Steam injection and recovery in the APPU

Parametric analysis on the impact of steam injection and recovery on the Auxiliary Power and Propulsion Unit embedded turboshaft engine

Martin van Schie

Delft University of Technology

TU Delft

Steam injection and recovery in the APPU

Parametric analysis on the impact of steam injection and recovery on the Auxiliary Power and Propulsion Unit embedded turboshaft engine

Thesis report

by

Martin van Schie

to obtain the degree of Master of Science
at the Delft University of Technology
to be defended publicly on July second, 2024 at 09:30

Student number:	4648366	
Institution:	Delft University of Technology	
Project Duration:	October, 2023 - July, 2024	
Supervisors:	Prof. Dr. Arvind Gangoli Rao	
	Dr. Ing. Alexander Heidebrecht	
Thesis committee:	Dr. Ir. Feijia Yin	TU Delft, Chair
	Prof. Dr. Arvind Gangoli Rao	TU Delft, Supervisor
	Dr. Ing. Alexander Heidebrecht	TU Delft, Examiner

TU Delft

Preface

This thesis marks the conclusion of my time as a student here in Delft. Despite tribulations such as the coronavirus pandemic, I look back at this period with a lot of joy and many good memories. Luckily, by the time I started my thesis, there were no restrictions and I could work on-campus, enjoying the essential coffee breaks with my peers. I learned so much during my thesis, academically, technically, and personally. Although *pyCycle* was challenging to get acquainted with, by the time is was writing my report I yearned back to the coding-days. Working on this thesis was a rollercoaster with lots of celebrations and frustration.

I want to thank my supervisors, Arvind Gangoli Rao and Alexander Heidebrecht, for their input, guidance and support. You were always very direct and honest in your feedback, which I greatly appreciate. This resulted in my goals being very clear, allowing me to work independently without requiring frequent steering. I want to note my appreciation for the propulsion modelling group meetings as well. These allowed for easy update opportunities, with great critical assessment of my intermediate results. For this I want to thank Feijia Yin and Turhan Eker as well, as you did not shy away from asking difficult questions, making me reassess any oversights.

I also want to thank my friends and family. My parents have always stood by my side, with never-ending love and support, enabling me to pursue my goals freely. I want to thank my friend Simon, who I could always talk to even when times were busy. I appreciate our always-fruitful pre-exam sparring sessions, which I am sure improved my grades during my bachelor. I want to thank my friends from the Hydromotion Team, who were always a nice distraction from the thesis stress — especially Peer, who I could always vent successes, difficulties, and frustration to during our breaks and lunches in Echo. Last but not least, I want to thank my girlfriend Helena. You were always there to support me, knowing when I needed to vent or be distracted, and always keeping my spirits up with your positive outlook.

I want to conclude by saying that overall I enjoyed this research project and the topic of preliminary engine design. I hope my efforts could prove valuable, both in the *A321 APPU* project and in the general academic and aerospace community. I hope you find the report interesting, and maybe learn something new.

Martin van Schie
Delft, June 2024

Executive summary

At the current trend of increasing demand, despite decreasing energy requirements, the climate impact of aviation will grow, counteracting the fact that the Advisory Council for Aeronautics Research and Innovation in Europe (ACARE) has set significant emissions reduction targets for 2050. To this end, radical aircraft and engine concepts are required. However, a faraway EIS introduces the need for semi-radical concepts that could enter service sooner. The *A321 APPU* is an example that can reduce aircraft-level emissions, while the Steam Injection and Recovery (SIR) cycle can offer improvements on the engine level. The goal of this research is to give a performance estimate of a baseline engine and an assessment of what improvements the SIR cycle can offer.

The *A321 APPU* is a modification of the A321neo. The tail section is modified in order to fit a liquid hydrogen tank and the Auxiliary Power and Propulsion Unit (APPU) dual-fuel turboshaft engine. The APPU powers a Boundary Layer Ingestion propulsor, taking over 10% of the cruise total thrust requirement and thereby reducing mission CO_2 emissions by 11%. The APPU is a two-spool free power turbine hydrogen-kerosene turboshaft engine with an axial and centrifugal compression system. The SIR cycle would add Heat Exchangers (HE) that liquefy and capture water from the exhaust using the LH_2 fuel as the heat sink. The captured water is pressurised and evaporated before it is injected into the combustion chamber. The exhaust flow is split in order to effectively utilise the cooling potential of the LH_2, directing a small portion of the flow towards the HEs. The expected effect of the SIR cycle is an increase in efficiency and a significant reduction in NO_x emissions.

The engines are modelled in *pyCycle*, an open-source parametric engine analysis tool based on *NASA*'s *openMDAO* framework utilising *NASA*'s *Chemical Equilibrium with Applications* (*CEA*) model for the determination of thermodynamical properties. A commercial equivalent, *Gasturb*, is used for verification purposes and the engine core mass estimation. Methods are developed for the determination of component efficiencies based on cycle parameters, such as efficiency and specific weight. Additionally, *pyCycle*'s capabilities are expanded so that the SIR cycle can be modelled. HEs are added, as well as the IAPWS-97IF water properties model, and the principle of relative humidity governs the condensation process. The added methods and components are verified to work as intended, and *pyCycle* and *Gasturb* are in excellent agreement.

The APPU is tested in cruise, at take-off, and while performing APU duties, for both hydrogen and kerosene operation. Thermal efficiencies up to 45.0% are observed, a notable improvement over turboprop engines currently in service. An engine mass of 502 kg is estimated, giving a specific power of 10.5 kW/kg. The SIR cycle is found to improve cruise fuel consumption with 1.54% while reducing the NO_x emissions by 33.4% but at the cost of a 15.7% engine mass increase. The engine is found sensitive to the turbine Allowable Material Operating Temperature, as well as the intake pressure recovery. The fraction of the flow directed through the HEs is found to have an optimum regarding fuel consumption and NO_x emissions reduction, which is used in all other analyses. A large power output discrepancy is observed between hydrogen and kerosene operation, which is attributed to the differences in the combustion products' specific heat capacity. The current form of *pyCycle* does not incorporate any impact from the fuel temperature, while the comparisons between different fuels and cycles could be significantly impacted if this is to be included. The hydrogen cruise efficiency improvement of the SIR APPU would increase to 7.3%. Additional sources of inaccuracies are identified and found to be negligibly small. Recommendations for future work include studies to improve the accuracy of analyses, and more detailed design and analysis efforts focused on individual components, especially the heat exchangers and the combustion chamber.

Contents

Nomenclature

List of Abbreviations

ACARE	Advisory Council for Aeronautics Research and Innovation in Europe
AMOT	Allowable Material Operating Temperature
APPU	Auxiliary Power and Propulsion Unit
APU	Auxiliary Power Unit
BLI	Boundary Layer Ingestion
CEA	Chemical Equilibrium with Applications
CFD	Computational Fluid Dynamics
EIS	Entry Into Service
FAR	Fuel-to-Air Ratio
HE	Heat Exchanger
HPC	High-Pressure Compressor
HPT	High-Pressure Turbine
HRSG	Heat Recovery Steam Generator
IAPWS	International Association for the Properties of Water and Steam
ICAO	International Civil Aviation Organization
LH_2	Liquid Hydrogen
LHV	Lower Heating Value
LPC	Low-Pressure Compressor
LPT	Low-Pressure Turbine
LTO	Landing and Take-Off
MDAO	Multi-Disciplinary Analysis and Optimization
NOx	Nitrogen Oxides
NPSS	Numerical Propulsion System Simulation
OPR	Operating Pressure Ratio
PR	Pressure Ratio
PT	Power Turbine
RPM	Revolutions Per Minute
RQL	Rich-burn Quick-quench Lean-burn
SFC	Specific Fuel Consumption
SIR	Steam Injection and Recovery
SIRA	Steam Injection and Recovery Aeroengine
SP	Specific Power
SR	Splitting Ratio
TET	Turbine Entry Temperature
TL	Technology Level
ToC	Top-of-Climb
V & V	Verification and Validation
WAR	Water-to-Air Ratio
WET	Water-Enhanced Turbofan

List of Greek Symbols

ϵ	Heat exchanger effectiveness
$\eta_{thermal}$	Thermal efficiency
γ	Specific heat capacity ratio
ϕ	Relative humidity

List of Roman Symbols

A	Area
C_p	Constant pressure specific heat capacity
C_v	Constant volume specific heat capacity
dP	Pressure loss
h	Specific enthalpy
M	Mach number
m	Mass
N_{mech}	Shaft speed

P	Power	T	Temperature
P	Pressure	T_b	Allowable Material Operating Temperature
Q	Heat flux	W	Massflow rate
Q	Water flow rate	x_{H_2O}	Water molecular fraction

List of Figures

List of Tables

1 Introduction

The demand for aviation is growing, making it challenging to reduce its emissions. The aviation sector currently (2019) contributes about 4% to anthropogenic global warming [1]. On average, the number of passenger kilometres increases by approximately 4.8% per year. However, aircraft are also becoming more fuel-efficient. Since the 1960's the fuel consumption per passenger kilometre has decreased by 75%, and about half of this reduction is a result of improved gas turbine efficiency [2]. The fuel burn per passenger kilometre is expected to further reduce by approximately 1.3% every year [3]. The result is that, despite the efficiency improvements, the climate impact will still continue to grow. This puts stress on parties involved in aircraft design and operations, as the Advisory Council for Aeronautics Research and Innovation in Europe (ACARE) has set targets to reduce CO_2 emissions by 75%, NO_x emissions by 90% and perceived noise by 65% by 2050, compared to the 2000 technology level [4]. Part of this will come from improved aircraft technology and operations efficiency, and part will come from using renewable fuels, such as sustainable aviation fuel and hydrogen [1, 5–8].

To these means, radically different aircraft designs are proposed, such as blended-wing-body aircraft [9] and the Flying-V [10], which are mainly aimed at reducing the aircraft's energy requirement. Also, aircraft completely fueled by hydrogen [11] or electric aircraft are conceptualised, which target to reduce CO_2 emissions by utilising a different energy carrier. What these aircraft concepts have in common is that their Entry Into Service (EIS) is expected to be around 2040-2050[1] [12, 13].

While these aircraft could offer major emissions reductions, their EIS is many years away, leaving the period until then with no more than minor fuel burn improvements as the tube-and-wing aircraft is further refined. This is where semi-radical aircraft concepts come in. An example of a semi-radical concept is a tube-and-wing aircraft with hybrid propulsion. Hybrid propulsion could be turbo-electric or by means of using multiple fuels. These types of aircraft could have their EIS around 2030-2040 [12, 13].

An example of such a hybrid aircraft is the *A321 APPU*, which has kerosene-fueled main engines and a dual-fuel kerosene or hydrogen Auxiliary Power and Propulsion Unit (APPU) [14]. The *A321 APPU* project is a venture aiming to decrease CO_2 and other harmful emissions by means of replacing the Auxiliary Power Unit (APU) with an Auxiliary Power and Propulsion Unit in an Airbus A321 [14]. The aim of the project is to reduce CO_2 emissions by 20% while keeping the changes manageable [15]. Limiting the number of changes and innovations reduces development time and risks. The APPU is an addition to the sufficiently powerful main engines, reducing risk and requirements regarding reliability and certification [14, 16]. Next to reducing overall mission CO_2 emissions, the introduction of an APPU should reduce the Landing and Take-Off (LTO) cycle emissions by 50% [15].

Besides improvements in aircraft technology, advances in engine performance are required as well to reduce the energy requirement further. Improvements in areas such as fluid dynamics and material science have brought this increased performance thus far, but this trend is stagnating and is subject to theoretical performance limits [2]. For this reason, revolutionary engine designs are required. One such technology is that of Steam Injection and Recovery (SIR). This technology adds a semi-closed water cycle to the conventional Brayton cycle, potentially allowing for improved fuel economy and reduced NO_x

[1] *Will the Flying-V get off the ground?*, news article by T. van Dijk, https://www.tudelft.nl/en/delft-outlook/articles/will-the-flying-v-get-off-the-ground, accessed 21-9-2023

emissions. The effects of adding SIR have been studied for a turbofan engine by Schmitz et al. [17] and Kaiser et al. [18], showing significant performance improvements. However, the SIR cycle for a turboshaft engine has not yet been studied.

This research aims to fill that knowledge gap, as well as provide an updated and more elaborate performance assessment of the APPU. A previous internal design study provided an indication of the APPU performance but did not include an analysis regarding the dual-fuel capability. Additionally, power requirements have been updated [2], as well as the inlet duct pressure loss [19, 20]. Therefore, a next iteration and more extensive design study of the baseline APPU is warranted. These two research objectives suggest the following research question:

What are the effects on engine SFC, NO_x emissions and engine mass of incorporating a steam injection and recovery cycle in the APPU engine?

To simplify the project, this research question is split up into the following sub-questions:

1. What is the performance of the baseline APPU, both in on- and off-design conditions?
2. How can an existing engine analysis tool be expanded such that the steam injection and recovery cycle can be modelled?
3. What is the engine performance of the steam injection and recovery APPU engine, both in on- and off-design conditions?
4. What is the sensitivity of the results to variation in input parameters such as Operating Pressure Ratio (OPR), Turbine Entry Temperature (TET), Splitting Ratio (SR), heat exchanger effectiveness (ϵ), etc.?

The remainder of this report gives the context and methods for answering the above research question. It first elaborates on the context of the engine and its current design. Next, it explains the methodologies that are used to model the baseline APPU and form the basis of the SIR cycle analysis. After that, it discusses the fundamentals and motivation of the SIR cycle, introduces the proposed SIR APPU engine architecture, and explains the methods added to the analysis to be able to model the SIR cycle. Then, the results are discussed and critically analysed. Lastly, conclusions are drawn, including recommendations for future work.

Chapter 2 dives deeper into the *A321 APPU* project, giving the context to understand the current state of the project and the APPU itself. Next, the methodologies used for the analysis of the baseline APPU are explained in Chapter 3. Then, the SIR cycle is further explained, as well as the methods implemented in order to analyse the SIR cycle in the APPU. Thereafter, Chapter 5 aims to verify and validate both the baseline and SIR cycle, providing confidence in the results. Chapter 6 presents these results, which are then critically analysed in Chapter 7. Lastly, conclusions are drawn in Chapter 8 and Chapter 9 concludes this report with recommendations for future research.

[2] Personal correspondence with Dr. Ing. Alexander Heidebrecht on 28-11-2023

2

The *A321 APPU* project

This chapter will dive deeper into the APPU project that is mentioned in Chapter 1. The engine will be designed with a very specific use case in mind, with tailored power requirements and various input parameters dependent on the aircraft integration. Why the project exists is reiterated and the current state of the project is elaborated upon, emphasising the changes to the A321neo. Since this research revolves around the APPU itself, the engine is explained to a deeper level, as well as what choices were made to lead to this design, and why. Section 2.1 explains the *A321 APPU* project and aircraft, after which Section 2.2 gives a detailed discussion of the APPU engine itself.

2.1. The *A321 APPU* project and aircraft

Chapter 1 introduces the APPU project as a semi-radical aircraft design. It is supposed to be a step in between the existing aircraft (tube-and-wing aircraft that use kerosene) and the radically different aircraft concepts (such as blended-wing-body aircraft), with the main goal of bringing the EIS forward while still offering significant emissions reductions. In the *A321 APPU*, the APU, which is located in the tail cone, is replaced with the APPU, a dual-fuel hydrogen-kerosene turboshaft engine driving a rear-mounted BLI propulsor. The dual fuel capability increases the operational flexibility, lowering the threshold towards hydrogen-powered aircraft propulsion. The latest design study by Heidebrecht et al. [14] suggests a 10% share of the total cruise thrust for the APPU. This leads to a 10.9% kerosene usage decrease when flying 4630 km with 25 tons of payload. This analysis only considered the cruise phase. The *A321 APPU* can significantly cut back on the LTO cycle emissions as well. An earlier design study by students of the Delft University of Technology [16] suggested that the LTO non-CO_2 emissions of an *A320 APPU* could be reduced by 64.5%, as well as a 58.6% reduction in kerosene usage. Most of these reductions come from the fact that the APPU provides the thrust required for taxiing, massively reducing the main engine idle time [16, 21, 22].

The study by Heidebrecht et al. [14] suggests a limited number of changes, most of which can all be seen in Figure 2.1. The APPU is located right at the tip of the slightly modified tail cone, with the Boundary Layer Ingesting (BLI) propulsor directly attached. BLI aims to improve the propulsive efficiency by energising the low-energy boundary layer, instead of the already-high-energy free-stream air. For more information on the BLI propulsor principle and quantification of its potential benefits, the reader is referred to works such as Smith [23], Uranga et al. [24] and Moirou [25]. Placing the APPU here facilitates the BLI concept, as well as allowing all tailplanes to be in front of all large rotating elements. The conical LH_2 tank is placed right in front of the APPU. This shape was chosen to maximise fuel volume. The tank placement requires the horizontal stabiliser to be moved up onto the vertical stabiliser. Not shown in Figure 2.1 is the inlet duct for the APPU. There is not yet a definitive design for the inlet duct, but a recent study by Bariş [20] explored different submerged inlets applied to the *A321 APPU* context. However, a long duct with its inlet at the base of the vertical stabiliser leading edge is a possibility as well. Because the former provides an accurate pressure loss value, a submerged-style inlet is assumed for now. Lastly, the wing is moved aft by 1.2 m in order to balance the aircraft with the shifted centre of gravity.

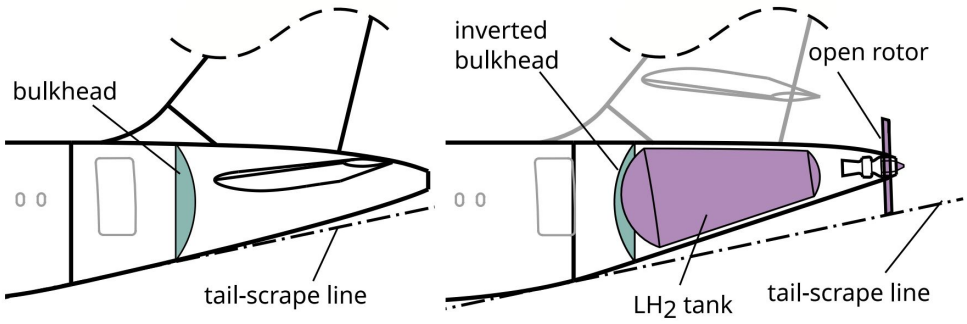

Figure 2.1: Comparison of the tail cone of the A321 and the modified *A321 APPU*

2.2. The engine

Next to these analyses at the aircraft level, studies have been done on the APPU design itself. The latest, an internal design study from 2021, is used as a starting point for this research and provides most of the architectural decisions. Figure 2.2 gives a schematic representation of the proposed architecture resulting from this study. The engine is a two-spool free power turbine turboshaft engine. This research does not include the BLI propulsor, hence it is discarded in this walk-through as well. It has a 4-stage axial LPC and a single-stage radial HPC. The turbines are all axial, consisting of a one-stage HPT, one-stage LPT and 3-stage PT. The combustor is of the reverse-flow configuration. This section will assess and explain if and why this architecture is suitable for the APPU. First, the spool architecture, two-spool with a free turbine, is discussed in Section 2.2.1, after which Section 2.2.2 elaborates on the choice of compressor types. Lastly, the choice for a reverse flow combustor is explained in Section 2.2.3.

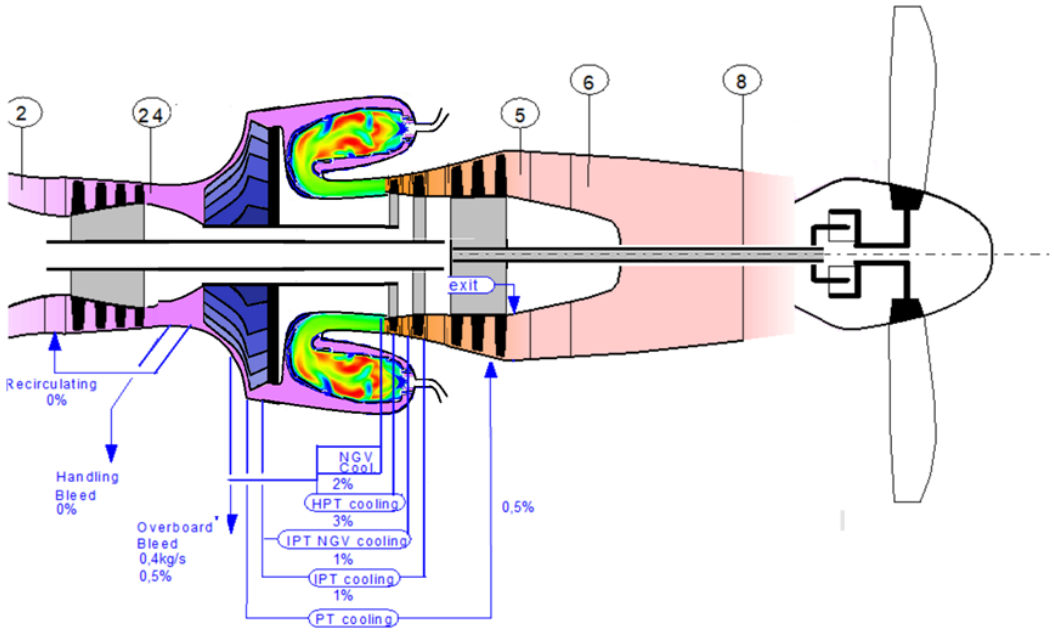

Figure 2.2: Schematic representation of a previous preliminary design for the APPU engine [19]

2.2.1. Spool architectures

A major and important part of the core of turbine-based engines consists of rotating compressor and turbine stages. The turbines extract energy from the flow, and (part of) this energy is used to power the compressor stages. The most convenient way of transferring this power is by mechanically connecting the compressor and turbine using a shaft or multiple concentric shafts. However, a designer still has large design freedom

even when constrained to using shafts. In this section, the configurations currently used in existing engines are mentioned and explained (in order of increasing complexity), and if applicable, applications are mentioned. An introduction to all different possibilities paves the way to a better understanding of the design choice.

Single-spool

The simplest engine architecture is that of the single-spool engine. All turbomachinery, both for gas generation and power generation, is connected using one shaft, as shown in Figure 2.3 [26]. A single shaft is currently mostly used in gas turbines for power generation. The constant speed and little load variations make a single-spool well-suited for that application [27]. An example of an aero-engine application of a single-spool architecture is the Rolls Royce Dart turboshaft engine, which entered service in 1953 [28].

A disadvantage of a single-spool engine is the coupling between the gas generator and the load. If the load requires a slower rotating speed (in the case of a fixed-pitch propeller for example), the operation of the gas generator is altered. The slower speed reduces the pressure ratio, and as a result, the output torque (and thus also power) decreases, as is shown in Figure 2.4 [27].

The single-spool architecture is advantageous due to its simplicity and low weight, as there is only one shaft that requires bearings and adds to the mass[29, 30]. The architecture is disadvantageous however due to its coupling between the load and the gas generator, decreasing off-design performance.

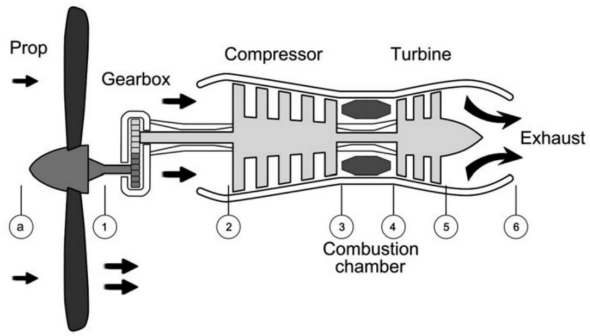

Figure 2.3: Schematic view of a single-spool engine [26]

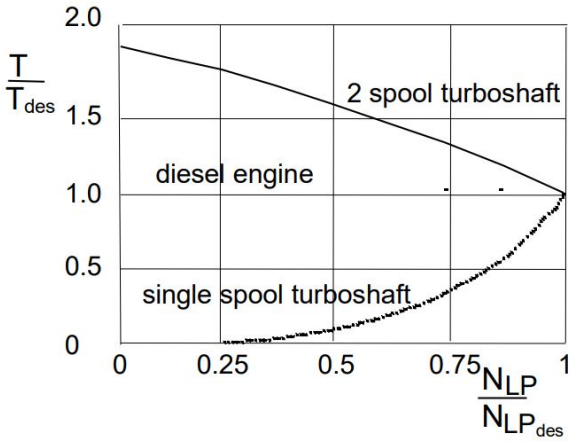

Figure 2.4: Influence of spool speed (N_{LP}) on engine torque (T) for a single-spool engine [27]

Single-spool with free power turbine

In an engine with a single spool and a free power turbine, the gas generator and the power extraction are decoupled. A schematic view of this architecture is shown in Figure 2.5 [26]. The first turbine stages

power the compressor, and the last turbine stages drive the load. An engine with a free turbine is suited for applications where there are (rapid) load variations and good part-load requirements are desired. Also, applications where the output shaft speed varies, such as a fixed-pitch propeller, fare better with a free power turbine. This is because the gas generator speed (and thus its power) is independent of the power turbine speed [27]. However, the addition of a spool does increase complexity, making this architecture unsuitable for micro-turbines.

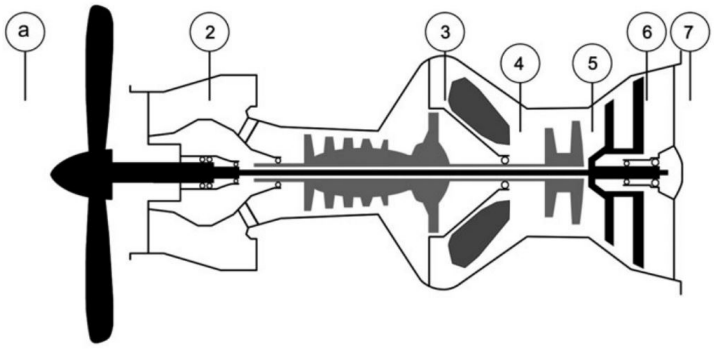

Figure 2.5: Schematic view of a single-spool engine with a free power turbine [26]

Twin-spool

The twin-spool architecture splits the gas generation into a low- and high-pressure segment. The low-pressure turbine also drives the load. The two shafts are concentric, meaning that the low-pressure spool shaft runs through the high-pressure spool shaft. A schematic of this architecture is shown in Figure 2.6 [28]. Having two spools adds mechanical complexity (and all its disadvantages) over a single-spool. The drawbacks of this added complexity can be negated by a gain in efficiency. Having two spools means one can let different compressor and turbine stages operate at different rotational speeds, allowing higher efficiencies and pressure ratios as the components can operate closer to their optimum speed. This improved efficiency, in turn, allows higher stage loading, which leads to fewer stages, saving weight, lowering costs and shrinking the engine envelope [26], or one can opt to go for a higher OPR, increasing the engine's thermal efficiency [28]. Also to prevent unmanageable off-design stability issues at higher OPRs a second shaft is warranted [31].

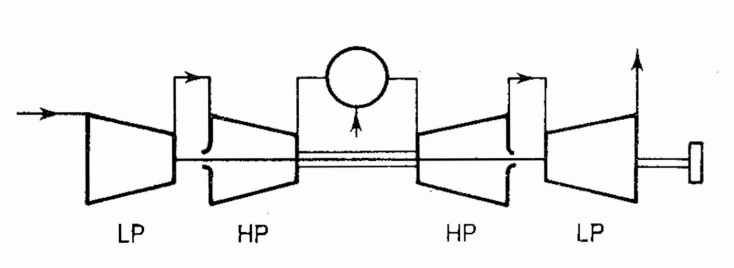

Figure 2.6: Schematic view of a twin-spool engine [28]

Twin-spool with free power turbine

The twin-spool with free power turbine architecture combines the benefits of a twin-spool engine with those of a free power turbine. Having a third spool adds even more complexity compared to the two-spool arrangement, but how much depends on the engine/propulsor integration. Suppose the load is located on the intake side of the engine. In that case, the shaft from the power turbine has to run through the engine, essentially making the engine mechanically as complicated as a triple-spool engine. If the load is at the exhaust side of the engine, the engine becomes essentially a twin-spool turbojet with an added power turbine at the rear [31]. Figure 2.7 schematically shows the latter architecture [28].

A real-world example of this spool architecture is the PW100-150 engine series. This engine has its

load on the intake side and thus has three concentric shafts. This engine series has a maximum mass flow rate in the range of 6.7-14.4 kg/s and an OPR between 12 and 18, depending on the engine type [32].

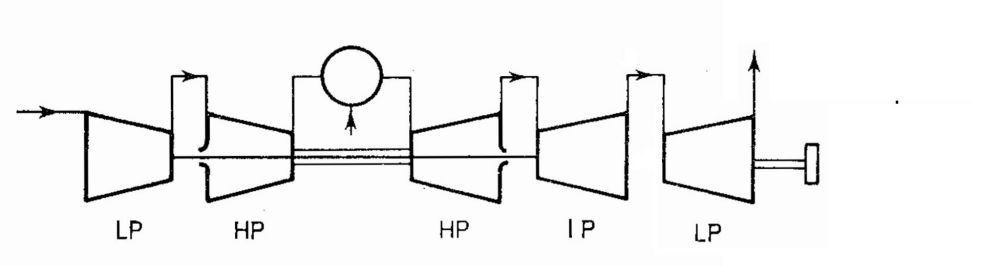

Figure 2.7: Schematic view of a twin-spool engine with a free power turbine. Modified from [28]

APPU engine spool architecture
The APPU has the propeller it powers on its aft, as mentioned in Section 2.1. Hence it makes sense to have a free power turbine, as it does not add a concentric shaft to the forward parts of the engine, limiting the increase in mechanical complexity. The PW100-150 engine series is regarding inlet mass flow of comparable size and has multiple shafts. By the reasoning of comparison, the APPU should have multiple shafts as well. The resulting APPU spool architecture thus should be a two-spool free power turbine configuration.

2.2.2. Compressor architecture

With the spool architecture known, it needs to be determined what types of compressor to put on each shaft. The function of the compressor is to increase the pressure and temperature of the intake air so that (sustained) combustion can take place in the combustion chamber. A compressor can take two forms: an axial compressor and a centrifugal compressor. Examples of an axial- and centrifugal compressor are shown in Figure 2.8 and Figure 2.9 respectively [33]. This dive into the characteristics of compressors will be limited to aspects important for making a design choice for the APPU. For a better understanding of the fundamentals and basic working principle is the reader referred to textbooks such as Saravanamuttoo [28] and El-Sayed [26]. This section will discuss what possible compressor architectures are and include indications of when and why to use which architecture.

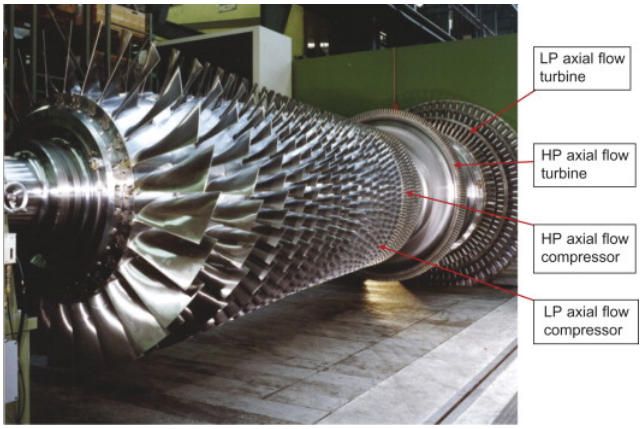

Figure 2.8: Axial compressor [33]

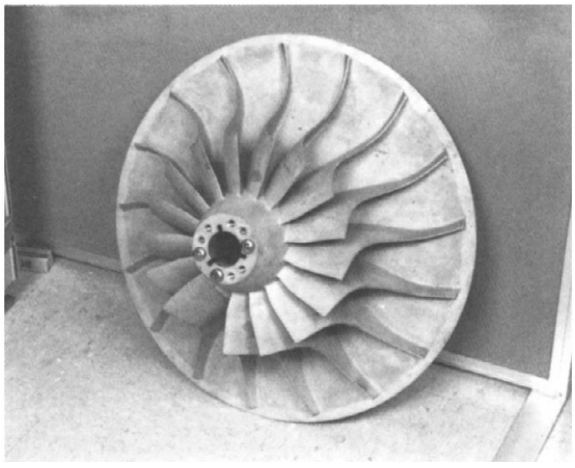

Figure 2.9: Centrifugal compressor [33]

Logically, it is desired to use the type of compressor that has the best efficiency for the application. Theoretically, axial flow compressors are capable of higher efficiencies than radial compressors. However, as a compressor becomes smaller, real-world effects such as Reynolds number effects, relatively larger tip gaps and production inaccuracies lower the attainable efficiency. Axial flow compressors are more

heavily influenced by these size effects, as is shown graphically in Figure 2.10 [31, 34]. Note the steep efficiency drop for an axial compressor at low exit flow function values, and how the centrifugal compressor surpasses the axial compressor at very low values. The corrected mass flow (W_c), which is similar to the compressor exit flow function, is a strong indicator of the rough size of a compressor.

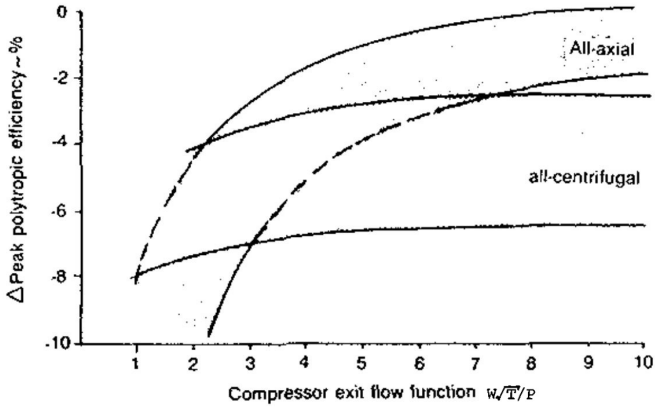

Figure 2.10: Effect of the compressor size on the efficiency [31]

There are several other aspects to consider when deciding on a compressor architecture, such as mass and frontal area. However, the main driving aspect for the compressor type choice in this research is the achievable efficiency. Yet, detailed geometrical design is outside the scope of this research. Therefore the efficiency is considered dependent on the exit-corrected mass flow. More details on the method used to correlate these two parameters are given in Section 3.2. W_c is easily quantifiable and takes important cycle parameters into account, such as OPR and inlet mass flow. For the baseline APPU W_c <1.7 lbm/s is observed, using the inputs specified in Table 6.2. However, the corrected mass flow value at which the transition between axial and centrifugal lies is trickier to determine. Sadler & Hodges [31] set this transition zone to be between 2.5 and 3.5 lbm/s corrected mass flow (see Figure 2.10), but this is a dated assessment. A more recent study on turboshaft engines by Welch et al. [35] used W_c ≈1.5 lbm/s as the transition point. This value was derived by taking practical limits into account, such as the minimal achievable tip gap. The APPU HPC exit W_c is close to this value, prohibiting a clear choice based on corrected mass flow.

Because the corrected mass flow could thus not be the definitive deciding factor, the now driving characteristic for the compressor type selection is the compressor off-design operation. Because the engine needs to be able to operate in more than one condition, so do the compressors. The compressors need to be able to handle different incoming corrected mass flows, as well as spinning at different speeds. The off-design performance of a compressor is captured by a compressor map. A compressor map tells one what the efficiency and pressure ratio are given the speed and corrected mass flow, while also indicating operational limits, such as the surge line. Indicative maps for both an axial and centrifugal compressor are shown in Figure 2.11. Note that for a given spool speed, a centrifugal compressor can handle a larger range of corrected mass flow. This hints at an advantage centrifugal compressors have over their axial-flow counterpart: they have a wider operational range. This might be beneficial or even required for the APPU because it does not only need to be able to handle different flight conditions but also different fuels. Therefore, the centrifugal compressor type is selected for the APPU HPC.

2.2.3. Combustor architecture

The combustor is an essential part of the engine. In the combustion chamber, fuel is added and combusted, raising the flow temperature. The combustion chamber needs to meet many requirements, such as high combustion efficiency, low pressure loss, low emissions and wide stability limits [36]. Most aspects regarding any detailed geometry are outside the scope of this research, meaning the combustor is just a black box where the fuel gets added, but the mass estimation requires the input of either a *straight-through* or a *reverse-flow* type combustor.

A straight-through combustor means that the flow is always predominantly in the axial direction, from front to back. This is the most commonly used combustor type in aero-engine applications. This is because

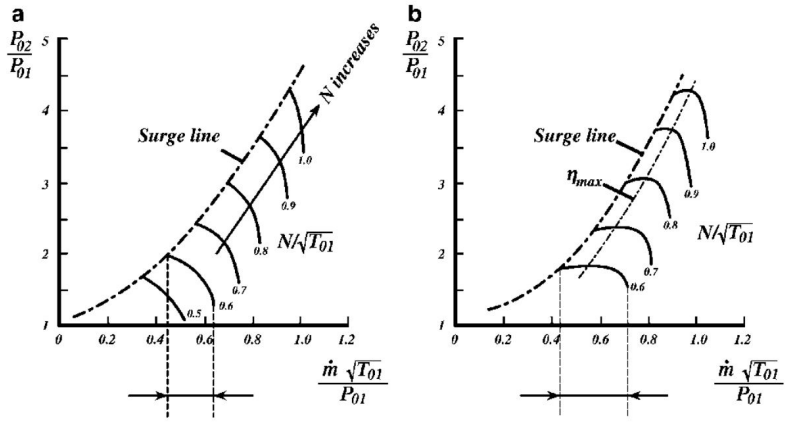

Figure 2.11: Indicative compressor maps for axial compressors (a) and centrifugal compressors (b) [26]

it is well-suited for all-axial turbomachinery engines, as well as generally having lower pressure loss than reverse-flow combustors [36].

In a reverse-flow combustor, the combustion flows in the opposite direction, as can be seen in Figure 2.12 [36]. Note how the flow has a long flow path alongside the liner, contributing to large pressure losses [27]. Also, note how the combustor exit is located radially inward compared to the inlet. This is convenient when combining a radial compressor with an axial turbine, the turbomachinery architecture of the APPU. Additionally, this type of combustor allows the turbines to be closer to the compressors, shortening the engine [36]. This benefits the *A321 APPU* aircraft, as a shorter engine leaves more room for the hydrogen tank or a less aggressive inlet curve. These benefits result in the reverse-flow combustor being the chosen combustor type for the APPU.

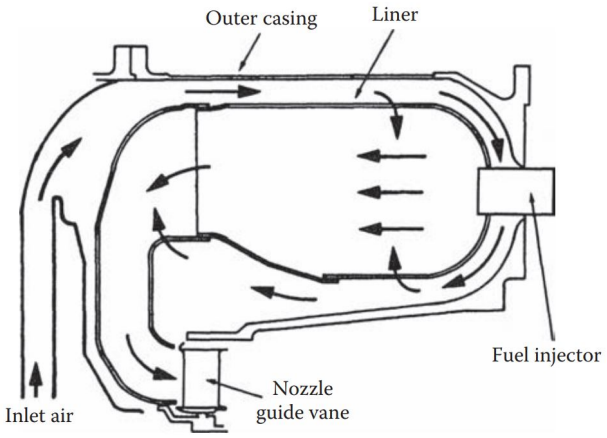

Figure 2.12: Indicative schematic of a reverse-flow combustor

3

Baseline methodologies

The first objective of this research is to establish the performance of the baseline APPU. With the engine architecture determined in Section 2.2, a numerical model can be constructed. This chapter will discuss the methods used, both for analysing the engine cycle and for determining cycle inputs based on this specific application. Understanding these methods is essential in order to be able to understand the results and assess their validity and shortcomings. The methodologies specific to the SIR cycle are discussed in Chapter 4. Firstly, the computational tools used are introduced in Section 3.1, after which the methods for determining component efficiencies are listed in Section 3.2.

3.1. Analysis tools

Turboshaft engines are complex machines. Components, such as compressors and turbines, have dependencies on each other, and there are many input variables for a designer to play with. Additionally, the physics governing the components and engine operation are complex. The performance of the APPU will be calculated by means of parametric analyses. In this type of analysis, the engine consists of black-box components tied together. Inside these components are the physics governing the components' impact on the flow. To aid the designer in making an engine, numerous engine modelling software tools have been developed. This research utilises two of these tools: *pyCycle* and *Gasturb*. Their characteristics, advantages and drawbacks are described in Section 3.1.1 and Section 3.1.2, respectively. Section 3.1.3 summarises what each tool is used for.

3.1.1. *pyCycle*

This section introduces the primary analysis tool used in this research: *pyCycle*. First, its origin is mentioned, followed by the advantages and drawbacks of the software while introducing some of the underlying physics used.

pyCycle was born from the need to be able to incorporate engine design into the complete aircraft design [37]. Modern aircraft design requires increasing amounts of multi-disciplinary interaction [37, 38], such as the aeropropulsive interaction of the BLI concept mentioned in Chapter 2. The developers recognized that, despite some moderately successful efforts [39–41], *NASA*'s *Numerical Propulsion System Simulation* (*NPSS*) [42, 43] software was found to be insufficient in its ability to be incorporated in Multi-Disciplinary Analysis and Optimization (MDAO) [37]. MDAO is about solving design problems that can be defined by coupled (complex) numerical models [38]. When using MDAO, one can (quickly) explore a design space consisting of a large number of variables where different engineering disciplines influence each other. *NASA*'s *openMDAO* framework [38, 44] was used as the basis for *pyCycle*. This underlying optimization structure allows *pyCycle* to be more easily and effectively integrated into larger multi-disciplinary problems, such as coupled airframe and propulsion systems design [37].

Hendricks & Gray [37] tested *pyCycle* against *NPSS* for its accuracy and computational cost. *NPSS* is considered the most advanced engine cycle analysis tool, and can thus be used as a benchmark. An advanced turbofan engine was simulated both in *pyCycle* and *NPSS*, and it was concluded that *pyCycle* deviated less than 0.03% from the *NPSS* results. Due to its more efficient method for calculating derivatives, *pyCycle* was between 7 and 23 times faster than *NPSS*, depending on the derivative calculation method used in *NPSS*.

pyCycle does not have an included graphical user interface. This could be a drawback if one wants to quickly model a standard engine. However, this is a significant advantage when one wants to integrate *pyCycle* into a more extensive analysis, as is its intended use. Additionally, because *pyCycle* is open-source and in easily accessible Python scripts, it allows for great flexibility. This comes in very useful when one wants to analyse the steam injection and recovery cycle. *pyCycle* does not yet contain the capability to model heat exchangers and model water extraction, and it is not yet capable of dealing with the phase change of water and hydrogen. The modifyability allows these modules and capabilities to be made and implemented. Next to that, the modifyability shows itself in the very flexible 'engine builder'. Whereas other software might have a library of available architectures but cannot deviate from those, in *pyCycle* one can build up the engine in any way that is desired. This is because *pyCycle* consists of modules of engine components that can be tied together to form an engine.

pyCycle uses two methods for determining thermodynamic properties: tabular data with interpolation, and its own adaptation of the *NASA Chemical Equilibrium with Applications* (*CEA*) method [45–47]. Only the latter will be used in this research. While the *NASA CEA* method is capable of calculating the properties for both liquid and gaseous water [45, 46], what is implemented into *pyCycle* is not; it can only model gaseous water. This prohibits the current version of *pyCycle* from analysing the SIR cycle. However, its modifyability allows this capability to be added. Details on this method are given in Section 4.3.1.

pyCycle is an engine cycle calculation tool designed with MDAO in mind. This makes *pyCycle* suitable for multi-disciplinary design problems where the engine is closely interconnected with and influenced by the other aircraft parts and systems. *pyCycle* is comparable in its accuracy with *NPSS*, which is considered the cutting edge of engine cycle analysis, and significantly reduces computational costs. *pyCycle*'s easily accessible Python code both allows it to be integrated into more extensive studies, and to be expanded such that novel engine cycles can be modelled.

3.1.2. *Gasturb*

Gasturb is an engine cycle analysis tool originally developed in the 1990s by J. Kurzke. Originally, it automated parametric- and performance cycle analysis and performed numerical optimisation to find the optimal cycle parameters for the chosen performance metric, while taking set constraints into account [48]. The version used in this research is *Gasturb* 12. This version can go into much more detail about the engine design, and is next to the original functions, for example, also capable of preliminary component design and engine mass estimation. For the other capabilities of *Gasturb* that are not used in this research, the reader is referred to the *Gasturb* 12 manual [49]. *Gasturb* can be considered a validated engine analysis tool. Wemming [50] compared results from *Gasturb* to experimental data from engine manufacturers. Discrepancies generally were less than +-2%, with some outliers up to +-10%.

The attractiveness of *Gasturb* is its wide range of capabilities and convenient user interface. This convenience in stand-alone use is the software inconvenience when the user desires to incorporate the software into a more extensive analysis effort [51]. The drawback of *Gasturb* is its lack of architectural flexibility. *Gasturb* comes with a number of pre-programmed engine architectures and configurations, which can only be modified to a minimal degree. The steam injection and recovery cycle is not among these options, meaning *Gasturb* can not be used for the second part of this research. The baseline cycle APPU architecture (a two-spool free power-turbine turboshaft) is available however, allowing *Gasturb* to be a benchmark to validate the *pyCycle* model against. This process is elaborated in Section 5.1.

Gasturb determines the thermodynamical properties in a similar but also different manner as compared to *pyCycle*. Similarly, the quantification of the gas properties, such as specific enthalpy, have their origin in the *NASA CEA* model. The difference lies in how this data is used. *Gasturb* has the required properties stored in tables. Pressure variation is not taken into account, meaning the thermodynamical properties of the flow in *Gasturb* are independent of pressure. Additionally, only the combustion products CO_2 and H_2O are considered. An exemption is made for the temperature rise due to combustion. Here the influence of various combustion products as well as the pressure are taken into consideration [49]. On the contrary, *pyCycle* calculates both the gas composition as well as the resulting gas properties at every station in the engine, taking the pressure into account. These differences in gas properties calculation could cause discrepancies when comparing results from the two analysis tools.

3.1.3. Analysis tool usage

The previous two sections describe the capabilities, advantages and drawbacks of *pyCycle* and *Gasturb* respectively. This section will list what each of the tools will be used for and why. It also explains what parameters are inputs in on- and off-design.

The primary analyses will be done using *pyCycle* and the enhanced version of it. As Section 3.1.1 states, *pyCycle* can be modified and expanded. This allows the SIR cycle to be modelled. By analysing both cycles in the same software, a better comparison can be made and the conclusions drawn are more valid.

Gasturb will be used to validate the baseline cycle APPU model in *pyCycle*. Additionally, *Gasturb* is used to do a mass estimation of the APPU. This way the APPU-specific cycle parameters and architecture can be taken into account, as opposed to using statistical data. The *Gasturb* mass analysis is also used for part of the mass estimation of the SIR APPU. The engine mass of the baseline cycle APPU will be adjusted linearly according to inlet mass flow. This value is similar in magnitude for both cycles, as is shown in Table 6.9, meaning the linear approximation should give reasonable results. The mass of the heat exchangers will be added to this engine mass. Details on the Heat Exchanger (HE) mass determination are provided in Section 4.4.2. This gives Equation 3.1 for the total engine mass of the SIR APPU.

$$m_{SIR,total} = \frac{W_{SIR}}{W_{baseline}} m_{baseline} + m_{HRSG} + m_{condenser} \tag{3.1}$$

When analysing an engine for a design condition, i.e. making an engine perfectly sized for the defined condition and cycle parameters, *pyCycle* uses the specified inputs to calculate the engine performance, and the flow path cross-sectional area, essentially giving the engine a physical size. If an off-design condition is to be analysed, the previously sized engine (in the on-design calculation) is given a different flight condition or throttle setting. It then calculates the off-design performance for that particular condition. This is only one distinction between on-design and off-design inputs. Table 3.1 lists the general required inputs for on- and off-design analyses, and what outputs are to be expected.

A different kind of analysis done in this research is a sensitivity analysis. In these analyses, an on-design analysis is done for a range of values of a specific input parameter. All other inputs thus remain constant, and a 'new specific' engine is designed for each instance of the varied parameter.

Table 3.1: Listing of required inputs and given outputs for *pyCycle* on- and off-design analyses

On-design inputs	On-design outputs	Off-design inputs	Off-design outputs
Flight conditions	SFC	Flight conditions	Power
Power requirement	W_{inlet}	Gas path area	SFC
TET	Gas path area	TET	OPR
OPR		Initial guesses	W_{inlet}
Efficiencies			Efficiencies
Map scaling			Flow speeds
Flow speeds			
Initial guesses			

3.2. Component efficiencies

An significant factor in the performance of a gas turbine engine is the efficiency of its components. Lower efficiencies or larger pressure losses can significantly deteriorate the engine performance. Because of the significant impact these input variables have, it is essential that appropriate values are used. However, in the used engine analysis tools, the components are essentially black boxes; no details about the geometry are known, making it impossible to calculate an exact component efficiency. To ensure the efficiencies are still tailored to the specific cycle of the APPU, they are determined with methods that use cycle-specific parameters. First, the efficiencies of the turbomachinery components, i.e. the compressors and turbines, are discussed in Section 3.2.1, together with cooling air requirements. Then, Section 3.2.2 finds an appropriate pressure loss value for the combustor.

3.2.1. Turbomachinery

The efficiency of turbomachinery depends on many parameters, such as approximate size and cooling air. Because both are not yet known (they depend on the cycle calculations), appropriate values cannot be set right away. Methods to determine these values based on the cycle calculations and their resulting impact on turbomachinery efficiency are discussed in this section. First, the bare efficiency is treated, after which the determination and effect of turbine cooling are discussed. Lastly, the turbomachinery component maps and how they are essential for off-design calculations are introduced.

Basic efficiency

As explained above, only minimal details are known about the turbomachinery. The set of characteristics required for the coming methods only contains values calculated by *pyCycle*, constants and user inputs. Using these parameters it is not possible to calculate an actual efficiency, as this requires additional geometrical inputs such as blade geometry and tip gap. However, with some assumptions, it is possible to get an approximate efficiency using only the corrected flow parameters. The main parameter that influences the component efficiency in this simplified method is the corrected mass flow, on the smallest side of the component. This means the compressor outlet and the turbine inlet. The corrected mass flow W_c is calculated using Equation 3.2:

$$W_c = W * \frac{\sqrt{\frac{T}{T_{ref}}}}{\frac{P}{P_{ref}}} \tag{3.2}$$

where T_{ref} is a reference temperature, which is 288.15 K (15 °C), and P_{ref} is a reference pressure, which is 1 atm or 101325 Pa.

How this corrected mass flow translates to a component efficiency is done using data from Snyder & Tong [52]. They made a trend for the compressor efficiency as a function of W_c, including both axial and centrifugal compressor types. Figure 3.1 [35] shows qualitatively how the efficiencies of the two compressor types are merged into a single trend: at low W_c the centrifugal compressor is driving the trend, while at high W_c the axial compressor takes over, with a blended region where efficiencies are close.

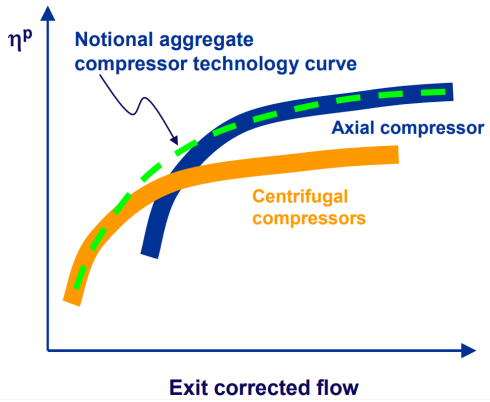

Figure 3.1: Notional compressor efficiency technology curves showing how a single trend represents both axial and centrifugal compressor types [35]

Using this method, they plot the component efficiency as a function of corrected mass flow for three Technology Levels (TL), see Figure 3.2. Turbomachinery technology constantly advances, and to account for this and any other uncertainty in the extent of advances and the EIS of the projected engine, these three TLs are used. Fitted curves were constructed for these lines to get a simple equation that gives the component efficiency as a function of the corrected mass flow. The general equation for these fitted curves is as follows:

$$\eta_{polytropic} = a * log^3(W_c) + b * log^2(W_c) + c * log(W_c) + d + e * W_c^{0.02} + f * ln(W_c) \tag{3.3}$$

where W_c is in lbm/s. The coefficients for the three TLs are determined using the Python Scipy optimise curve fit function and are stated in Table 3.2. This general equation is not optimized such that the error is minimized. Its purpose is to follow the original curve relatively closely, and have a derivative of the correct sign (always positive). The original data, together with the fitted curves, are shown in Figure 3.2.

Table 3.2: Coefficients for the efficiency fitted curves

Coefficient	Current	Advanced	Future
a	-9.3734E-1	-5.6394E-1	1.2959E-2
b	-6.0756E+1	-3.6526E+1	-3.3780E-1
c	3.2938E+1	3.0687E+4	3.2055E+2
d	-5.7260E+4	-3.4412E+4	-2.7590E+2
e	5.7261E+4	3.4413E+4	2.7681E+2
f	-1.1595E+3	-1.4016E+4	-1.4473E+2

The data from Snyder & Tong starts around 0.2 lbm/s and goes up to 10 lbm/s, meaning Equation 3.3 and the coefficients in Table 3.2 are valid between these values. A corrected mass flow below this range is not encountered in the analyses, and above this range the efficiency is set to that at 10 lbm/s. Note also the steep slope at small mass flows. This is partly because the data is a blend of axial and centrifugal compressors, as indicated in Figure 3.1.

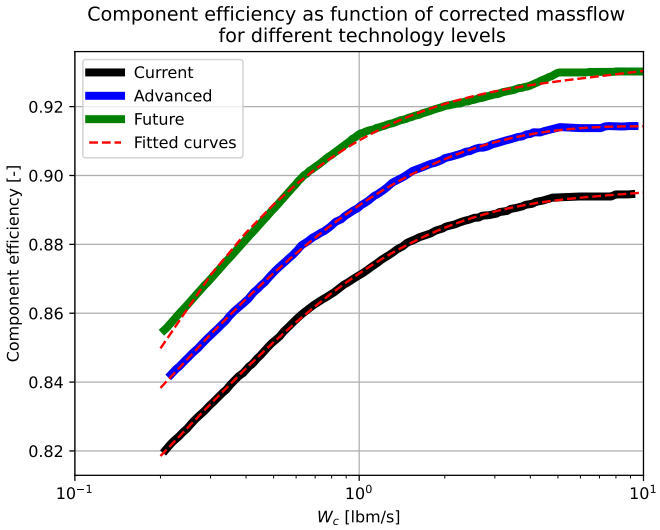

Figure 3.2: Component efficiency as a function of corrected mass flow for different technology levels with their respective fitted curves (data from [52])

Turbine cooling

Because of the increasing TET in modern aero-engines, the turbines require cooling to ensure they maintain their structural integrity, despite the increasing Allowable Material Operating Temperature (AMOT). This is shown in Figure 3.3 [3], where the trends in both AMOT and TET are shown, highlighting the discrepancy. However, cooling air lowers the efficiency of the turbine. It is therefore essential to assess how much cooling air impacts the efficiency and how much cooling air is required. The latter depends on the AMOT, so an investigation towards an appropriate value is conducted as well.

Cooling air impact: The method to be used in this analysis has been created by Yin & Gangoli Rao [3]. It was chosen for its compatibility with the data available in the *pyCycle* calculations. This method dictates that every 1% cooling air fraction lowers the turbine efficiency by 0.6%.

Cooling air requirement: Cooling air thus lowers the turbine efficiency. It is, therefore, desired to have the minimum amount of cooling air, just enough to cool the turbine sufficiently. Here a method is discussed that is used to determine the required amount of cooling air. The chosen method has been devised by Jonsson et al. [53]. This method is selected for its simplicity and, therefore, compatibility with data available from *pyCycle* calculations.

The cooling air mass fraction required to cool the turbine is calculated using Equation 3.4 [53]. The subscripts 'c' and 'g' indicate the parameters belonging to the coolant or the gas, respectively. C_P is the respective specific heat capacity, T_{in} is the turbine inflow temperature, and T_b is the AMOT. Lastly, b and s are adjustable parameters that represent the gas turbine configuration and technology level. b and s are 0.11 and 1.0 respectively [54]. T_b is specified as an input, and the other parameters are calculated by *pyCycle*.

$$\frac{W_c C_{P,c}}{W_g C_{P,g}} = b\left(\frac{T_{in} - T_b}{T_b - T_c}\right)^s \tag{3.4}$$

Turbine material temperature: As mentioned, the turbine AMOT is both a driving parameter in determining the cooling air requirement and is subject to technological advances. It is, therefore, essential to set an accurate value that is representative of the APPU application and EIS. The value encountered in research by Yin et al. [54] and by Yin & Gangoli Rao [3] is 1450 K. The EIS for their respective applications are 2035 and 2025, a significant difference. When analyzing the current and past state of technology, shown in Figure 3.3, the value of 1450 K seems feasible for 2030: 1050 K in 1950 and 1300 K in 2000, meaning a 5 K/year trend. This then gives 1450 K AMOT for an EIS of 2030.

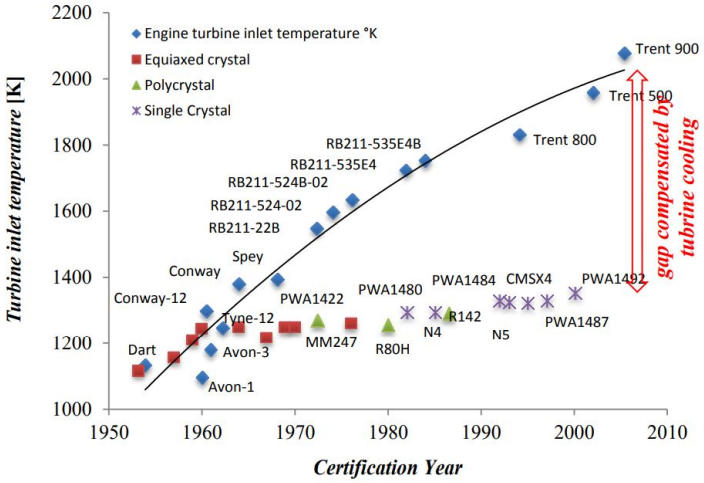

Figure 3.3: Evolution of turbine material temperatures and turbine inlet temperatures [3]

This value is supported by doing a similar analysis of data from Grilli et al. [55], which is shown in Figure 3.4 (note that this figure uses degrees Celsius). Assuming single-crystal cast alloys, a trend of 3K/year increase is seen, and an operating temperature of roughly 1085 °C in 2007. This would then give an AMOT of 1427 K in 2030. Although this is a slightly lower value, it is in the same order of magnitude meaning 1450 K is a reasonable value. Section 6.3 will perform a sensitivity analysis for the AMOT, such that the impact of a different value can be assessed.

Component maps

Compressors and turbines need to be able to operate over a wide range of conditions, with varying (corrected) mass flows and rotational speeds. The effect of these parameters on efficiency and pressure ratio is described by so-called component maps. The component maps are determined by their detailed design, such as blade shape, and thus making component maps is outside the scope of this research. This section is, therefore, about the use of component maps in parametric analysis, not how to make component maps.

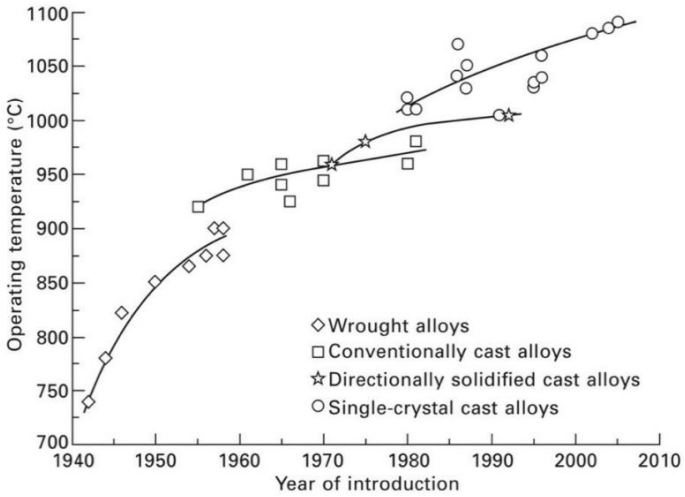

Figure 3.4: Evolution of turbine allowable material operating temperatures classified into different production methods [55]

In *pyCycle*, the component maps consist of arrays of data points, describing what combinations of corrected speed and mass flow lead to what pressure ratio and efficiency. To make this possible for the compressors, the operating region is split by so-called R-lines [56]. These lines run somewhat perpendicular to the constant speed lines but are drawn arbitrarily. The two outermost R-lines are the surge line and the choke line. Depending on the design point, the map is scaled to fit the input mass flow, PR and efficiency. By default, the design point is placed at 100% rotational speed and R-line 2.0, but to change off-design performance these values can be altered. The turbine maps do not have an R-line and altering their scaling can be done by selecting a different design speed and PR.

The component maps are defined using these tabular data. When an off-design point does not land on one of these data points, *pyCycle* interpolates to get an appropriate value. When an off-design value falls outside the defined field, *pyCycle* extrapolates to try and get a solution. However, these solutions should be taken with caution, as this extrapolated data is uncertain. Table 3.3 states the map scaling input values used for both the baseline and SIR APPU analyses. These values are chosen to ensure sufficient surge margin and to improve off-design performance.

Table 3.3: Turbomachinery maps design points

Parameter	LPC	HPC	HPT	LPT	PT
N_{mech} [%]	100	100	100	110	100
R-line [-]	2.7	2.1	N.A.	N.A.	N.A.

3.2.2. Combustor pressure loss

An essential component of any jet engine is the combustion chamber, where fuel is added in order to heat the working fluid. Inherent to a combustor is a pressure loss, for example due to friction between the gas and the wall. It is desired to keep this pressure loss to a minimum. A larger pressure loss has a detrimental effect on the engine performance. However, combustors have other design requirements as well, such as low emissions and flame stability. These aspects are beyond the scope of this research. For this reason, an appropriate value based on existing combustors is chosen.

However, this process is made difficult by the fact that it is not yet determined what type of combustor will be used. Therefore the value of 5% pressure loss used in the previous APPU design study is reused [19]. This value is supported by Liu et al. [57], who mention a typical range of 4% to 6% pressure loss for various types of combustors. To account for any further uncertainty, a sensitivity analysis is performed (Section 6.3.1).

4

The steam injection and recovery engine

With the baseline cycle and methods explained, the steam injection and recovery cycle can be explored. It is essential to understand the broad principle of what SIR is, and why one would want to implement it. With the SIR concept understood, it can be applied to the APPU. Next to that, Section 3.1.1 mentions that *pyCycle* is not yet able to model the SIR cycle, but the code can be expanded. Therefore, new methods and components are added to *pyCycle* such that the SIR cycle can be modelled. Lastly, these new components require realistic inputs. Similar to Section 3.2, approximate values for aspects such as efficiency and pressure loss are found. Section 4.1 explains the broad concept of the SIR cycle, after which the implementation in the APPU and the resulting architecture are explained in Section 4.2. Next, the *pyCycle* enhancement is treated in Section 4.3. The chapter concludes with the SIR cycle-specific components in Section 4.4.

4.1. Steam injection and recovery background and motivation

The Steam Injection and Recovery concept is about adding a semi-closed water cycle to the conventional Brayton cycle. This technology aims to decrease engine fuel consumption and NO_x emissions. This section first briefly mentions the use of only water or steam injection (Section 4.1.1), after which it explains the Steam Injection and Recovery Aeroengine (SIRA) and Water Enhanced Turbofan (WET) concepts as devised by Schmitz et al. [17] and Kaiser et al. [18] (Section 4.1.2). This also includes the aspects that make the SIR cycle advantageous, as well as its drawbacks.

4.1.1. Current and past use of water and steam injection

Water and steam injection technologies have already been employed in land-based gas turbines for power generation for decades, mostly with the goal of reducing NO_x emissions and increasing specific power [34, 53]. Land-based turbines can either inject liquid water or steam [34]. Water injected before the compressor has the purpose of decreasing the inlet temperature by means of evaporation, improving engine performance on hot days. Water injected in the combustion chamber reduces NO_x emissions by decreasing flame peak temperatures [33, 34, 53, 58]. However, this increases CO emissions due to the lower temperatures. Steam injected in the combustion chamber also reduces NO_x emissions but without the drawback of increased CO emissions, as it lowers the temperature less [34, 58, 59]. The amount of water or steam injected in the combustion chamber is limited by the compressor operability, as the added mass flow changes the turbine operation.

Water or steam injection has been studied and utilised since the beginning of the 20th century, first for its power augmentation capability and later for NO_x emissions reduction. Water injection has also briefly been applied to aircraft for thrust augmentation [53]. Jonsson & Yan [53] provide an extensive review of the history of studies and practical applications of water/steam injection in gas turbines.

4.1.2. Steam injection and recovery in aeroengines

The advantage of adding heated steam is utilised by the SIRA and WET concepts [17, 18, 58]. In these concepts, steam is injected into the combustion chamber and later extracted from the exhaust in liquid form. The recovered liquid water is converted to hot steam using heat exchangers, and injected into the combustor. This forms the semi-closed water cycle. The goal is to decrease the fuel consumption and NO_x emissions.

Part of the efficiency improvement of the SIR engine comes from reduced compressor work. A gas turbine operates by compressing air, adding heat energy by burning fuel, and expanding the flow in a turbine and by doing so it extracts power to drive the compressor (and load). Adding steam to the combustor substitutes part of the compressor mass flow, decreasing compressor work. The pressurisation of the water-steam cycle happens when the water is in its liquid state. The incompressibility of a liquid causes this pressurisation to require two orders of magnitude less power than compressing a gas [17].

Additionally, the higher steam concentration increases the specific heat capacity of the flow, meaning the turbines can extract more power from equal mass flow and Turbine Entry Temperature. This is equal to increasing the TET, which increases the specific work a turbine can do, but requires more advanced turbine materials or an increased cooling air fraction [17, 28]. This specific heat effect further reduces the required compressor mass flow.

The effects above are also true for engines with just steam injection. Now, to dive more into what sets the concepts analysed by Schmitz et al. [17] and Kaiser et al. [18] apart. Figure 4.1 shows a schematic of the SIRA concept [17]. Once power has been extracted by the turbine, the still-hot gas-steam mixture enters the hot side of a heat exchanger, the Heat Recovery Steam Generator (HRSG), which cools down the flow. Next, another heat exchanger extracts more heat energy from the flow in order to liquefy the water, after which the liquid water is collected. The collected water is deposited in a small buffer tank, after which it is pressurised. This pressurised water is fed into the cold side of the HRSG. The heat from the exhaust evaporates the water and heats the steam further up, such that it can be injected into the combustion chamber at elevated temperatures.

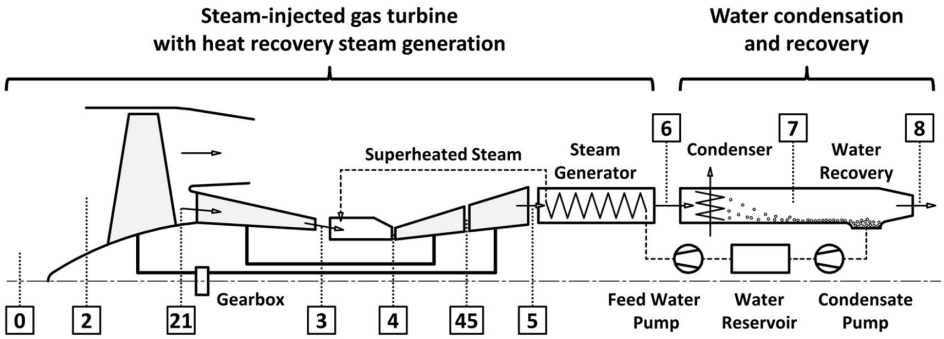

Figure 4.1: Schematic representation of the steam injection and recovery engine concept [17]

According to Schmitz et al. [17], the decrease in required compressor power and the heat recovery after the turbine result in a 20% decrease in SFC despite an assumed pressure loss of 10% across the HRSG and condenser. Kaiser et al. [18] calculated a 90% decrease in NO_x emissions due to the steam injection. However, there is a significant mass penalty. The turbomachinery is 15% lighter, but due to the added components, the total engine weight increases by 40%. The volume of the engine(core) increases as well [17, 58]. Due to this increased engine size and mass and other installation penalties, the reduction in mission fuel burn is only 15%. However, as said above, the compressor will be smaller due to reduced inlet mass flow, which reduces its efficiency. Also, any variation in the turbine cooling flow is not taken into account. Due to the higher specific heat more cooling air would be required, carrying an efficiency penalty. These two effects would lower the efficiency gain reported.

The technology required for this water recovery is still in its infancy. The water or steam injection is very advanced in its development, as it has extensively been applied in land-based gas turbines. However, the HRSG, condenser and water recovery are more novel technologies. Additionally, the analyses by Schmitz et al. and Kaiser et al. concern a turbofan engine, while this research is about an embedded turboshaft engine. The envisioned architecture of the SIR APPU is discussed below.

4.2. The steam injection and recovery APPU engine architecture

The SIR APPU engine is inherently different from the WET engines from Schmitz et al. [17] and Kaiser et al. [18] as it is a turboshaft engine and not a turbofan engine. Whereas Schmitz et al. and Kaiser et al.

could use the relatively cold bypass flow to condense the water, this is not an option for the SIR APPU engine due to the absence of a cold bypass flow. A different heat sink is required. As Section 4.3.3 already mentioned, the LH_2 fuel will be used for this purpose.

However, the potency of using the LH_2 fuel as a heat sink is limited. The fuel flow rate, PT exit temperature and heat exchanger effectiveness dictate how much heat can be extracted from the exhaust flow. To illustrate: with ϵ=1.0, Fuel-to-Air Ratio (FAR) =0.011 and assuming $C_{P,g}$=1.22 kJ/kg K and T=800 K at the PT exit, the flow can only be cooled down 100 K. This is not enough to cool down the flow sufficiently for water to liquefy.

For this reason, the PT exit flow is split in two: the main gas path, and the heat exchanger duct (HE duct). The ratio between these two mass flows will be called the Splitting Ratio (SR) and is an input of the parametric analysis. Equation 4.1 shows how SR is defined mathematically. The main gas path flows through a duct (with minor pressure loss) to the exhaust. The HE duct houses the HRSG and condenser & collector. Figure 4.2 shows a schematic of this engine.

$$SR = \frac{W_{HE}}{W_{main}} \tag{4.1}$$

The water collected from the HE duct does not go straight to the water compressor; it is first collected in a buffer tank. The water in this tank is assumed to be at a constant 2 bar and 330 K. The buffer tank is only modelled in the form of these two parameters. These two parameters are set constant to improve numerical stability and efficiency.

An essential drawback of using the LH_2 as the heat sink lies in the dual fuel capability of the APPU. As mentioned in Chapter 2, a design requirement of the APPU is that it should be able to operate both on hydrogen and on regular jet fuel. If the engine is being fueled with kerosene, there is no longer a heat sink available, and the water cycle comes to a stop. This is reflected in the inputs listed in Table 6.3: the SR is set to zero. The result is that the advantages of the water cycle are only applicable when the engine is running on hydrogen.

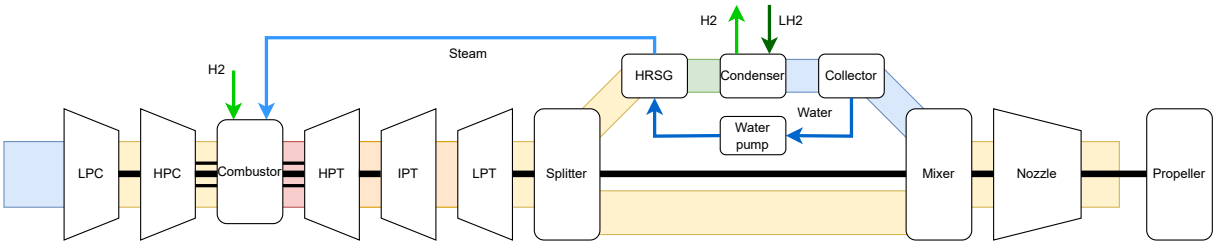

Figure 4.2: Schematic representation of the SIR APPU cycle

4.3. Steam injection and recovery in *pyCycle*

As explained in Section 3.1, the current version of *pyCycle* does not possess the capabilities to model the SIR cycle. This section describes the methods implemented into *pyCycle* such that it is able to do this. First, the properties of a pure water flow are treated in Section 4.3.1. Next, Section 4.3.2 explains the physics of heat exchangers and their use in the HRSG component. Then, the workings of the condenser are described in Section 4.3.3. After that, the pressurisation of water is mentioned by Section 4.3.4. This is followed by Section 4.3.5 where the intricacies of water injection in the combustor are explained. This section is concluded by Section 4.3.6 with an explanation of how all new components tie together numerically to form the SIR APPU *pyCycle* model.

4.3.1. Water properties

To enable *pyCycle* to model liquid water and the liquid-gaseous phase change, an additional thermodynamical properties model for water needs to be added. This section mentions what methods are used, and how they are implemented. A distinction is made between the calculation of properties for a pure water flow (Section 4.3.1), and the methods for condensing water in the exhaust (Section 4.3.1).

Pure water flow
The properties of the pure water flows are chosen to be calculated using the International Association for the Properties of Water and Steam (IAPWS) IF-97 method [60]. This method was chosen as it is commonly used in industry and for its simplicity, while still taking the effects of both temperature and pressure into account. The IAPWS IF-97 method takes the pressure and temperature and returns the corresponding properties, such as the specific enthalpy h and the specific isochoric heat capacity C_P.

Important to note is the inclusion of the phase change from liquid to gaseous or vice versa. This allows for the latent heat to be incorporated in calculations. The latent heat in the relevant pressure range (up to about 4 MPa) is in the order of $2{\cdot}10^3$ kJ/kg. For illustration, the C_P for liquid water is in the order of 4 kJ/kg, and for steam it is in the order of 2 kJ/kg. Including the latent heat is thus essential for accurate results.

Humid air flow
Whereas in a water-only environment, the boiling and condensation occur at the boiling temperature, it is more of a gradual process when other gasses are present. For example, there is water vapour in the air, despite it being far below the boiling temperature of water. Such an environment exists in the exhaust of an engine, where water vapour is present in a mixture of various gasses.

Usually, the exhaust is well above the boiling temperature of water. However, in the SIR APPU engine, (part of) the exhaust is cooled down to below the boiling temperature to allow for the extraction of liquid water. To ensure the accuracy of the analysis, it is required that the amount of condensed water is calculated correctly.

This is where the principle of the relative humidity (ϕ) comes in. The relative humidity indicates the level of saturation of the air with water vapour: ϕ=0 means there is no water vapour in the air, and ϕ=1 means the air is saturated. Adding more water vapour to saturated air will lead to ϕ>1, which causes water to condensate until ϕ=1 is reached again. The relative humidity is calculated using Equation 4.2 [17]:

$$\phi = \frac{x_{H_2O,g} P}{P_{s,v}(T)} \tag{4.2}$$

where $x_{H_2O,g}$ is the molar fraction of gaseous water, P is the static pressure, and $P_{s,v}(T)$ is the vapour pressure. The vapour pressure is approximated using the method from Sonntag [61], which uses Equation 4.3:

$$P_{s,v}(T) = exp(-6096.9385\,T^{-1} + 16.635794 - 2.711193{\times}10^{-2}\,T + 1.673952{\times}10^{-5}\,T^2 + 2.433502ln(T)) \tag{4.3}$$

where T is in Kelvin, and $P_{s,v}$ is in hPa. This equation is valid between 173.15 K and 373.15 K (-100°C and 100°C).

If ϕ can not be larger than 1, the maximum amount of water vapour in the flow occurs at ϕ=1. With this assumption, the maximum gaseous water molar fraction can be calculated for every temperature and pressure. This is illustrated in Figure 4.3 for P=$3.0{\times}10^4$ Pa. When $x_{H_2O,g}$ reaches unity, the boiling temperature at the particular pressure is reached. If the total water molar fraction in the flow is 0.2, condensation starts to occur below 309 K at this pressure. If this flow is cooled to 300 K, $x_{H_2O,g}$=0.12, meaning that 60% of the water remains gaseous, while 40% is condensed. Figure 4.3 also visualises how much further the flow needs to be cooled down compared to assuming all condensation occurs at the boiling temperature.

Utilising this method ensures realism in the condenser component (Section 4.3.3). This method is used to determine the amount of water that is condensed at a certain temperature and pressure. To calculate the latent heat released during this condensation, the method described in Section 4.3.1 is used.

4.3.2. Heat exchangers
A significant part of the SIR cycle is the addition of heat exchangers to the engine. This section dives into the relevant physics of HEs and states how these are implemented into the HRSG. The condenser, despite being an HE as well, is treated in Section 4.3.3 as it is significantly different from the HRSG due to the water condensation and collection.

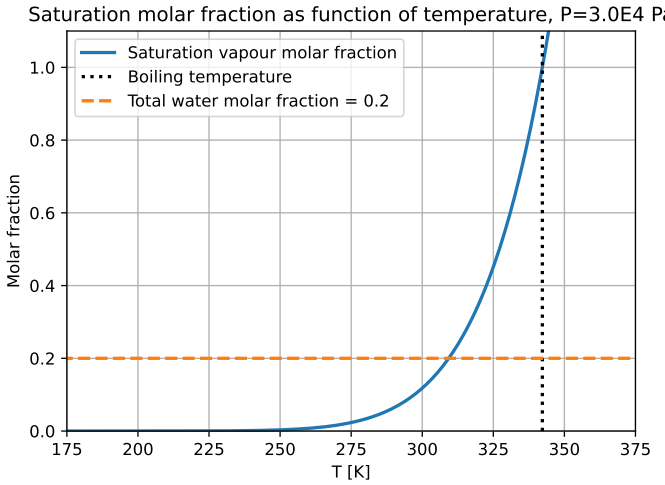

Figure 4.3: Illustration of the saturation water molar fraction as a function of temperature at P=3.0$\times 10^4$ Pa, highlighting the boiling temperature and molarfraction=0.2

The heat exchanger is, similar to other components, modelled as a black box with only a few design variables, and in- and output flows. The heat exchanger has two design parameters: the heat exchanger effectiveness (ϵ), and the flow pressure loss (dP). In a crossflow heat exchanger, ϵ is described by Equation 4.4. ϵ tells one how much of the theoretically maximum heat flux is utilised. The hot flow can not be cooled down further than the inflow temperature of the cold flow, and the cold flow can not be heated up further than the inflow temperature of the hot flow. The assumption made in Equation 4.4 is that of constant specific heat capacity. However, in *pyCycle* this assumption is not necessary. Also, a possible phase change is not taken into account in this form of the equation, something essential for modelling the SIR cycle.

$$E = \frac{Q}{Q_{max}} = \frac{W_h C_{P_h}(T_{in,h} - T_{out,h})}{C_{min}(T_{in,h} - T_{in,c})} = \frac{W_c C_{P_c}(T_{out,c} - T_{in,c})}{C_{min}(T_{in,h} - T_{in,c})} \tag{4.4}$$

where

$$\left.\begin{aligned} C_h &= W_h C_{P_h} \\ C_c &= W_c C_{P_c} \end{aligned}\right\} C_{min} = MIN(C_h, C_c)$$

Because of these shortcomings, Equation 4.4 is rewritten to Equation 4.5. This equation uses the flow enthalpies instead of the temperatures and specific heats. As *pyCycle* (with its *CEA* model) and IAWPS-97IF can accurately calculate the enthalpies including the phase change, the enthalpies accurately reflect the changes in internal energy.

$$E = \frac{W_h(h_{in,h} - h_{out,h})}{Q_{max}} = \frac{W_c(h_{out,c} - h_{in,c})}{Q_{max}} \tag{4.5}$$

where

$$\left.\begin{aligned} Q_h &= W_h(h_{in,h} - h_{h,T_{in,c}}) \\ Q_c &= W_c(h_{h,T_{in,h}} - h_{in,c}) \end{aligned}\right\} Q_{max} = MIN(Q_h, Q_c)$$

The HRSG is a relatively simple application of Equation 4.5: the enthalpies are calculated using the respective thermodynamical properties models which then gives the heat flux Q. As mentioned, this already takes possible evaporation into account. The gas side simply has a cooled-down flow as output, and the water flow has the following output parameters: pressure, temperature, mass flow rate, and water/steam fraction. The integration of this component is treated in Section 4.3.6.

4.3.3. The water condensation and collection

After the HRSG, the gas flow has been cooled down, but not enough to condense the steam. For this purpose, a condenser has to be implemented. This component (as implemented in *pyCycle*) also extracts the liquid water from the flow.

Section 4.3.1 describes how the amount of water condensed is calculated as a function of temperature. The inflow conditions of the condenser, such as composition, temperature and pressure, are known, allowing all calculations to be performed, resulting in the amount of water condensed. The difficulty lies in the computation of the reached temperature. Below the calculation procedure with its assumptions is explained, and Figure 4.4 shows a schematic representation of this process.

The condenser uses the fuel, liquid hydrogen, as the heat sink. It is assumed this hydrogen arrives at the condenser in liquid form at 20 K. The condenser works as a heat exchanger, meaning Equation 4.5 can be used to calculate the heat flux. The problem is slightly simplified, however. The Q_{max} is always that of the hydrogen, even if it is not the case. This was done to simplify the computation and prevent bound violations since a lower limit is imposed on the gas flow temperature. The thermodynamic properties model of *pyCycle* (the *NASA CEA* model) has a lower limit, which is 200 K. If this limit is exceeded, the results are no longer valid. When the liquid hydrogen is too potent of a heat sink, the heat flux is limited such that the gas temperature lower limit is not exceeded. If this occurs, the heat exchanger has a lower practical effectiveness.

The Q_{max} is calculated using the hydrogen properties from McCarty et al. [62]. This method is chosen, as opposed to the NIST-JANAF properties [63], as it takes pressure variations into account and also contains data for 20 K. It is assumed that the liquid hydrogen is pressurised beforehand to 4.00 MPa. This value is chosen as it is certain to be larger than the pressure in the combustion chamber (the highest pressure encountered is about 2.1 MPa, this can be deducted from the results stated in Table 6.8). At this pressure, the enthalpies at 20 and 300 K are 307.3 kJ/kg and 4244 kJ/kg respectively. Any variation from 300 K is accounted for with a constant specific heat capacity of 14.50 kJ/kg K. The C_P at 300 K is 14.41 kJ/kg K and remains below 15.00 kJ/kg K up to 1000 K, meaning 14.50 kJ/kg K is a fair assumption. Combining Q_{max} and the heat exchanger effectiveness gives the heat flux. This heat flux is used for both cooling down the flow and for the liquefication of water.

However, it is not yet known how much heat flux is utilised for each. For this, an iteration loop is used: a heat flux for cooling is specified, and the achieved temperature is calculated, then the amount of water condensed at this temperature is obtained, after which the condensation enthalpy is calculated. This iteration loop continues until $Q_{cooling} + Q_{condensation} = Q_{h2}$. The temperature lower limit is enforced by limiting $Q_{cooling}$. Once the loop is converged, the new temperature and the amount of liquid water are known for the next calculations.

To complete this component, the water collection takes place. Only the liquefied water is extracted. This water is (in *pyCycle*) fed to the water compressor. The remainder of the gas flow continues to be mixed with the main gas path.

An assumption made for this component is that no ice is formed. An analysis that is able to determine ice formation would require details about the HE design, which is outside the scope of this research. Ice buildup needs to be prevented as it will alter the workings of the HE, and likely increase dP. Therefore, when making a detailed design for the condenser & collector, ice formation needs to be accounted for, and prevented or minimised.

4.3.4. Water pressurization

Once the water has been collected, and before it enters the HRSG, it has to be pressurised. If this would happen after the HRSG, the flow would be (partly) gas, which requires more power to compress. A big part of the SIR concept is to pressurise the water in its liquid form to save power. Because the pressurisation of liquids is different than that of gasses, it requires its own component with its own physics. This section describes this component, the water compressor.

The incompressibility of water greatly simplifies calculations compared to the regular compressor. Additionally, the efficiency of this component is assumed constant, irrespective of parameters such as

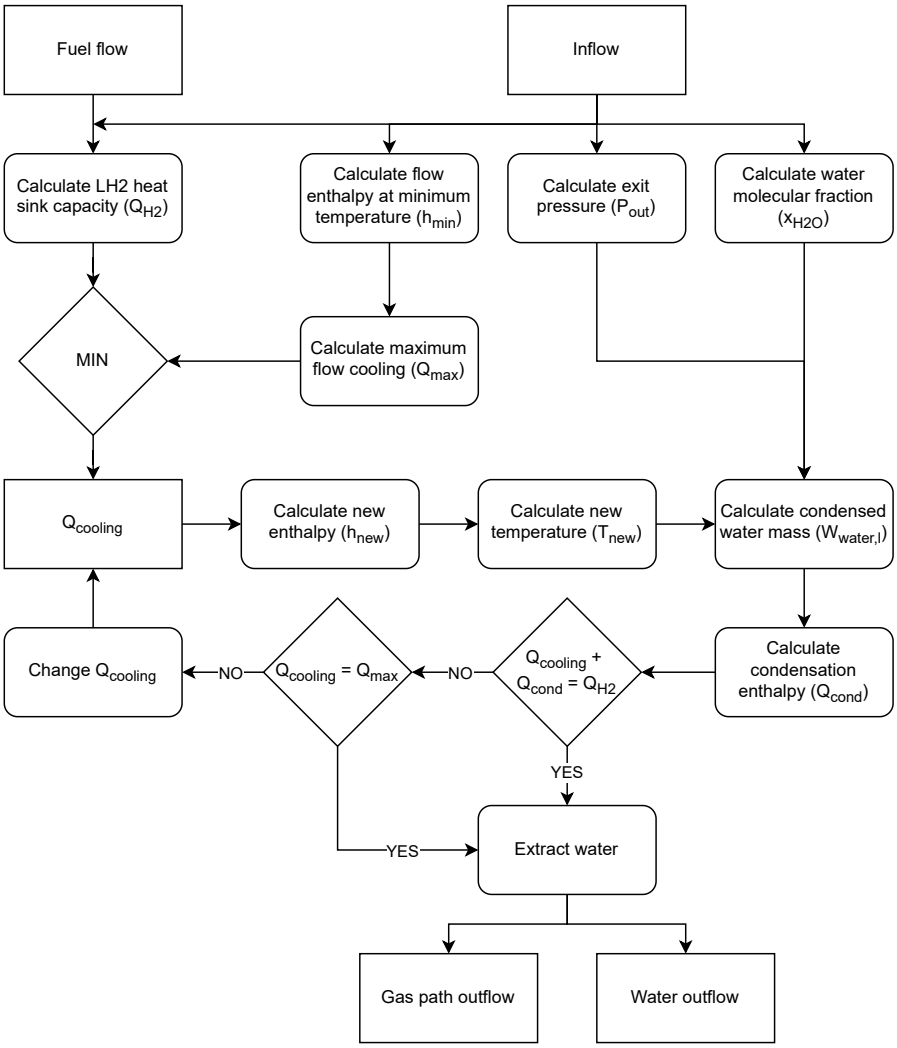

Figure 4.4: Schematic representation of the calculation procedure in the condenser & collector component

mass flow. Equation 4.6 describes the power required for the water pressurisation in the SIR APPU:

$$P = \frac{\Delta p \cdot Q}{\eta} \tag{4.6}$$

where P is the power required for compression in kW, Δp is the increase in pressure in Pa, Q is the water flow rate in L/s, and η is the efficiency. When using this equation, the density of water is assumed to be constant at 1000 kg/m^3. This power exerted onto the flow for pressurisation is reflected in an increase in enthalpy and, thus, temperature.

4.3.5. Water injection

Once the water has been collected, pressurised and (partially) evaporated, it can be injected back into the gas path. This happens in the combustor. The component discussed in this section, the water injector & combustor, fulfils this task. Below, the process as implemented in *pyCycle* is explained, and Figure 4.5 visualises it in a schematic.

For the sake of argument, it is assumed none or only part of the water is evaporated by the HRSG. This is the case for at least the design condition and take-off. This water has to be evaporated before it is

added to the flow in *pyCycle*, to ensure accurate enthalpy bookkeeping. The inability of *pyCycle* to handle liquid water would cause discrepancies if liquid water was added to the gas flow.

The water flow comes in with a certain pressure, temperature, mass flow rate and water/steam ratio. This is used to calculate its enthalpy. Then it is calculated how much heat flux is required to evaporate all liquid water, taking the combustor pressure loss into account in the determination of the boiling temperature. It is not necessary to find the equilibrium where the steam is at the same temperature as the air, because the described procedure is purely for numerical reasons.

This enthalpy is taken from the gas flow, in the same manner as in the heat exchangers. If too little enthalpy is present, for example when too much water is injected, the gas flow could be 'cooled down' to below the minimum temperature of *pyCycle*, resulting in (convergence) errors. For this reason, the water injector & combustor in this form will only work with limited amounts of liquid water.

Once all water is evaporated, and its pressure and temperature are known, it can be handed over to the thermodynamic properties model of *pyCycle*. With both flows in the same thermodynamics model, they are mixed. The last step of this component is to increase the temperature to the desired TET by adding and combusting fuel, similar to the regular combustor.

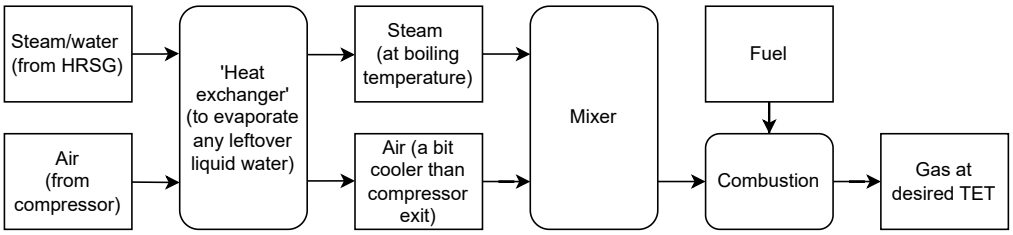

Figure 4.5: Schematic representation of the water injector & combustor component as implemented in *pyCycle*

4.3.6. Numerical integration

With all individual components implemented, the complete SIR APPU engine can be 'constructed'. This section discusses the characteristics and limitations of the SIR cycle implementation in a *pyCycle* model. When *pyCycle* runs the analysis, it always goes from front to back. This poses a problem however as the water flows forward, from aft of the turbines and HEs to the combustor. The lack of a calculated water flow would prohibit the calculation of the whole engine. This is prevented both by limiting the number of parameters required for the water flow, and by imposing initial guesses for the first iteration.

The first, limited parameters, is possible because the water flow does not use the thermodynamic model of *pyCycle*. The only data required when using the IAPWS 97IF water properties model are the pressure, temperature, mass flow rate and water/steam fraction. The latter, imposing initial guesses, is enforced by how *pyCycle* is coded. *pyCycle* requires every parameter used for a calculation to have a default value as it is put into the function. The fact that only a limited amount of parameters is required helps as only a few initial guesses are needed.

However, the unfortunate result is that the water cycle essentially always runs one iteration cycle behind. This is mitigated by the fact that the solver used in *pyCycle* converges to small tolerances. This means that the second to last iteration cycle has inputs very close to those of the last iteration cycle, limiting the error in the water cycle.

A problem arising from *pyCycle* itself when implementing the SIR cycle is that a zero mass flow causes numerical instabilities and prevents a solution from being reached. This problem occurs when modelling the kerosene and HEs off conditions, where SR=0. To avoid this issue, the SR is set to 0.005. This is large enough to prevent numerical instabilities, and sufficiently small to only have a negligible impact on the results.

4.4. Component efficiencies

In addition to the efficiencies for the conventional components, there are also efficiencies for the described new components. A close example is the pressure loss in a heat exchanger. This section finds efficiencies

and methods to calculate them for the new components. The considered aspects all have a significant impact on the engine cycle or are otherwise required for answering the research question. First, a method for estimating the NO_x emissions reduction due to steam injection is introduced in Section 4.4.1. Next, Section 4.4.2 finds the effectiveness, pressure loss and specific mass of the heat exchangers.

4.4.1. NO_x reduction

Adding steam to the combustion chamber inlet can decrease the NO_x emissions. This is, for example, caused by the reduction in peak flame temperatures, because the steam increases the specific heat. The method used to determine the extent to which the steam reduces the NO_x emissions is derived using data from Xue et al. [64]. They used Computational Fluid Dynamics (CFD) to develop a chemical reactor network which could predict NO_x emissions and used this to investigate the effect of steam injection on NO_x emissions. This model was applied to a kerosene Rich-burn Quick-quench Lean-burn (RQL) combustor.

The product of their research that is used is Figure 4.6. Similar to how the trend for the turbomachinery efficiencies is made, an equation is constructed that describes the normalised NO_x emissions as a function of the Water to Air Ratio (WAR), Equation 4.7.

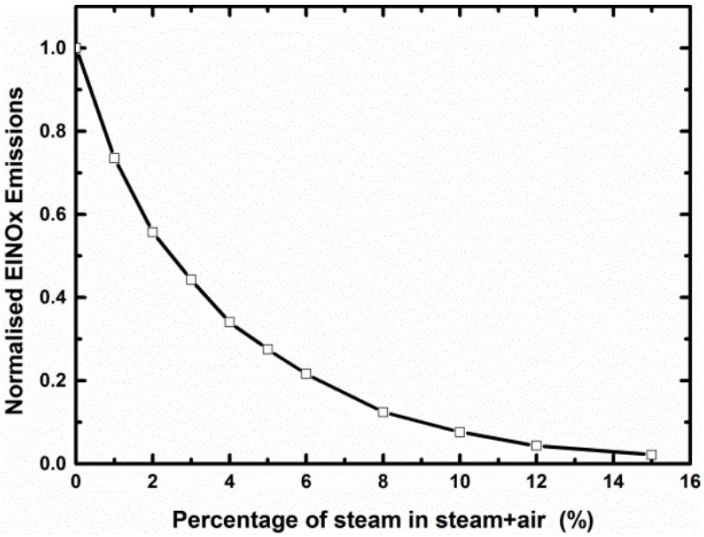

Figure 4.6: Influence of steam dilution on the overall NO_x emission [64]

$$relative\_NO_x = 1 \cdot 10^{-6}x^6 - 6 \cdot 10^{-5}x^5 + 1.2 \cdot 10^{-3}x^4 - 1.26 \cdot 10^{-2}x^3 + 7.7 \cdot 10^{-2}x^2 - 0.3337x + 1 \quad (4.7)$$

where

$$x = \frac{W_{steam}}{W_{air} + W_{steam}} \cdot 100$$

The data from Xue et al. is chosen over the methods from Kyprianidis et al. [65] and from Kaiser et al. [18]. Both these methods found a correlation based on empirical data. The data from Xue et al. is from a validated CFD model, meaning it has less uncertainty, and more is known about its origin and application.

However, as mentioned, this research applies to a kerosene RQL combustor. The exact type of combustor envisioned for the APPU is not yet known, but an RQL type is not among the (top) candidates[1]. The type and detailed design of a combustor have a driving impact on the NO_x emissions [57]. Additionally, the different combustion characteristics of hydrogen and kerosene affect the NO_x emissions significantly [66]. The NO_x reduction estimations done using the mentioned method therefore carry a considerable uncertainty, but nevertheless still offer an indication of the improvement.

[1] Personal correspondence with Arvind Gangoli Rao on 1st of March 2024

4.4.2. Heat exchangers

The heat exchangers are a key part of the SIR APPU engine, in the form of the HRSG and the condenser. The physics of heat exchangers are explained in Section 4.3.2, and how those physics are applied in the HRSG and condenser is elaborated in Section 4.3.2 and Section 4.3.3 respectively.This section discusses the two key design parameters of these components that have a significant impact on the engine performance. The first is the heat exchanger effectiveness (ϵ), and the second is the heat exchanger pressure loss (dP). These two parameters are intertwined and also influence the weight of the heat exchanger. Figure 4.7 shows this correlation [67]. Note, for example, how an engine with a heat exchanger with ϵ=0.7 and dP=10% has the same mass as one with a heat exchanger with ϵ=0.5 and dP=4%.

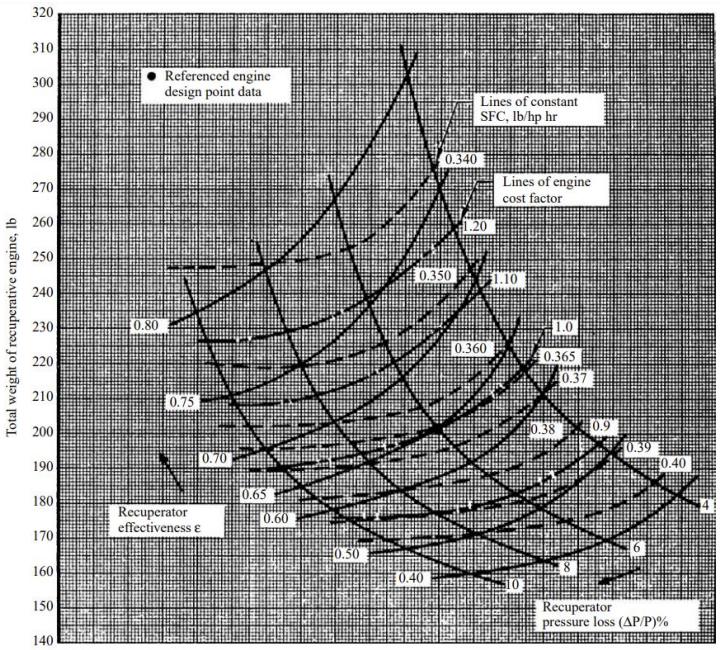

Figure 4.7: Relations between heat exchanger effectiveness, pressure loss and weight, for a 1000 hp helicopter turboshaft [67]

What lacks in Figure 4.7 is the weight of the HE itself. Next to that, this figure is from 1971 and thus is outdated. A more recent analysis produced Figure 4.8 [68], where the specific recuperator matrix weight is related to heat exchanger effectiveness, and the type of heat exchanger. It does however not contain any specification of the according pressure loss.

The pressure loss of a heat exchanger depends on many design variables, such as the effectiveness, but also more specific variables, such as the matrix architecture and tube shape. Next to that, both the HRSG and condenser of the SIR APPU are multiphase-flow heat exchangers, something not yet applied to aero engines [17, 18]. Designing a heat exchanger is outside the scope of this thesis, leaving these parameters unspecified and the pressure loss uncertain.

For this reason, a value for the pressure loss is chosen that is used by comparative analyses. Andriani et al. [69] performed a parametric analysis of an intercooled recuperated turbofan. A multitude of ϵ were used (0.6, 0.7 and 0.8), and the pressure loss was set constant at 5% on each side (hot and cold) of both heat exchangers. It is important to note that these are gas-to-gas heat exchangers. A more relevant analysis by Schmitz et al. [17] used 10% pressure loss over both the HRSG and condenser, which is approximately 5% over each. An advantage of comparing to the latter analysis is the similarity in the heat exchanger application. The chosen default value for the HE pressure loss is 5%. This parameter does carry much uncertainty with it. Therefore, a sensitivity analysis will be performed in Section 6.3.2.

The heat exchanger effectiveness offers slightly more certainty. Whereas land-based gas turbines with heat exchangers often employ $\epsilon > 0.9$, aero engines operate with lower values, often around $\epsilon = 0.7$ and not exceeding $\epsilon = 0.8$ [69, 70]. Land-based gas turbines are not much restricted in HE volume and weight, allowing different HE designs and higher ϵ. This is indicated by Figure 4.8 as well.

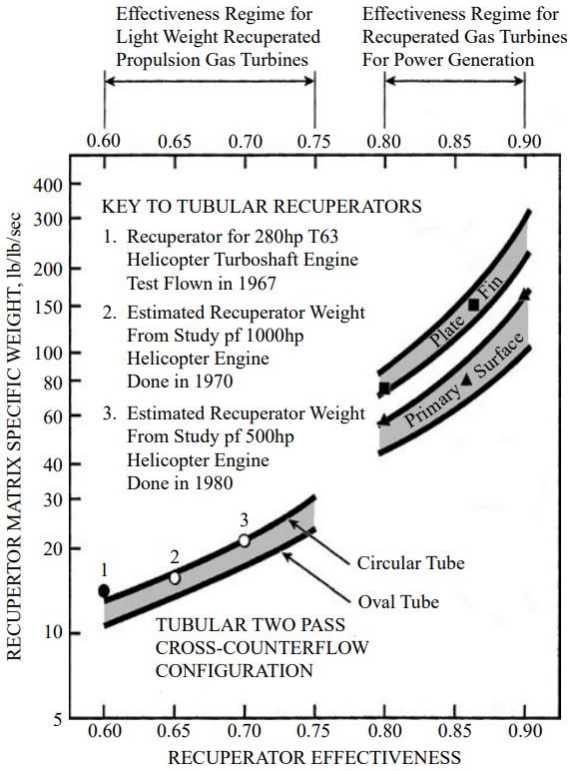

Figure 4.8: Relations between heat exchanger effectiveness and specific matrix mass [68]

As will be explained in Section 4.3.6, only part of the exhaust flow will pass through the heat exchangers. This will lower the sensitivity of pressure loss and HE weight on engine performance and overall mass. This is proven quantitatively by comparing Figure 6.8 and Figure 6.15. The influence of increasing ϵ from 0.7 to 0.8 does, however, have a significant impact on the NO_x reduction, as is shown by Figure 6.14. Therefore, $\epsilon = 0.8$ is chosen as the default value for the heat exchangers.

Next to these two parameters for the cycle calculations, it is required to know something about the mass of these heat exchangers. For this, Figure 4.8 is used. For an ϵ of 0.8, using extrapolation, the specific matrix mass is approximately 30 lbm/(lbm/s), or kg/(kg/s) [69]. However, this is only the mass of the matrix, not yet including components such as tubing to and from it. This adds approximately 25% [70], meaning a total of 37.5 kg/(kg/s) specific HE mass.

5

Verification and validation

The methods described in Chapter 3 and Section 4.3 are potent tools for calculating the performance of the baseline and SIR APPU. However, it is not yet known whether these methods produce realistic results. This chapter aims to Verify and Validate (V & V) the used methods. First, this is done for the engine model of the baseline cycle in Section 5.1. Then, the new components added to *pyCycle* such that the SIR cycle can be modelled are verified in Section 5.2. Due to the lack of an existing SIR turboshaft engine, or even a comparable analytical study, the *pyCycle* SIR model can not be validated.

5.1. Baseline cycle verification and validation

The *pyCycle* analysis software is introduced in Section 3.1.1. Previous research by Hendricks & Gray [37] proves *pyCycle*'s accuracy, meaning the analysis tool itself is sufficiently validated. Something not yet verified is the correct working of the engine model made in *pyCycle*. The baseline core APPU has an architecture that is already common in existing engines. Therefore, this architecture is present in *Gasturb*, allowing comparison between the two softwares. This existing model in *Gasturb* is assumed validated.

The baseline core APPU inputs (Table 6.2) are copied into *Gasturb*. If the *pyCycle* model is constructed correctly, the results should be similar, if not equal. Table 5.1 states the numerical results for both *pyCycle* and *Gasturb*. It is clear that the differences are negligible, verifying the correct setup of the *pyCycle* model.

Table 5.1: Baseline core results comparison between *pyCycle* and *Gasturb*

Parameter	*pyCycle*	*Gasturb*	Difference
SFC [kg/kWh]	0.0674	0.0675	+0.15%
W_{inlet} [kg/s]	3.777	3.773	-0.11%
$\eta_{thermal}$ [%]	44.5	44.4	-0.15%
A_{nozzle} [m^2]	0.0935	0.0932	-0.32%

Verifying the correct use and working of the component maps is also important. Therefore, the off-design conditions are analysed using *Gasturb* as well. Similar to *pyCycle*, *Gasturb* has a library of component maps to choose from. However, none of the compressor maps resembles a centrifugal compressor, such as illustrated in Figure 2.11, the type of compressor used for the HPC of the APPU. The *pyCycle* component maps are imported into *Gasturb* to remedy this. This has the added benefit that the verification aspect is more valid due to the larger degree of input similarity. Table 5.2 states the differences between *pyCycle* and *Gasturb* analyses for selected parameters for all off-design conditions.

Although larger than the design condition, the differences are minor for the off-design conditions as well. The considerable differences in the APU-modi are noteworthy. This is likely due to slight discrepancies in the map scaling. Because the APU-modi operating points lie far away from the design operating points, this slight discrepancy has a significant impact on the results.

Also noteworthy is that the kerosene operation differences are larger than the hydrogen operation differences. This is likely caused by the different thermodynamic properties models of *pyCycle* and *Gasturb*.

Table 5.2: Baseline core off-design results comparison between *pyCycle* and *Gasturb*

Condition / Output parameter	H_2 take-off	H_2 APU-modus	Kerosene cruise	Kerosene take-off	Kerosene APU-modus
Power	+0.64%	+6.27%	+2.25%	+4.62%	+9.02%
SFC	-0.07%	-4.43%	+4.03%	+3.07%	-2.00%
W_{inlet}	+0.36%	+1.81%	+2.09%	+3.65%	+3.50%
OPR	+0.42%	+2.06%	-0.76%	+1.07%	+2.75%
A_{nozzle}	-0.39%	-0.40%	-0.39%	-0.39%	-0.39%

These models calculate different compositions at the high-temperature combustor exit, resulting in a specific heat discrepancy of 2.2% in the kerosene cruise condition. This causes a difference in performance. How a specific heat discrepancy is linked to performance differences is explained in Section 7.1. Because hydrogen has no carbon emissions, its combustion products are less prone to be calculated differently by the different models. This results in a smaller discrepancy in C_P and, thus, smaller performance discrepancies.

5.2. *pyCycle* enhancement verification and validation

For the SIR APPU results to have value, it needs to be verified that the new components are modelled correctly and work as intended. This section dives into the water properties (Section 5.2.1) and HE (Section 5.2.2) implementations. The remaining components were verified by checking their outcomes with manual calculations.

5.2.1. Water properties

The water thermodynamical properties model, the IAPWS-97IF model [60], is described in Section 4.3.1. This model is assumed to be validated, meaning only correct implementation needs to be verified. The *IAPWS* has an online calculation tool [1] which is used to check the results. The results are found to be the same, thus verifying the correct implementation of the IAPWS-97IF method.

However, such a freely available tool does not exist for the vapour pressure. Similar to the IAPWS-97IF model, the method by Sonntag [61] is assumed to be validated. A way to verify the correct implementation of the vapour pressure is by comparing it with the IAPWS-97IF method at boiling temperature. With ϕ=1 and x_{H_2O}=1, the vapour pressure should equal the static pressure. The IAPWS-97IF method calculates the boiling temperature for a particular static pressure, and calculating the vapour pressure with this temperature should give the same value as the static pressure. It is found that this is the case, thus verifying the correct implementation of Sonntag's method for the vapour pressure.

5.2.2. Heat exchangers

The heat exchangers assume a counterflow configuration. With such a configuration it is possible that the outflow temperature on the cold side is higher than the outflow temperature on the hot side. If it were a gas-to-gas or liquid-to-liquid HE, this would not pose any problems. However, if a phase change occurs in the HE, this might not be the case: the temperature of the cold side could locally surpass the temperature of the hot side. This is because the HRSG and condenser are modelled as a single HE element, where only calculations using the in- and outputs are done. This section investigates whether this crossover occurs, thereby aiming to validate the ϵ assumption of 0.8.

In the design condition, the HRSG does not impose a problem, as the gas outflow temperature is 632 K and the water outflow temperature is 596 K, meaning it is impossible for the cold flow to have a higher temperature than the hot flow locally. The same situation occurs in the H_2 take-off condition. There, the gas outflow and water outflow temperatures are 698 K and 641 K, respectively. The last condition that utilises the HRSG is the H_2 APU-modus. However, as stated in Table 6.8, no water is recovered in this condition. The input of ϵ=0.8 is thus valid for the HRSG.

[1] IAWPS calculation tool home page, http://www.iapws.org/relguide/IF97-Rev.html, last accessed 16-05-24

However, this problem could occur in the condenser: In the design condition, the gas gets cooled to 264 K while the hydrogen fuel gets heated to 512 K. The temperature progression throughout the condenser is calculated to verify that the cold-side temperature does not locally surpass the hot-side temperature. Figures 5.1 through 5.3 show the results of this analysis by means of plotting the temperature of both flows as a function of how much heat transfer has occurred. This is similar to the temperature progression from front to back in a HE but normalised for the heat transfer such that detailed parameters such as the local heat transfer rate are not required.

In the analysis, the gas flow C_P is assumed to be constant at the value of the condenser inflow. For a range of temperatures, it is calculated how much heat flux is required to reach a specific temperature, taking the water condensation into account (as described in Section 4.3.1 and Section 4.3.3). The latent heat released during the condensation is what causes the kink in the temperature progression of the gas path. The enthalpy calculations of the hydrogen are as explained in Section 4.3.3, apart from some extra data points added between 20 K and 300 K. Because the hydrogen is assumed to be pressurized to 4.0 MPa, there is no distinguishable temperature plateau where evaporation occurs, as 4.0 MPa is above the critical pressure of hydrogen (which is 1.29 MPa) [62].

Figures 5.1 and 5.2 show that the temperature difference does not change sign in both the design (cruise) and take-off condition. In the APU-modus, no water is recovered (see Table 6.8); this is confirmed by Figure 5.3 as well: the gas flow temperature progression has no kink, indicating there is no condensation. Additionally, the lowest gas temperature is above 400 K, which is above the boiling temperature at near-atmospheric pressure. These findings all indicate that ϵ=0.8 is valid.

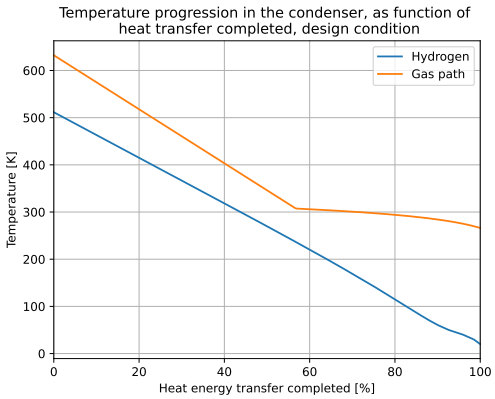

Figure 5.1: Temperature progression in the condenser, as a function of heat transferred, design condition

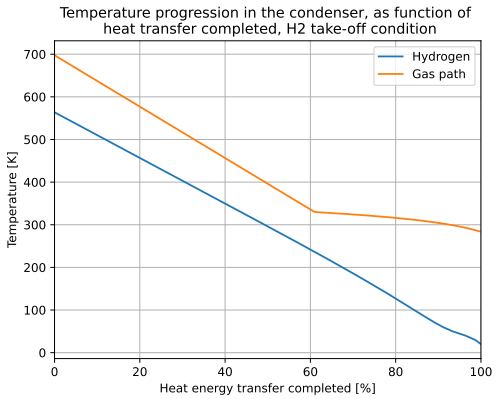

Figure 5.2: Temperature progression in the condenser, as a function of heat transferred, H_2 take-off condition

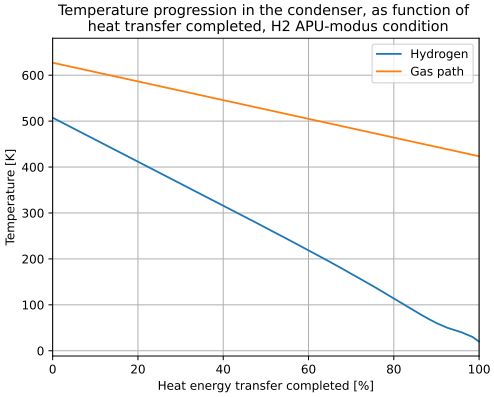

Figure 5.3: Temperature progression in the condenser, as a function of heat transferred, H_2 APU-modus condition

6

Results

The baseline APPU engine model is constructed in *pyCycle* and verified to be working accordingly, as well as the required new components and the SIR APPU engine model. This chapter will state the design conditions and inputs (Section 6.1), and the resulting engine performance (Section 6.2). Additionally, the sensitivity to selected parameters of both cycles is presented in Section 6.3. Note that this chapter primarily focuses on presenting the results and explaining the trends in the sensitivity analyses, whereas Chapter 7 will give more detailed explanations of particularities observed.

6.1. Design conditions and inputs

Chapter 2 describes the context of the engine. This context dictates the performance requirements in the on- and off-design conditions. This section states these conditions, how they came to be, and what the driving engine parameters are.

All design conditions are stated in Table 6.1. The cruise condition is derived from the nominal cruise condition of the A321neo: a flight Mach number of 0.78 at an altitude of 33 kft (10 km) [14]. The electrical power and compressed air for auxiliary systems will still be generated by the main engines. This is because these engines are larger and, therefore, less affected by these off-takes. Take-off is logically at sea level. The APU-modus means the APPU is fulfilling the functionalities of a conventional APU; providing around 250 kW of electrical power and 0.5 kg/s compressed air [19]. The flight altitude and Mach number are specified for every condition. Table 6.1 also gives a selection of engine parameters for each condition. These are the parameters that drive the engine operation, such as output power and SFC, with emphasis on showing how these parameters change for the different conditions. The driving performance requirement is the power requirement in the design condition (H_2 cruise): P=2200 kW.

Noticeable are the significant differences in pressure ratios, both for the intake and for the nozzle. As mentioned in Chapter 2, the engine is embedded in the tail, with its intake inside the fuselage boundary layer. This causes a significant pressure drop as compared to free-stream air. During take-off and APU-modus the boundary layer is smaller, hence the smaller pressure drop [20].

The pressure ratio at the nozzle is a result of the aerodynamics around the tail cone. At the tip, where the APPU nozzle is located, there is a higher-than-ambient total pressure zone. This requires the total pressure of the APPU exhaust to be higher as well [1]. Due to the lower aircraft speeds during take-off and APU-modus the required PR is smaller for those conditions.

Most of the values of the TET and PRs were taken from the previous design study. A significant change was made in the HPC PR however. It was lowered from 6.0 to 4.5. This was deemed a more realistic value [2]. Section 6.3 will investigate whether the chosen TET is good or should be changed.

Table 6.2 shows the extensive list of the more detailed component inputs for the *pyCycle* analysis. Most of these inputs are kept the same as the previous iteration of APPU. The **bold** parameters are driving inputs in the design condition, but depend on the designed engine in the off-design conditions. Table 6.3 shows the additional inputs required for the SIR cycle-specific components.

[1] Personal correspondence with Alexander Heidebrecht on 7th of December 2023

[2] Personal correspondence with Arvind Gangoli Rao on 30th of April 2024

Table 6.1: Defining characteristics of the analysed conditions

Condition Input parameter	H_2 cruise (design)	H_2 take-off	H_2 APU-modus	Kerosene cruise	Kerosene take-off	Kerosene APU-modus
Mach number [-]	0.78	0.10	0.0	0.78	0.10	0.0
Altitude [kft]	33	0	0	33	0	0
TET [K]	1700	1700	900	1700	1700	920
PR_{intake} [-]	0.78	0.98	0.98	0.78	0.98	0.98
PR_{nozzle} [-]	1.336	1.135	1.050	1.336	1.135	1.050
Bleed-offtake [-]	0.0	0.0	0.15	0.0	0.0	0.15

Table 6.2: Component inputs for the *pyCycle* analyses (**bold** values are design-condition-only inputs)

Pressure loss	Value [%]
LPC-HPC duct	1.5
Combustor	5.0
HPT-LPT duct	1.0
LPT-PT duct	1.0
PT-nozzle duct	2.0

Pressure Ratio	Value [-]
LPC	**5.8**
HPC	**4.5**

Shaft speed	Value [rpm]
HP-shaft	**15000**
LP-shaft	**8000**
PT-shaft	6000

Bleed fraction	Value [-]
Leakage	0.005

Efficiency	Value [%]
Combustor	100
HP-shaft	99.5
LP-shaft	99.5
PT-shaft	99.5

Flow Mach number	Value [-]
Inlet	**0.50**
LPC	**0.50**
LPC-HPC duct	**0.50**
HPC	**0.40**
Bleed	**0.40**
Combustor	**0.28**
HPT	**0.40**
HPT-LPT duct	**0.40**
LPT	**0.40**
LPT-PT duct	**0.40**
PT	**0.40**
PT-nozzle duct	**0.50**

6.2. Results

With the design conditions and component inputs specified in Section 6.1, the engine performance can be calculated. Firstly, the baseline APPU performance is stated, after which it is compared with comparable existing turboshaft and turboprop engines. Next, the SIR APPU performance is stated, and this section is concluded by comparing the baseline APPU and SIR APPU performances.

6.2.1. Baseline results

The component efficiencies are absent from Table 6.2. These parameters are calculated using the methods described in Section 3.2, and the two cycles have minor discrepancies. Therefore they are stated separately. Table 6.4 lists them for the baseline APPU. The resulting performance of the baseline APPU is summarized in Table 6.5.

Table 6.3: Additional input parameters of the SIR APPU engine in *pyCycle*

Parameter	Value [unit]
SR	0.13 [-]
E_{HRSG}	0.8 [-]
$dP_{HRSG,g}$	5 [%]
$dP_{HRSG,w}$	5 [%]
$E_{condenser}$	0.8 [-]
$dP_{condenser}$	5 [%]
$P_{watertank}$	2E5 [Pa]
$T_{watertank}$	330 [K]
$PR_{watercompressor}$	20 [-]
$\eta_{watercompressor}$	90 [%]
dP_{main}	0.02 [-]

Table 6.4: Calculated component isentropic efficiencies of the Also peculiar are the differences between the constant and variable efficiencies for the lower-TET analyses. For example, the combination of TET=1300 K and OPR=40 gives zero NO_x reduction when analysing with constant efficiencies, while a 5% NO_x emissions reduction is calculated when efficiencies are updated. This difference can be attributed to the same effect that causes the OPR trends that is explained above: the difference in HPC discharge temperature. If the efficiencies are updated, they are significantly higher at low TET due to the low SP. This reduces the resulting HPC discharge temperature, increasing ΔT and, thus, FAR. A higher FAR results in more water recovered. This effect is only noticeable at low TET because then the efficiency differences are significant, and the ΔT is already small, so a small change can have a big impact. APPU for the 'Advanced' component technology level and AMOT=1450K

Component	Base efficiency [-]	Cooling air fraction [-]	Cooling air efficiency penalty [-]
LPC	0.890		
HPC	0.880		
HPT	0.914	0.046	0.028
LPT	0.917	0.004	0.002
PT	0.930	0.000	0.000

Table 6.5: Baseline APPU performance results calculated with *pyCycle*

Condition / Output parameter	H_2 cruise (design)	H_2 take-off	H_2 APU-modus	Kerosene cruise	Kerosene take-off	Kerosene APU-modus
Power [kW]	2200	5273.4	263.0	1935.7	4158.3	258.7
SFC [kg/kWh]	0.06744	0.07145	0.18018	0.18571	0.20251	0.49623
W_{inlet} [kg/s]	3.777	9.890	4.254	3.534	8.527	4.170
OPR [-]	25.71	20.57	5.463	24.44	18.01	5.445
$\eta_{thermal}$[%]	44.5	42.0	16.7	45.0	41.3	16.9

Lastly, the engine mass is calculated by *Gasturb*. The geometrical design of the engine is outside the scope of this research, so these inputs in *Gasturb* were determined in cooperation with Prof. Dr. Arvind Gangoli Rao . The calculated mass is 502 kg, and Figure 6.1 shows the preliminary geometric design of the APPU. Note the PT-shaft exiting the engine through the front, contrary to what is envisioned for the APPU. The lack of architectural flexibility of *Gasturb* prohibits making this correct. This might affect the

resulting engine mass, introducing uncertainty in the estimated value. However, the magnitude of this uncertainty is beyond the scope of this project as it involves detailed geometrical design.

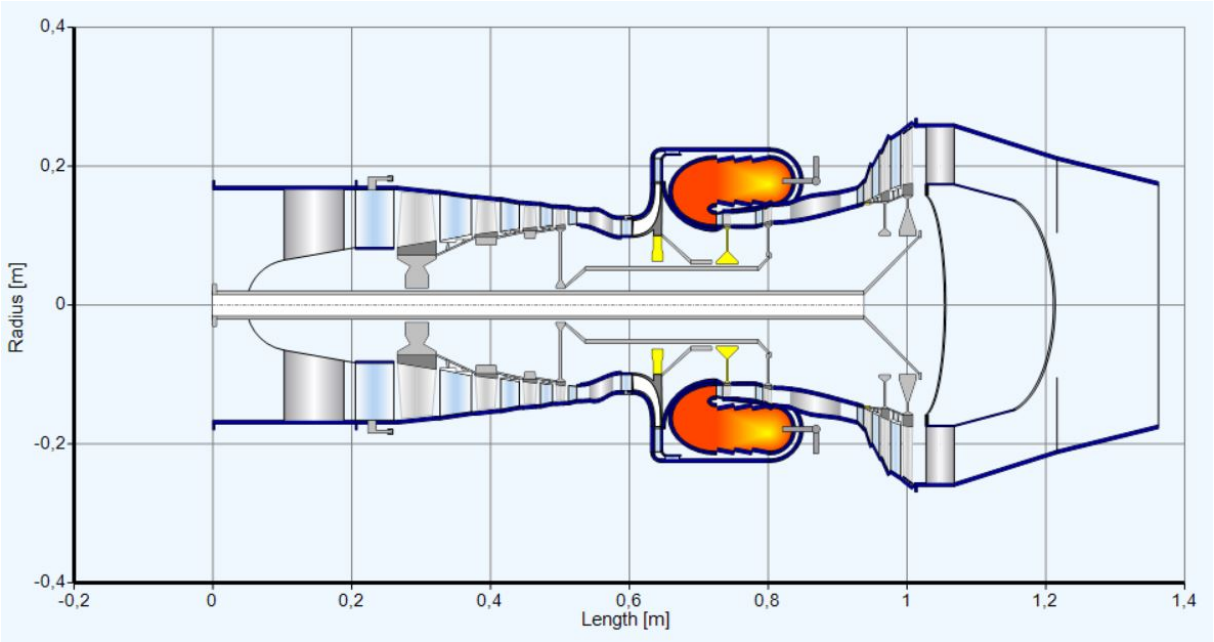

Figure 6.1: Preliminary geometric design of the APPU generated by *Gasturb*

The baseline APPU is found to have a thermal efficiency of up to 45.0%. This efficiency is reached during the kerosene cruise condition, with the hydrogen cruise operation close behind. This discrepancy is caused by slightly different component efficiencies, as can be seen in Appendix A. $\eta_{thermal}$ is noticeably lower during take-off, which is caused by the reduced OPR, which in turn is a result of the component maps. Note the drastically lower $\eta_{thermal}$ of the APU-modi. This is not unexpected, as the engine is running on approximately 5% of its power capability.

However, does the performance make sense at all? Are these realistic values? The performance of the baseline APPU is therefore compared with the performance of existing turboprop and turboshaft engines. Due to the scarcity of extensive detailed engine data, only the take-off results are compared. Any exhaust thrust contribution is ignored. Table 6.6 lists a number of engines currently in service. These engines were selected because their power output is somewhat similar. This data is used to compare the baseline APPU performance. The SFC is reported in terms of $\eta_{thermal}$ as this allows for easy comparison with the APPU hydrogen operation results. Notable are the significant differences in $\eta_{thermal}$: The APPU has a $\eta_{thermal}$ between 7 and 13 per cent points higher than these existing engines. However, these engines were designed some time ago, meaning engine technology has significantly improved. This can even be observed in the listed data: A newer engine such as the T408 from 1989 has a higher thermal efficiency than the oldest engine (T56-A427) from 1954. The power-to-weight ratio of the listed engines varies significantly: between 4.1 and 11.2 kW/kg. The baseline APPU is calculated to have a maximum power-to-weight ratio of 10.5 kW/kg, which is within and at the upper end of the observed range. This comparison aims to place the performance of the baseline APPU in the context of existing engine performance numbers. The mass is determined to be a reasonable value, within the range of existing engines. The thermal efficiency, however, is significantly higher than any of the reported engines. Part of this increase can be attributed to the significant gap in (targeted) EIS: the APPU is to be introduced 24 years after the TP-400-D6. A performance improvement of 11.8% achieved after 24 years of innovation, which is significant. Part of this is because of the increased turbomachinery efficiencies, despite the smaller size. Also, the APPU does not suffer from any power and bleed-air off-take in the analyses of this research, while this could have a significant impact. Whether these two aspects explain the full 11.8% efficiency increase is not determined.

Table 6.6: Performance data of existing turboprop and turboshaft engines

Parameter Engine [source of data]	EIS	Take-off power [kW]	Take-off $\eta_{thermal}$ [%]	Engine mass [kg]
PW150 [71]	1995	3730	31.8	718
T56-A427 [71]	1954	4283	29.3	880
AE 2100D3 [71]	1997	3377	29.9	746
T408 [3]	1989	5600	34.4	501
T700/T6E [3]	1978	1775	31.8	244
TP-400-D6 [19, 72]	2006	7971	39.8 [4]	1938

6.2.2. SIR APPU results

Now for the SIR APPU: The SIR APPU engine has similar requirements as the baseline core APPU engine. All flight conditions, both on- and off-design, are thus stated in Table 6.1. However, when the engine operates using kerosene, or the HEs are inoperative, the SR is set to zero. Section 4.3.6 states that the LH_2 fuel is used as the heat sink for the condenser. When the engine operates on kerosene, this heat sink is thus no longer present, rendering the condenser ineffective. The result is that no water can be recovered. To limit the pressure losses between the PT and nozzle, the complete flow is directed through the main duct.

As mentioned previously, the SIR APPU core is slightly different and thus has marginally different efficiency inputs. These are listed in Table 6.7. The resulting SIR APPU performance, including the HE-inoperative conditions, is stated in Table 6.8.

Table 6.7: Calculated component isentropic efficiencies of the SIR APPU for the 'Advanced' component technology level and AMOT=1450K

Component	Base efficiency [-]	Cooling air fraction [-]	Cooling air efficiency penalty [-]
LPC	0.890		
HPC	0.879		
HPT	0.913	0.047	0.028
LPT	0.917	0.005	0.002
PT	0.930	0.000	0.000

The slightly lower (design) core mass flow as compared to the baseline APPU means the core of the SIR APPU is marginally smaller, with a mass of 480 kg.The core is, however, only part of the mass of the SIR APPU; the mass of the new components also needs to be added. The total mass of the SIR APPU is calculated using Equation 3.1. In Section 4.4.2 a value for the specific mass of a heat exchanger is given: 37.5 kg/(kg/s) [69, 70]. The maximum mass flow through the HRSG and condenser occurs at H_2 take-off. Then 10.06*0.13=1.31 kg/s flows through both components, meaning both components have a mass of 49.0 kg. This brings the total mass of the SIR APPU to 581 kg. What is not yet included in this mass estimation is all the additional tubing for the water and steam cycle, a water buffer tank, and the water compressor. A size and mass estimation of these components is outside the scope of this project.

[3] *GE Turbines and small Engines Overview*, GE global research company presentation, https://arpa-e.energy.gov/sites/default/files/14_deBock_GE%20Turbines%20and%20small%20engines%20overview%20-%20ARPA-e%20INTEGRATE%20V2.pdf#page=5, last accessed 16-6-2024

[4] Cruise thermal efficiency

Table 6.8: SIR APPU performance results calculated with *pyCycle*

Condition / Output parameter	H_2 cruise (design)	H_2 take-off	H_2 APU-modus	Kerosene cruise	Kerosene take-off	Kerosene APU-modus
Power [kW]	2200	5263.3	231.6	1813.6	3746.1	228.6
SFC [kg/kWh]	0.06640	0.07031	0.18963	0.18529	0.20774	0.52027
W_{inlet} [kg/s]	3.620	9.459	3.856	3.283	7.826	3.783
OPR [-]	25.71	20.52	5.097	23.37	17.02	5.083
$\eta_{thermal}$ [%]	45.2	42.7	15.8	45.2	40.3	16.1
W_{water} [g/s]	46.0	117	0.0	0.0	0.0	0.0
Relative NO_x [-]	0.666	0.672	1.0	1.0	1.0	1.0

Condition / Output parameter	H_2 cruise HEs off	H_2 take-off HEs off	H_2 APU-modus HEs off
Power [kW]	2094.2	4832.2	263.2
SFC [kg/kWh]	0.06695	0.07197	0.17788
W_{inlet} [kg/s]	3.543	9.058	3.949
OPR [-]	24.84	19.40	5.278
$\eta_{thermal}$ [%]	44.8	41.7	16.7
W_{water} [g/s]	0.0	0.0	0.0
Relative NO_x [-]	1.0	1.0	1.0

6.2.3. Baseline-SIR comparison

With the performances of both the baseline and SIR APPU known, a comparison can be made. This is essential for one to be able to assess whether it might be worth the effort of implementing the SIR cycle into the APPU. This will show the gains that will be obtained with the SIR cycle. Possible drawbacks might also appear, such as larger engine mass. Table 6.9 states the on-design performance of the baseline and SIR appu, and lists the differences. Table 6.10 states the differences between the baseline and SIR APPU for the off-design conditions. The H2-operation-HE-off conditions of the SIR APPU are compared with the H2-operation conditions of the baseline APPU as there is no direct baseline APPU condition to compare with.

Table 6.9: Comparison of the baseline and SIR APPU design condition results

Parameter	baseline cycle	SIR cycle	Difference
SFC [kg/kWh]	0.0674	0.0664	-1.54%
W_{inlet} [kg/s]	3.777	3.637	-3.70%
Relative NO_x [-]	1.0	0.666	-33.4%
Mass [kg]	502	581	+15.7%
baseline components [kg]	502	483	-3.70%
HEs [kg]	0	98	N.A.

The data in Table 6.9 shows that only minor SFC improvement can be obtained. Also, the Specific Power (SP) is only marginally higher. This higher SP is reflected in the mass of the baseline components (the compressors, combustor and turbines), which is slightly lower for the SIR APPU. The slight decrease in core mass is, however, offset by the mass of the heat exchangers, making the total mass of the SIR APPU 79 kg higher than that of the baseline APPU, a 15.7% increase.

The slight decrease in SFC is not unexpected. The pressure losses through the HRSG and condenser

Table 6.10: Comparison between the baseline and SIR APPU results for all design conditions

Condition / Output parameter	H_2 cruise (design)	H_2 take-off	H_2 APU-modus	Kerosene cruise	Kerosene take-off	Kerosene APU-modus
Power	0.00%	-0.19%	-11.9%	-6.31%	-9.91%	-11.6%
SFC	-1.54%	-1.60%	+5.24%	-0.23%	+2.58%	+4.84%
W_inlet	-4.16%	-4.36%	-9.36%	-7.10%	-8.22%	-9.28%
OPR	0.00%	-0.24%	-6.70%	-4.38%	-5.50%	-6.65%
Relative NO_x	-33.4%	-32.8%	0.00%	0.00%	0.00%	0.00%

Condition / Output parameter	H_2 cruise HEs off	H_2 take-off HEs off	H_2 APU-modus HEs off
Power	-4.81%	-8.37%	+0.08%
SFC	-0.73%	+0.73%	-1.28%
W_inlet	-6.20%	-8.41%	-7.17%
OPR	-3.38%	-5.69%	-3.39%
Relative NO_x	0.00%	0.00%	0.00%

have a slight detrimental effect on the engine performance.This is offset, however, by the benefits of the heat recovery and steam injection, Section 4.1 explains how. The compressors require 68.2 kW less power, and the HRSG reclaims 128 kW of heat energy. Regarding performance, the SIR cycle implementation thus offers minor gains. Where the water cycle makes a significant difference is in the NO_x emissions: a 33.4% reduction. This could help with reaching the ACARE goals mentioned in Chapter 1.

The efficiency improvement of the SIR cycle is also present during take-off, with a similar relative NO_x reduction as well. However, during AP-modus there is a significant performance drop, with less power, higher SFC and no NO_x reduction. This is because the FAR is too low for condensation to occur in the condenser, leaving only the detrimental effect of additional pressure losses. The other conditions, where the SIR cycle is not utilised, are only slightly affected in their SFC. However, the power output is significantly reduced. This is likely because the water concentration through the turbines is lower than in the design condition. This effect is already observed in the baseline APPU results when the hydrogen and kerosene results are compared. In the SIR APPU, the kerosene operations have a lower water concentration both due to the different combustion products and due to the lack of steam injection. The latter causes a power output decrease when comparing the baseline and SIR APPU. This lack of steam injection is also prevalent in the HEs off conditions, where the power is reduced despite using hydrogen. An explanation for why reduced water content decreases power output is given in Section 7.1.

6.3. Sensitivity analyses

Both Section 3.2 and Table 6.2 contain many inputs for the engine cycle, with even more inputs added in Section 4.4 specific to the SIR cycle. All these inputs carry uncertainty, either for their realism or because one might want different engine parameters for the APPU. To account for these uncertainties and make the results more useful, sensitivity analyses are performed. Additionally, it shows how sensitive the engine performance is to certain parameters. First, the sensitivities of the baseline core APPU are investigated in Section 6.3.1, followed by the SIR core APPU in Section 6.3.2.

6.3.1. Baseline

For the baseline core, conventional input parameters are varied in order to study its sensitivity to them — parameters such as the OPR and TET, efficiencies and pressure losses. First, the combination of OPR and TET is investigated, followed by the AMOT. Next, the turbomachinery TL is varied to study the effect of component efficiencies, and this section is concluded by looking at the impact of pressure losses in the inlet duct and combustor. For convenient comparison, the y-scales of the last four analyses are equal.

OPR and TET

In order to gain insight into the influence of OPR and TET on the performance of the baseline core engine, a sensitivity analysis for these two parameters was performed. Here, the OPR and TET were varied between 10 and 50, and between 1300 K and 2200 K, respectively.

This analysis is done for two variations: one with and one without updating the component efficiencies and cooling air requirement. The analysis with constant efficiencies serves to be a more straightforward comparison with results in literature, as the efficiencies are generally not a variable. However, updating the efficiencies and cooling air requirements does give valuable insight into the practical implications of high OPR and TET. A higher OPR leads to smaller components as the air is compressed more and thus lowers efficiencies. A higher TET both increases the efficiency penalties and decreases the mass flow. The latter results in smaller components, therefore reducing component efficiencies. The results with constant efficiencies are shown in Figure 6.2 and those with varying efficiencies in Figure 6.3.

One can clearly see in Figure 6.3 that the efficiency penalties start to make a difference above a TET of 1700 K. The components become small due to the high SP, lowering efficiency, and significantly more cooling air is required, further decreasing the efficiencies of the turbines. The component efficiencies and cooling fractions are shown in Appendix B. From this analysis, it is clear that a TET of 1700 K is well-suited for the APPU. Together with TET=1600 K, it has the lowest SFC for OPR≈25, but has a higher SP which leads to a smaller engine.

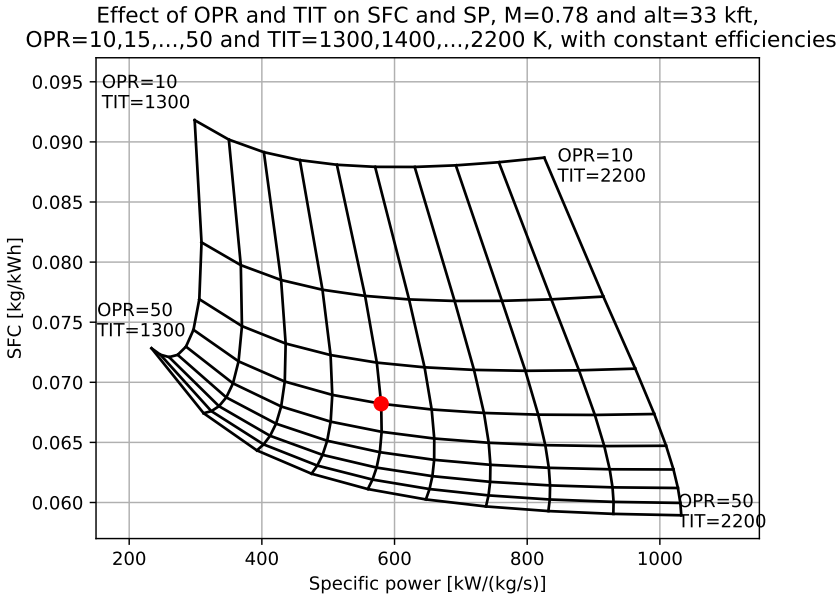

Figure 6.2: Effect of OPR and TET on the SFC and SP of the APPU, OPR between 10 and 50, TET between 1300 K and 2200 K, with constant component efficiencies (the red dot indicates the default OPR and TET)

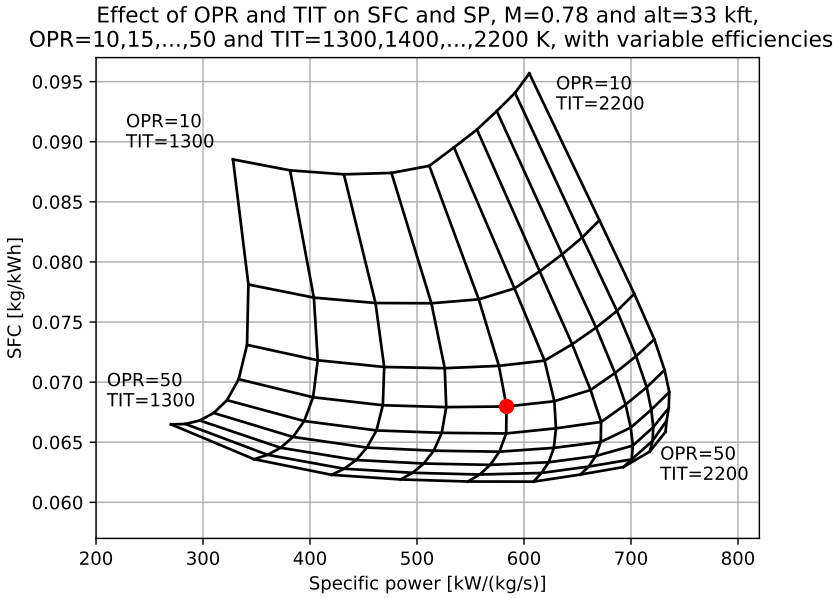

Figure 6.3: Effect of OPR and TET on the SFC and SP of the APPU, OPR between 10 and 50, TET between 1300 K and 2200 K, with variable component efficiencies (the red dot indicates the default OPR and TET)

Maximum turbine material temperature

Section 3.2.1 explains why turbine cooling is required, and also why it is beneficial to limit the cooling air required as much as possible. Equation 3.4 shows that the material temperature plays an important role in determining the cooling air requirement. However, the turbine AMOT is a parameter that carries uncertainty, as is discussed in Section 3.2.1. For this reason, a sensitivity analysis is performed for the turbine AMOT.

In order to more clearly show the trend in the performance impact of the turbine AMOT, a wide range has been used in the sensitivity analysis: from 1100 K to 1700 K. The upper limit is the turbine entry temperature, meaning that no cooling air will be required. This is confirmed by Figure 6.4. The impact on engine performance is shown in Figure 6.5.

The trends in Figure 6.4 and Figure 6.5 are as expected: a higher turbine AMOT results in less cooling air required, which improves overall engine performance. Note how the engine performance is more sensitive to the AMOT in the lower AMOT range. This is because then the cooling air required increases for all three turbines, resulting in a three-time efficiency penalty.

Turbomachinery technology level

As one would expect, the efficiencies of the compressors and turbines play an essential role in the overall performance of the engine; higher efficiencies result in higher SP and lower SFC, as will be shown in the following analysis. Section 3.2.1 explains the method used to determine the efficiency of a component based on its size. However, there is still uncertainty; components of similar size could have different efficiencies depending on their TL. The following sensitivity analysis aims to show the impact of the different turbomachinery technology levels on engine performance.

In Section 3.2.1 three technology levels are mentioned: 'Current', 'Advanced' and 'Future'. All other analyses use the 'Advanced' TL. Table 6.4 states the efficiencies for all components at this TL. Tables 6.11 and 6.12 list the efficiencies for the 'Current' and 'Future' TLs, respectively. The engine performance for the three TLs is shown in Figure 6.6. The trends observed are as expected: increased turbomachinery efficiency results in improved engine performance.

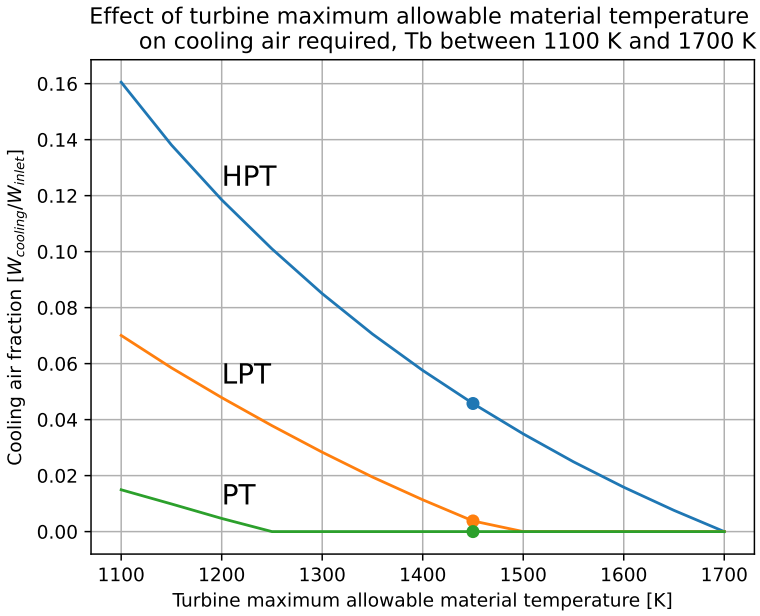

Figure 6.4: Effect of AMOT on the cooling air fraction of the APPU, AMOT between 1100 K and 1700 K

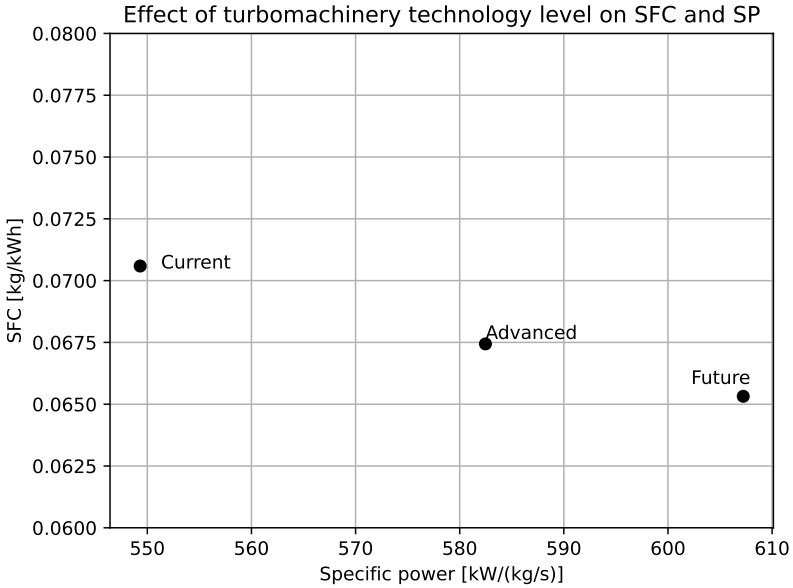

Figure 6.6: Effect of technology level on the SFC and SP of the APPU

Inlet pressure recovery

Chapter 2 discusses the integration of the APPU into the A321 airframe. It mentions the inlet location of the inlet ductand its consequent boundary layer intake. The result of this is a significant total pressure loss of 22%. However, changes in aircraft, inlet duct or engine design might change the total pressure ratio between the compressor face and free-stream air. This sensitivity is performed to shed light on the impact of a different pressure loss. Additionally, one might want to put the APPU engine in a different application.

These are the reasons behind the chosen PR range: 0.65 to 1.0. The resultant engine performance is shown in Figure 6.7. The trend is as expected: increased engine performance with improved pressure recovery. Similarly to the turbine AMOT, the inlet PR has a significant impact on the engine performance.

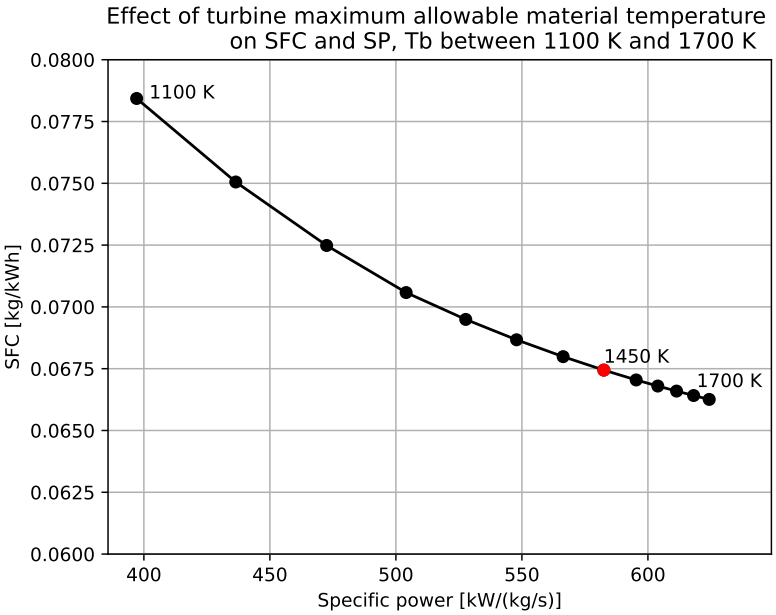

Figure 6.5: Effect of AMOT on the SFC and SP of the APPU, AMOT between 1100 K and 1700 K

Table 6.11: Calculated component isentropic efficiencies of the baseline APPU for the 'Current' component technology level and AMOT=1450K

Component	Base efficiency [-]	Cooling air fraction [-]	Cooling air efficiency penalty [-]
LPC	0.865		
HPC	0.857		
HPT	0.896	0.046	0.028
LPT	0.898	0.004	0.002
PT	0.913	0.000	0.000

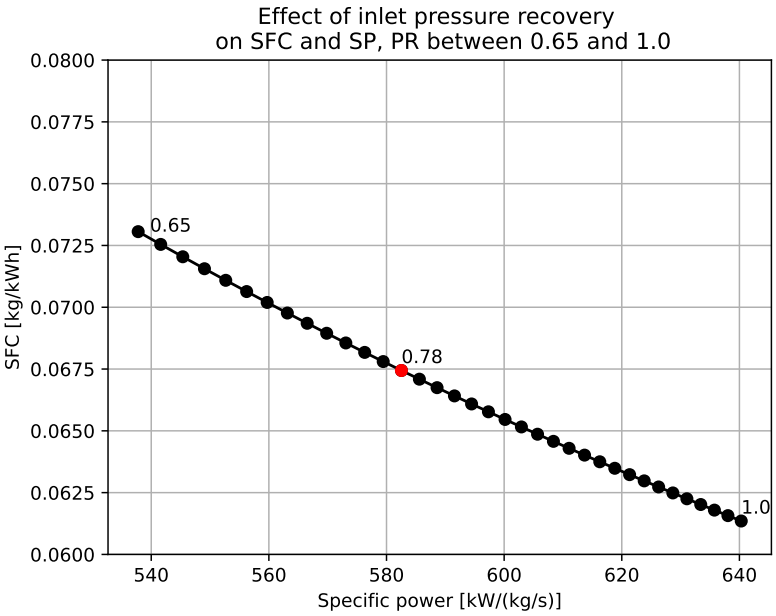

Figure 6.7: Effect of inlet pressure recovery on the SFC and SP of the APPU, PR between 0.65 and 1.0

Table 6.12: Calculated component isentropic efficiencies of the baseline APPU for the 'Future' component technology level and AMOT=1450K

Component	Base efficiency [-]	Cooling air fraction [-]	Cooling air efficiency penalty [-]
LPC	0.908		
HPC	0.899		
HPT	0.928	0.046	0.028
LPT	0.930	0.004	0.002
PT	0.943	0.000	0.000

Combustor pressure loss

Figure 6.8 shows the effect of varying the combustor pressure loss on engine performance. The trend here is as expected: less pressure loss results in better engine performance. When comparing with Figure 6.7, it can be seen that the combustor pressure loss has less of an impact than the inlet pressure recovery. This is, however, mostly due to the larger magnitude of the pressure loss variation in the inlet.

The important knowledge that can be taken from this sensitivity is that one or two per cent extra combustor pressure loss only has a minor effect on the engine performance. If this margin could allow for a combustor with, for example, lower NO_x emissions, it helps a designer in a trade-off to know what the performance penalty is.

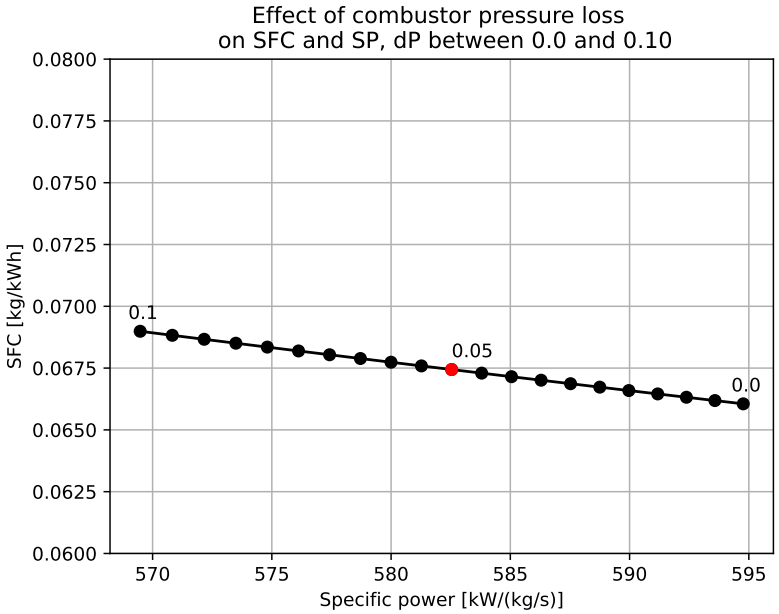

Figure 6.8: Effect of combustor pressure loss on the SFC and SP of the APPU, dP between 0.0 and 0.1

6.3.2. Steam injection and recovery

Similar to the baseline APPU, it is important to know the impact of changing a parameter on the SIR APPU performance. Contrary to the sensitivity analyses of the baseline core, more extensive explanations for the trends observed are provided. This is because the trends are not as easily recognized and understood. Note, however, that apart from the OPR-TET sensitivity analysis, all parameters are different from those in Section 6.3.1. This is because the impacts of changing these parameters are expected to be similar and thus do not require an additional analysis for the SIR APPU. This section starts with the OPR and TET sensitivity, followed by the SR sensitivity. Next, the heat exchanger effectiveness is varied, after which the

effect of heat exchanger pressure losses is investigated.

OPR and TET

The reason the OPR-TET sensitivity is investigated for the SIR cycle as well is that the added components and their effect on the cycle are much influenced by their inflows. Changing either the OPR or TET can drastically change the PT exit flow. Next to that, a different TET affects the FAR of the engine, and thus the heat sink capability of the condenser as well as the gas flow water content, resulting in it being able to condense a different amount of water.

The OPR and TET ranges are equal to those used for the baseline APPU: OPR between 10 and 50, and TET between 1300 K and 2200 K. The results for the analysis with constant efficiencies are shown in Figure 6.9 and those for updating efficiencies in Figure 6.10. These results are similar to the baseline core APPU OPR-TET sensitivity: higher OPR decreases SFC, and higher TET increases SP. Also, the difference between constant and variable efficiencies is similar.

In addition to the SFC and SP, is the NO_x emissions reduction, an important performance metric for the SIR APPU in this research. How the NO_x emissions vary can be influenced by the OPR and TET. The results from the analysis with constant efficiencies are shown in Figure 6.11 and those for updating efficiencies in Figure 6.12. It can be seen that with higher TET, the relative NO_x emissions decrease, and with higher OPR, the relative NO_x emissions increase. Important to realise is that these values are relative to a cycle with equal OPR and TET but without steam injection.

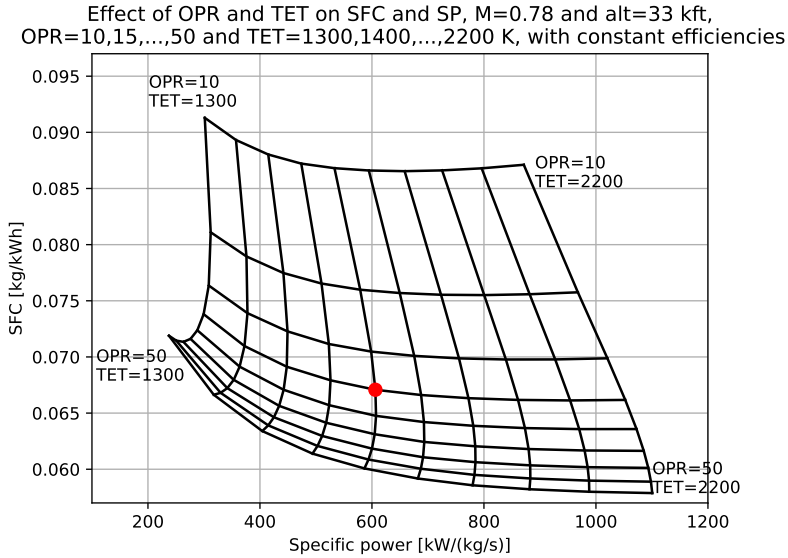

Figure 6.9: Effect of OPR and TET on the SFC and SP of the SIR APPU, OPR between 10 and 50, TET between 1300 K and 2200 K, with constant component efficiencies (the red dot indicates the default OPR and TET)

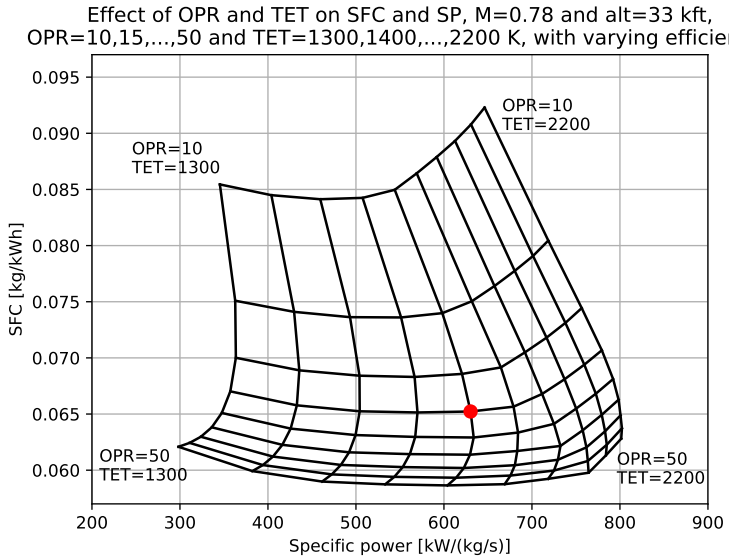

Figure 6.10: Effect of OPR and TET on the SFC and SP of the SIR APPU, OPR between 10 and 50, TET between 1300 K and 2200 K, with variable component efficiencies (the red dot indicates the default OPR and TET)

These found trends can be explained. If one increases the TET, the temperature increase in the combustor becomes larger. A bigger ΔT requires a relatively larger amount of fuel: a higher FAR. A higher FAR helps to decrease the relative NO_x emissions in two ways. The first is that it results in a higher concentration of water vapour in the exhaust. The second is that a higher FAR means there is a relatively larger heat sink in the condenser, allowing lower temperatures to be reached and more water to be condensed. Both effects increase the amount of water recovered and thus decrease the relative NO_x emissions. Note that this is a NO_x emissions reduction compared to an engine with equal TET and OPR but without steam injection. The reduction is larger at high TET, but the absolute NO_x emissions of such a cycle are likely to still be high compared to cycles with lower TET.

The reasoning behind the OPR trend is similar. With a higher OPR, the HPC discharge temperature is higher, resulting in a smaller ΔT in the combustor (for equal TET). This then leads to a smaller FAR, which results in less water captured and thus less NO_x reduction. This effect is, therefore, more prominent than that of the lower PT discharge temperature. A higher OPR means the temperature ratio over the turbines is larger as well, meaning a decreased turbine discharge temperature (for equal TET cases). This lowers the cooling requirements of the HEs. However, this does not matter, since there is less water to extract in the first place.

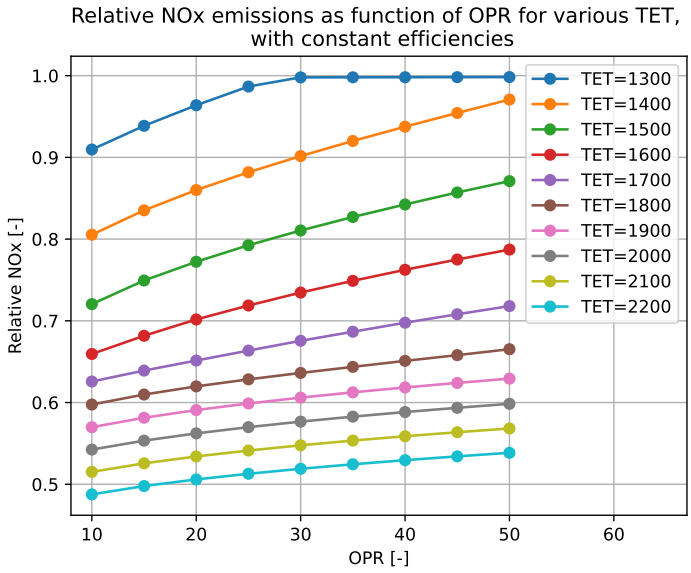

Figure 6.11: Effect of OPR and TET on the relative NO_x emissions of the SIR APPU, OPR between 10 and 50, TET between 1300 K and 2200 K, with constant component efficiencies

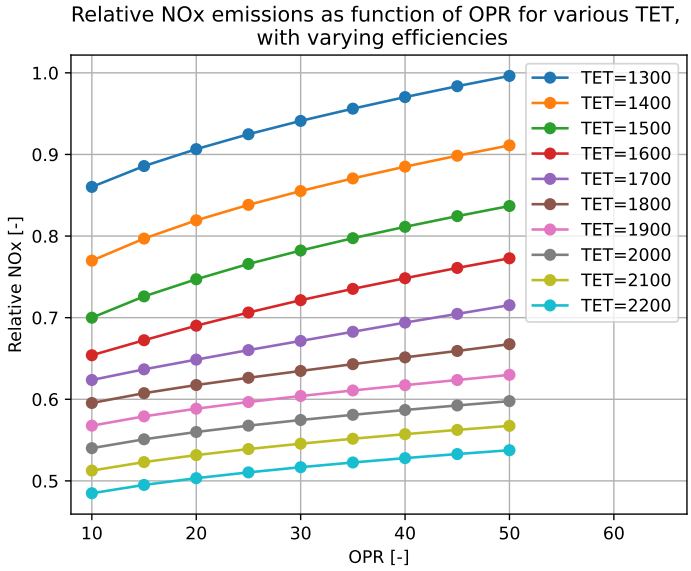

Figure 6.12: Effect of OPR and TET on the relative NO_x emissions of the SIR APPU, OPR between 10 and 50, TET between 1300 K and 2200 K, with variable component efficiencies (the red dot indicates the default OPR and TET)

Also peculiar are the differences between the constant and variable efficiencies for the lower-TET analyses. For example, the combination of TET=1300 K and OPR=40 gives zero NO_x reduction when analysing with constant efficiencies, while a 5% NO_x emissions reduction is calculated when efficiencies are updated. This difference can be attributed to the same effect that causes the OPR trends that is explained above: the difference in HPC discharge temperature. If the efficiencies are updated, they are significantly higher at low TET due to the low SP. This reduces the resulting HPC discharge temperature, increasing ΔT and, thus, FAR. A higher FAR results in more water recovered. This effect is only noticeable at low TET because then the efficiency differences are significant, and the ΔT is already small, so a small change can have a big impact.

SR

An important parameter for both the HRSG and condenser is the mass flow rate that passes through them. It dictates how much heat energy can be transferred into the water and the LH_2 fuel, and how much water can be extracted. This analysis aims to both gain insight into this balance, as well as potentially find an optimum SR. The selected range of SR is from 0.01 to 0.25. Ideally, the lower limit would be zero, but that causes numerical instabilities. The impact of SR on SFC, SP, relative NO_x and recirculated water is shown in Figure 6.13.

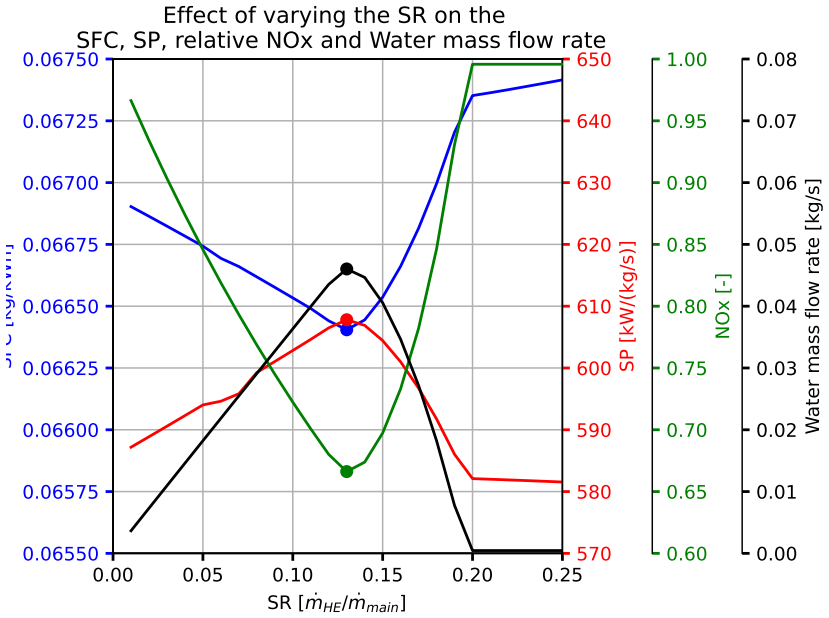

Figure 6.13: Effect of SR on the SFC, SP, relative NO_x emissions and recovered water mass flow rate of the SIR APPU, SR between 0.01 and 0.25

It can be seen that there is an optimal SR, for all aspects calculated. The SP and water flow are maximised and the SFC and relative NO_x are minimised when the SR is approximately 0.13. The fact there is an optimum can be explained. When the SR is low (SR<0.13) the flow is cooled to very low temperatures (the lower limit is set to 200 K), as there is relatively (too) much LH_2 for the gas flow. It results in not all heat sink potential being used as the result of the lower temperature limit enforcement, effectively limiting the HE effectiveness of the condenser. In these conditions, practically all water is condensed and collected. This is proven by the linearity of the graphs up to SR=0.12. Twice as much mass flow means twice as much water vapour to be condensed and collected (assuming equal flow compositions). Then, when SR≈0.13, all heat sink potential of the fuel is utilised, and an optimal temperature is reached for water condensation. As shown in Figure 4.3, the flow needs to be cooled exponentially further to extract the last bits of water.

Next, if the SR is increased further, the amount of water collected decreases, despite there being more water vapour present in the flow. This is because the LH_2 fuel is no longer able to cool the flow down to the mentioned optimal temperature for water condensation. The flow leaves the HE at a higher temperature, containing significant amounts of gaseous water still, which can not be collected.

Finally, when SR>0.20, the LH_2 fuel is no longer able to cool the flow down to the temperature at which the first condensation would occur. This means no water is condensed and thus collected, resulting in no NO_x reduction and an increase in SFC. This increase in SFC is due to the pressure losses in the HEs, which a significant part of the total flow now passes through. This is also proven by the fact that the engine performance deteriorates further when SR is increased beyond 0.20.

Heat exchanger effectiveness

The following SIR cycle-specific parameter is the heat exchanger effectiveness. This parameter can significantly impact the water cycle, making it interesting to perform a sensitivity analysis about it. The HE effectiveness is varied between 0.5 and 1.0, with a SR of 0.13. The results are shown in Figure 6.14.

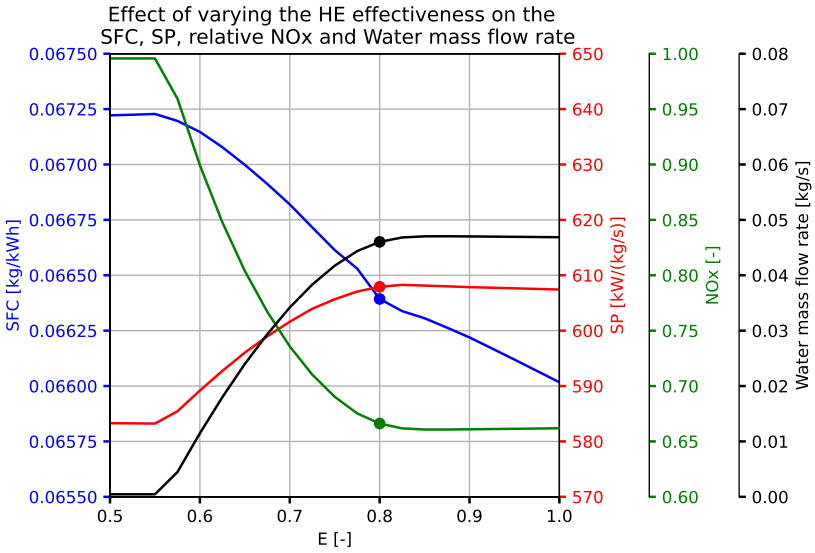

Figure 6.14: Effect of heat exchanger effectiveness on the SFC, SP, relative NO_x emissions and recovered water mass flow rate of the SIR APPU, ϵ between 0.5 and 1.0

The results can be explained in a similar manner as the SR sensitivity results in Section 6.3.2. When ϵ is low (ϵ<0.575) no water is collected, as there is not sufficient heat transfer to cool the flow to a temperature where condensation could occur.

Next, with increasing HE effectiveness, the amount of water collected increases. This is made possible by the larger heat flux cooling the flow to a lower temperature. Here a sort of snowball effect is created: a higher ϵ means more cooling in the condenser, which results in more water extracted. More water extracted also means more water flowing through the water side of the HRSG, causing more heat from the gas flow to pass to the water flow. The condenser then receives gas of a lower temperature already, meaning it can reach an even lower temperature itself, resulting in more water extracted, and so on. However, this snowball effect does hit a ceiling when $\epsilon \approx$0.825. At this point, all water in the flow is being condensed and extracted, meaning that even with more heat flux, the water massflow rate can not be increased.

But, it can be seen that even when the water mass flow rate does not increase at ϵ beyond 0.85, the SFC still decreases. This is due to the HRSG. With a larger ϵ, more heat is transferred from the gas to the water, meaning water with a higher enthalpy is injected into the combustor. The result is that less fuel is required to heat up and evaporate the injected water, hence an improved SFC.

Heat exchanger pressure losses

Section 4.4.2 describes what causes pressure loss in heat exchangers, and what design parameters influence this. It also states the large uncertainty in finding an appropriate value, and how ϵ has a significant impact. A designer might have to make the trade-off between choosing a higher ϵ at the cost of a larger pressure loss. In the section above, the impact of ϵ is calculated, and here, the effect of pressure loss is investigated.

To simplify the analysis, both heat exchangers, the HRSG and the condenser, have equal pressure losses. The chosen range is between perfect HEs and double the used pressure loss, i.e. between 0% and 10% for each HE. The results are shown in Figure 6.15. This analysis displays some limited numerical instability. Nevertheless, trends can be observed. The observed trends are similar to those seen in Figure 6.8: the pressure loss has a detrimental effect on engine performance, albeit to a limited extent. The performance difference in performance between 0% and 10% pressure loss in the HEs is smaller than what is observed for the combustor, despite the pressure loss being applied twice over. However, this is logical since only a small part of the total mass flow experiences the HE dP, whereas almost the complete flow experiences the dP of the combustor. The amount of water recovered and thus relative NO_x emissions are practically unaffected.

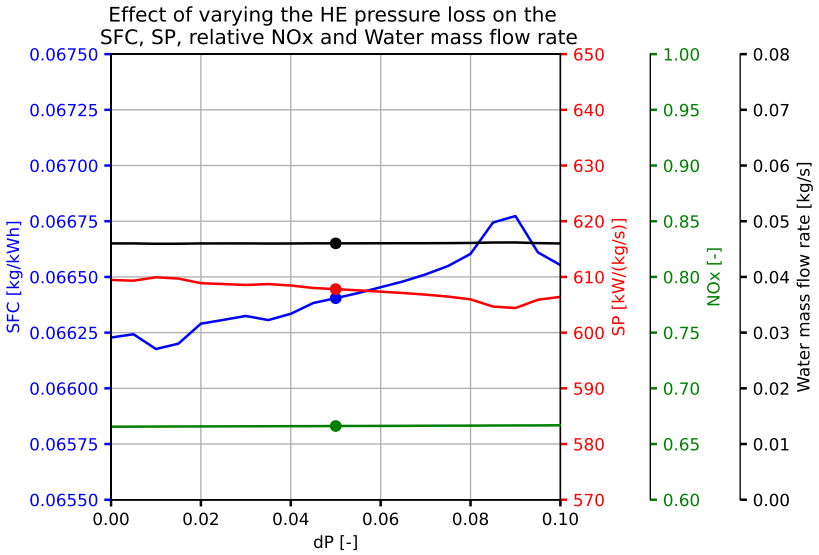

Figure 6.15: Effect of HE pressure loss on the SFC, SP, relative NO_x emissions and recovered water mass flow rate of the SIR APPU, dP between 0.0 and 0.1

Additional water inserted

The last sensitivity analysis for the SIR APPU concerns adding extra water from a storage tank to the water cycle. Table 6.9 shows that 46.0 g/s of water reduces the NO_x emissions with 33.4%. What if that reduction in NO_x can be significantly expanded by adding small amounts of water? Or how much water needs to be added if the NO_x emissions regulations require an even larger reduction in NO_x emissions? This sensitivity analysis aims to find that out and see how much added water results in how much further NO_x emissions reduction.

Another effect that will be investigated is the two snowball effects that are induced by adding water. The first is similar to the one explained in the ϵ sensitivity analysis: a larger water mass flow rate can result in a larger heat flux out of the gas path in the HRSG, giving the condenser a cooler flow which then can reach a lower temperature and extract more liquid water. The second is that if more water is present in the gas path, more water could potentially be extracted.

The drawback of adding water is that this water has to be supplied from a storage tank. This would add significant mass to the airplane. For example, if 10 g/s is added, this would add up to 108 kg of water for a 3-hour cruise phase. How much this would impact the complete aircraft is outside the scope of this project, but it might be interesting for an aircraft designer to know the outcome of this analysis such that a trade-off could be made. Up to 40 g/s is added, and the results are shown in Figure 6.16.

It can be seen that, as expected, the NO_x emissions are further reduced by adding water. Adding an (almost) equal amount of water as was extracted initially does not reduce the NO_x emission by an equal amount, however. This is expected because Equation 4.7 is not a linear relation. The snowball effects are limited. Adding 40 g/s only increases the captured water mass flow rate from 46.0 g/s to 49.8 g/s, an increase of 3.8 g/s or 8.2%.

Similar to the SFC trend in Figure 6.14, more circulating water decreases the SFC. This is also shown in this analysis. This trend does reverse, however, when 29 g/s or more is added. This is because from that rate of water added and upwards, the 'limiting side' of the HRSG is switched: In all other conditions the water side has the smallest heat transfer capacity ($MIN(Q_h, Q_c)$, Equation 4.5), but increasing the water mass flow rate increases the heat transfer capacity of the cold side. Once this happens, the water flow injected into the combustor has a lower enthalpy, thus requiring more fuel to be evaporated and heated up. This, in turn, increases the SFC.

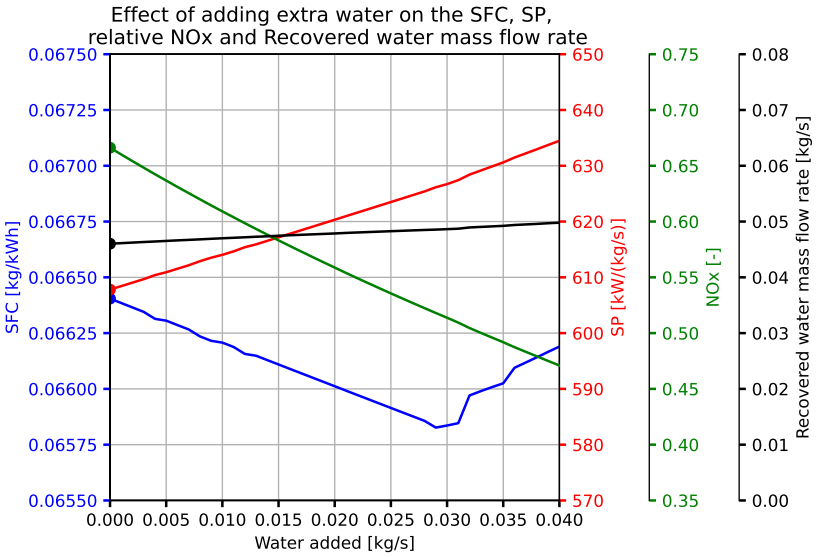

Figure 6.16: Effect of inserting additional water into the cycle on the SFC, SP, relative NO_x emissions and recovered water mass flow rate of the SIR APPU, $W_{addedwater}$ between 0.00 kg/s and 0.04 kg/s

7

Discussion

The results reported in Chapter 6 need to be critically analysed, such as explaining unexpected results and discussing found sources of inaccuracies. This will increase confidence in the answer to the research question. This chapter starts by explaining the discrepancy between the hydrogen and kerosene operation in Section 7.1. After that, the impact of fuel temperature negligence is investigated in Section 7.2. Lastly, Section 7.3 lists additional recognised sources of inaccuracies.

7.1. Hydrogen-kerosene discrepancy

Both the baseline APPU and the SIR APPU show that during kerosene operation significantly less power can be produced. Understanding the cause of this discrepancy is essential, as it hinders the engine from meeting its requirements. If the problem is understood, it might be possible to propose mitigation strategies. This section aims to find an explanation for the discrepancy and, if possible, will give solutions.

The baseline core produces 264 kW less (12.0%), and the SIR core produces 443 kW less (20.1%) when comparing the hydrogen and kerosene cruise condition results. This is due to the different specific heats of the combustion products, which leads to a different specific enthalpy and, thus, a different amount of energy to be extracted by the turbines. When burning one kilogram of kerosene (*pyCycle*'s $Jet - A(g)$ is $C_{12}H_{23}$), 3.16 kg of CO_2 and 1.24 kg of H_2O are created, while burning one kilogram of hydrogen creates 8.94 kg of H_2O. Even when normalising for the Lower Heating Values (LHV)(43.03 MJ/kg for kerosene [46] and 120.0 MJ/kg for H_2), H_2 combustion creates 2.59 times as much H_2O. Water has a higher C_P than air and than CO_2, meaning a higher concentration of water results in a higher C_P.

This is also calculated by *pyCycle*. Two separate engines are 'designed', with equal inputs apart from the design fuel. When comparing the C_P at the combustor exit, C_P=1.425 kJ/kg K and C_P=1.330 kJ/kg K are calculated for the H_2 and kerosene engines respectively. This location is chosen for comparison because here both temperature and pressure are equal for both engines. For these two engines, the total temperature (and pressure) entering the combustor are equal (assuming equal compressor efficiencies), meaning an equal ΔT to be achieved. Due to the lower C_P of the kerosene combustion products, less energy is added. The specific thermal power added in the combustor is 1.39 MW/(kg/s) for the hydrogen engine and 1.26 MW/(kg/s) for the kerosene engine, a difference of 10.0%. Less power added also means less power can be extracted.

This is because the flow can only be reduced in pressure so far. Both engines have an equal OPR, and thus an equal pressure ratio to distribute over the three turbine sections. The PR is directly linked to the temperature ratio. This shows that, apart from a negligible difference in γ and when ignoring cooling air, the exhaust temperature will be equal. With the lower C_P, this means less energy is extracted in the turbines, and thus less work is produced.

Again, this is as calculated by *pyCycle*. The exhaust conditions are nearly identical: equal total pressure (due to the nozzle PR input), and a total temperature of 897 K and 902 K for the H_2 and kerosene engine respectively. With the lower specific thermal power, this means that less power is available.

This explains the majority of the difference, but not all of it. Stepping away from the two different engines and back to the original case of the APPU engine, the remainder of the difference can be admitted/allocated/assigned to the component maps. It can be seen in Figure A.7 that the higher W_c

results in a lower LPC speed which, in turn, reduces the mass flow. Add the lower SP and lower mass flow together, and one gets the 12.0% power reduction.

This argument about the different C_P due to different combustion products is further supported by the larger power decrease for the SIR APPU. There, the water concentration is lower, both due to the different fuel and due to the lack of steam added. Even comparing the design condition and H_2 cruise without HEs gives a 210.5 kW (9.6%) power decrease.

A similar discrepancy was found by Mourouzidis et al. [73]. They ran analyses on two different but similar turbofan engines: one designed for kerosene and one for hydrogen. Rather than keeping the TET equal, they opted to keep the thrust the same. The result is two almost identical engines, but with 78 K lower TET for the hydrogen engine. A sensitivity showing the required TET for a range of thrust outputs was made, which is shown in Figure 7.1. This graph allows to compare the thrust output at equal TET for the kerosene and hydrogen engines. For example, at TET=1600 K, the thrust of the kerosene engine is 14.6% lower than that of the hydrogen engine. They attributed this to a difference in specific heat as well.

Comparable to their strategy, the TET in the APPU can be increased during kerosene operation in order to get equal power output. This is already implemented in the APU-modi: the TETs are 900 K and 920 K for the hydrogen and kerosene APU-modi, respectively. In kerosene cruise, the TET can be increased from 1700 K to 1790 K, resulting in a power output of 2211 kW with an OPR of 26.45 and $\eta_{thermal}$ of 45.1%. This will, however, increase the NO_x emissions. On the other side of the spectrum, one can also opt to lower the design condition (hydrogen cruise) TET. If the hydrogen cruise TET is reduced from 1700 K to 1625 K, the SP is lowered by 9.6%. With the kerosene cruise TET still at 1700 K, it can produce 2204 kW. This method will reduce the NO_x emissions in hydrogen cruise, but also decrease the SP and thus increase the engine size.

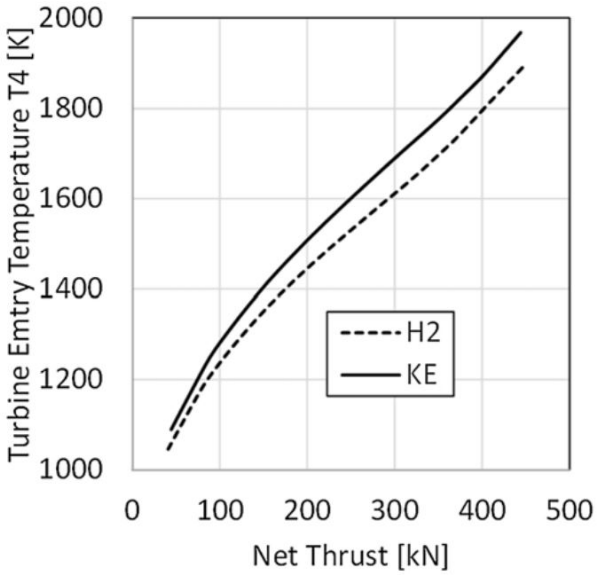

Figure 7.1: Comparison of standard day T4 vs Thrust for the baseline (KE) and hydrogen (H2) turbofans [73]

It is found that the power discrepancy between hydrogen and kerosene operation is caused by a difference in C_P of the combustion products. To equalise the power output, one could increase the kerosene TET, or decrease the hydrogen TET. The former has the drawback of higher NO_x emissions, while the latter strategy increases the engine mass.

7.2. Fuel temperature

pyCycle's standard combustor is made in such a way that the fuel temperature is not incorporated in the thermodynamic calculations. When fuel is added, the total enthalpy of the flow remains constant (and thus, the specific enthalpy drops slightly due to the new larger mass flow). The temperature at the end of the combustor can still be higher, because the zero-enthalpy-temperature of the combustion products lies at a different temperature than those of the gasses in the air.

One might think that then the fuel temperature is taken into account by this discrepancy in zero-enthalpy temperature as well, but this is not the case. Regardless of the combustor inlet temperature, the fuel enthalpy is zero. However, heating up the fuel from a lower temperature to the combustor inlet temperature can require a significant amount of energy. In the case of the APPU, the HPC discharge temperature is approximately 700 K in cruise. If the kerosene fuel is injected at 298 K (and 1 atm), 861 kJ/kg is required to heat it to 700 K [74], or 2.0% of the LHV.

This shows that in the case of a kerosene engine, neglecting the fuel temperature introduces only a small error. Additionally, when comparing different kerosene engines or design conditions, an approximately equal error is present in all analyses, thus cancelling out when comparing the results. This is also true when trying to compare hydrogen engines and design conditions. However, it becomes a problem when analyses involving different fuels are to be compared, or analyses of different cycles. Both apply to this research.

it is also the case for every APPU calculation performed, i.e. it is not a cause for differences between design conditions and the two cycles. However, it is important to consider the fuel temperature and enthalpy for the hydrogen analyses. Both because of a larger energy requirement and because of differences between the analysed cycles.

The comparison between fuels is corrupted because hydrogen (if stored cryogenically) requires significantly more energy to be heated to HPC discharge temperature. Heating hydrogen from 20 K to 700 K (at 1 atm), requires 9760 kJ/kg [62], or 8.1% of the LHV. This means that the calculated SFC of the conventional APPU should be 8.8% higher (neglecting other influences on the cycle due to higher fuel flow rate), whereas the kerosene operation SFC should only be 2.0% higher.

The comparison between the baseline and SIR cycle is corrupted due to the effect of the condenser on the fuel temperature. By cooling down the gas flow and condensing water, the condenser heats up the hydrogen. In the design condition, 7004 kJ/kg$_{H_2}$ of heat energy is transferred into the hydrogen, heating it up to 512 K. This means that 72% of the hydrogen heating towards HPC discharge temperature is done by the condenser. When translating this to the effects on the SFC, the penalty is reduced from 8.8% to 2.5%. This means that the design condition SFC improvement of the SIR cycle over the conventional cycle calculated in Table 6.9 of 1.54% is then increased to 7.28%.

This discussion highlights the importance of including the fuel temperature in the analysis, especially in the case of hydrogen (if it is stored cryogenically), as it can have a significant impact on the SFC. This is especially prevalent when comparing hydrogen operation with kerosene operation, and when comparing different cycles where only one incorporates a form of fuel pre-heating.

7.3. Sources of inaccuracies

Inherent to a numerical model are inaccuracies. They can, for example, arise from assumptions, an inability to model a particular aspect, or convergence errors. This section aims to create an overview of the recognised sources of inaccuracies in the study at hand, and, where possible, give an indication of the effect of the error. The fuel temperature omittance is an example of a source of inaccuracies, but due to its magnitude and significance, it is already discussed in Section 7.2. Also the uncertainty in the NO_x estimation method mentioned in Section 4.4.1 will not be discussed again, as well as discrepancies between *pyCycle* and *Gasturb* (Section 5.1).

Water cycle numerical integration

Already mentioned in Section 4.3.6, the forward-moving section of the water cycle, i.e. from the collector to the combustor, is running one iteration cycle behind the rest of the engine. Whether this increases or decreases output parameters will vary depending on the initial conditions and how the solver converges to a solution. However, the error is likely to be small: input tolerances for the solver are 10^{-6}. Unless the solver got lucky and suddenly found the solution after a large input step, the inputs when convergence is near are very similar to those of the previous iteration cycle.

Leakage

Jet engines cannot be made 100% airtight and thus experience leakage of high-pressure air. A small fraction is applied to the bleed component situated aft of the HPC, 0.5%. This value was left unchanged from the first APPU design iteration [19].

However, this leakage air is not rejoined with the gas path in the *pyCycle* model. In *Gasturb* this flow enters the gas path again aft of the PT. This is not the case in *pyCycle*, as bleed air can only re-enter the gas path in a turbine component. This might have a small impact on the engine operation, by means of influencing the exhaust flow. However, the effect is negligible: 0.5% of the inlet mass flow entering aft of the turbines, at an elevated temperature and pressure (HPC exit conditions), only has a negligible impact on the flow properties. The increased mass flow would slightly increase the engine thrust, but the thrust is of no importance in this research.

Constant cooling air
Using the methods described in Section 3.2.1, the amount of cooling air required for the turbines is calculated. However, this is only done for the design condition. These cooling air fractions stay constant for all other conditions. This is done to keep consistency between the cooling air fractions and the impact on efficiency. The design input efficiencies are calculated and applied with the cooling efficiency penalty included. *pyCycle* then scales the component maps with these efficiencies. This means that, regardless of any changes to cooling air fractions, the component efficiencies at all off-design conditions will be subject to the design condition cooling efficiency penalty.

The impact of this differs for each off-design condition. In take-off, the HPC exit temperature is higher, increasing the cooling air fractions. In APU-modus, the TET is below the AMOT, hence zero cooling air is required. In kerosene operation, the C_P of the combustion products is lower, which reduces the cooling air requirement. Additionally, the HPT PR is higher for the kerosene cases (see Figure A.5), reducing the LPT inlet temperature and thus the LPT cooling air requirement. These reasonings are summarized in Table 7.1, together with the expected impact on engine SFC and power output.

Table 7.1: Expected changes in cooling air fractions and engine SFC and power output due to inclusion of cooling air variability. The symbols ↑, ↓, - and 0 mean the parameter is expected to increase, decrease, be unaffected or be reduced to zero, respectively

Condition / Parameter	H_2 take-off	H_2 APU-modus	Kerosene cruise	Kerosene take-off	Kerosene APU-modus
HPT cooling fraction	↑	0	↓	↓	0
LPT cooling fraction	↑	0	↓	↓	0
PT cooling fraction	-	-	-	-	-
SFC	↑	↓	↓	↓	↓
Power	↓	↑	↑	↑	↑

Condensed water C_P
The inner workings of the condenser component are described in Section 4.3.3. There it is explained how the enthalpy bookkeeping when cooling down of the flow, including the water, is done using the built-in *pyCycle* (*CEA*) properties model. The latent heat is added separately to the bookkeeping. The liquified water introduces an error.

The method of the condenser calculates the heat flux required for cooling down the flow as if the water is gaseous at all times, despite any possible condensation. In the assumed reality, water gradually condenses as the temperature is lowered. Therefore, water is condensed and then cooled down further. Liquid water has a significantly different C_P than steam however, ∼4.2 kJ/kg K opposed to ∼2.0 kJ/kg K. This causes the temperature to be underestimated, as the C_P used is too low. Predicting the magnitude of the error is difficult, due to the non-linearity of the condensation process, and the inability to extract the C_P *pyCycle* calculates for water without causing instability.

The error is expected to be small, however, as the temperature decrease after the first condensation occurs, is only a fraction of the complete temperature decrease in the condenser: 40 K out of 370 K. Additionally, water is only part of the mass flow, about 10%. If all water would be condensed at the temperature condensation first starts, 10% of the mass flow would now have half the C_P it should have for 11% of the temperature range. This would mean an error of less than 2%, and this error becomes smaller when taking the gradual condensation into account.

8

Conclusion

With all results known, critically analysed and validated, conclusions can be drawn, and the research questions stated in Chapter 1 can be answered. First, the subquestions will be answered, after which the main question will get an answer.

- The first subquestion reads: *What is the performance of the baseline APPU, both in on- and off-design conditions?* The engine has a thermal efficiency of 44.5% in the design condition, and an approximate mass of 502 kg. The thermal efficiency of kerosene operation is similar, but power output is significantly reduced due to the difference in combustion products. While fulfilling the APU functionalities, the thermal efficiency drops to 17%, but such a drop is not unexpected at such a low power setting. More extensive results can be found in Table 6.5.

- The second subquestion reads: *How can an existing engine analysis tool be expanded such that the steam injection and recovery cycle can be modelled?* The chosen analysis tool is *pyCycle*. It requires the addition of a liquid-water thermodynamical properties model (the IAPWS IF-97 model), in combination with a realistic model to approximate the condensation process. It requires the addition of the HRSG and the condenser & collector components, and modification of the combustor such that it can accommodate injecting a mixture of water and steam. Lastly, it requires a water pump component to determine the power required for the water compression. A detailed explanation of the physics and implementation of these methods and components can be found in Section 4.3.

- Subquestion three is as follows: *What is the engine performance of the steam injection and recovery APPU engine, both in on- and off-design conditions?* The SIR APPU has a thermal efficiency of 45.2% in cruise when using hydrogen, and has an estimated total mass of 579 kg, of which 98 kg is attributed to the HRSG and condenser. The water injection decreases the NO_x emissions by 33.4%. However, performance significantly drops in off-design conditions, especially when the water cycle is unavailable. The complete set of results, including the off-design conditions, can be found in Table 6.8.

- The last subquestion is the following: *What is the sensitivity of the results to variation in input parameters such as OPR, TET, SR, E, etc.?* Varying the efficiencies, turbine material temperature and pressure losses have the expected effect: higher efficiencies and material temperatures, and lower pressure losses all have a favourable effect on the engine performance. The results from the OPR-TET sensitivities are in line with expectations as well: higher OPR improves SFC, and higher TET increases the SP. Taking the variability of component efficiencies into account in this analysis shows that a TET of approximately 1700 K is optimal with regards to SFC. A sweep of SR values shows an optimum exists, where water recovery is maximised and SFC is minimised, due to the interaction between hydrogen heat sink capacity and total water available in the bypass flow. This interaction is also visible when varying ϵ, but 0.8 is kept as the design value despite higher values being more favourable, as it is the realistic upper value for aero-engine applications. A full overview of the sensitivity analyses can be found in Section 6.3.

The answers to the subquestions lead to the answer to the main question, which reads:

What are the effects on engine SFC, NO_x emissions and engine mass of incorporating a steam injection and recovery cycle in the APPU engine?

Incorporation of the SIR cycle brings a minor improvement in engine SFC of 1.54%, but at the cost of a 15.7% engine weight penalty. The injection of steam into the combustion chamber lowers the NO_x emissions by 33.4%, a significant improvement, but this estimation carries a large uncertainty. The hydrogen take-off condition has similar performance improvements, but all other conditions suffer from the changed cycle and the resultant less optimal matching between turbines and compressors. This is most significantly reflected in a decreased power output. Additionally, the water cycle and its NO_x reductions are only possible during hydrogen operation.

9 Recommendations

This study calculates the SFC and mass of the baseline and SIR APPU and estimates a relative NO_x emissions reduction. This chapter lists recommendations for future work, aimed at improving the accuracy of the analyses and at further development of the (SIR) APPU project.

Fuel temperature inclusion: As discussed in Section 7.2, the fuel temperature is currently not included in *pyCycle*. Both in order to get a more realistic performance estimate of the conventional core APPU (and all other engines, for that matter) and to get a more realistic comparison between the two cycles, it is recommended that the fuel temperature is incorporated into *pyCycle*'s capabilities.

Further research into heat exchangers: In this research, the HEs are modelled as black boxes with some physical relations and assumptions governing their impact on the flow and engine cycle. The next step, both to get more accurate inputs for parametric analyses and to move towards the next design stage, could be to perform more detailed design and analysis studies of the HRSG and condenser.

Transient and part-power analyses: The present study focuses on the comparison between the two cycles, and therefore, only a limited number of flight conditions are modelled. To further assess the engine operation, part-power performance and transient behaviour need to be analysed. The former can be done in *pyCycle*, but the latter requires *Gasturb*. Part-power analyses should also involve expanding the number of flight conditions, to gain insight into, for example, the climb-phase or cruise at different altitudes. Results could be used for aircraft performance and fuel requirement analyses, as well as climate impact assessment.

Next steps in geometrical design: The current study predominantly involves parametric analyses, which do not require any specific geometry details. The core mass estimation in *Gasturb* requires some input, but still mostly relies on the default values and the built-in relations of *Gasturb*. To both further the design of the APPU and to improve the accuracy of the mass estimation, it is therefore recommended that a detailed geometry design study be conducted.

Aircraft implementation: Integration of the APPU in the *A321 APPU* aircraft has already been studied by Heidebrecht et al. [14]. However, this is for an old iteration of the conventional core APPU. The preliminary size estimation made using *Gasturb* (Figure 6.1) might be different in size and thus might require some additional work to place it in the A321 tail and design the inlet duct. Next to that, to better assess the feasibility of the SIR APPU, its impact on aircraft performance needs to be analysed. Additionally, once the HEs have been studied more and a preliminary size estimate is available, the physical integration into the airframe can be determined.

Cost analysis: The current study purely focuses on the thermodynamics of the SIR APPU. Cost factors are entirely ignored. Part of the feasibility assessment of the SIR APPU is its financial feasibility. Therefore, it is recommended to do a cost analysis of the SIR APPU.

Combustor design: After explaining the NO_x comparison method, Section 4.4.1 mentions the shortcomings of applying this method to this design study. Next to that, Section 3.2.2 mentions the uncertainty of the combustor pressure loss. Both these uncertainties originate from the lack of a determined combustor type, let alone a detailed combustor design. To solve these two uncertainties, it is therefore recommended that more details about the combustor be provided. Subsequently, a high-fidelity NO_x emissions assessment can be performed.

References

[1] M. Klöwer, M. R. Allen, D. S. Lee, S. R. Proud, L. Gallagher, and A. Skowron. “Quantifying aviation’s contribution to global warming”. In: *Environmental Research Letters* 16 (2021), p. 104027. DOI: 10.1088/1748-9326/ac286e.

[2] F. Yin and A. G. Rao. “A review of gas turbine engine with inter-stage turbine burner”. In: *Progress in Aerospace Sciences* 121 (2020), p. 100695. DOI: 10.1016/j.paerosci.2020.100695.

[3] F. Yin and A. G. Rao. “Performance analysis of an aero engine with inter-stage turbine burner”. In: *The Aeronautical Journal* 121 (2017), pp. 1605–1626. DOI: 10.1017/aer.2017.93.

[4] ACARE. “Flightpath 2050 Europe’s Vision for Aviation”. In: *European Commission* (2011). DOI: 10.2777/50266.

[5] C. A. Wells, P. D. Williams, N. K. Nichols, D. Kalise, and I. Poll. “Reducing transatlantic flight emissions by fuel-optimised routing”. In: *Environmental Research Letters* 16 (2021), p. 025002. DOI: 10.1088/1748-9326/abce82.

[6] S. van Dyk, J. Saddler, F. Boshell, D. Saygin, A. Salgado, and A. Seleem. *Biofuels for Aviation, Technology Brief*. Tech. rep. IRENA, 2017.

[7] D. L. Dagget, R. C. Hendricks, R. Walther, and E. Corporan. “Alternate Fuels for Use in Commercial Aircraft”. In: *Proceedings of 18th ISABE Conference, Beijing, China*. 2008. DOI: 10.1115/GT2019-91597.

[8] B. Khandelwal, A. Karakurt, P. R. Sekaran, V. Sethi, and R. Singh. “Hydrogen powered aircraft : The future of air transport”. In: *Progress in Aerospace Sciences* 60 (2013), pp. 45–59. DOI: 10.1016/j.paerosci.2012.12.002.

[9] M. Brown and R. Vos. “Conceptual design and evaluation of blended-wing-body aircraft”. In: *In AIAA Aerospace Sciences Meeting (210059 ed.). [AIAA 2018-0522] American Institute of Aeronautics and Astronautics Inc. (AIAA)*. 2018. DOI: 10.2514/6.2018-0522.

[10] J. Benad. “The Flying V - A new Aircraft Configuration for Commercial Passenger Transport”. In: *Deutsche Gesellschaft für Luft- und Raumfahrt*. 2015. DOI: 10.25967/370094.

[11] D. Kramer. “Hydrogen-powered aircraft may be getting a lift”. In: *Physics Today* 73 (12 2020), pp. 27–29. DOI: 10.1063/PT.3.4632.

[12] P. D. Bravo-Mosquera, F. M. Catalano, and D. W. Zingg. “Unconventional aircraft for civil aviation: A review of concepts and design methodologies”. In: *Progress in Aerospace Sciences* 131 (2022), p. 100813. DOI: 10.1016/j.paerosci.2022.100813.

[13] *Aircraft Technology Net Zero Roadmap*. Tech. rep. IATA, 2023.

[14] A. Heidebrecht, K. W. Burger, M. F. M. Hoogreef, R. Vos, A. T. Isikveren, and A Gangoli Rao. “Development of a Hydrogen-powered Fuselage-mounted BLI Propulsor Add-on for Passenger Aircraft”. In: *Paper presented at 33rd Congress of the International Council of the Aeronautical Sciences, Stockholm, Sweden*. 2022. URL: https://www.icas.org/ICAS_ARCHIVE/ICAS2022/data/papers/ICAS2022_0622_paper.pdf.

[15] TU Delft. *APPU project objectives*. 2023. URL: https://www.tudelft.nl/lr/appu/project/objectives.

[16] D. C. Acevedo, T. van Cranenburgh, J. Exalto, L. Halsema, B. van der Heijden, Y. Hoogterp, E. Jahilo, A. M. Jorge, Y. Naäman, M. J. M. van Schie, and M. van der Zwan. *Final Report A320 Auxiliary Propulsion and Power Unit*. Tech. rep. Delft, Netherlands: Delft University of Technology, 2020.

[17] O. Schmitz, H. Klingels, and P. Kufner. “Aero Engine Concepts Beyond 2030: Part 1 — The Steam Injecting and Recovering Aero Engine”. In: *Journal of Engineering for Gas Turbines and Power* 143 (2 2021), p. 021001. DOI: 10.1115/1.4048985.

[18] S. Kaiser, O. Schmitz, P. Ziegler, and H. Klingels. “The Water-Enhanced Turbofan as Enabler for Climate-Neutral Aviation”. In: *Applied Sciences* 12 (2022), p. 12431. DOI: 10.3390/app122312431.

[19] A. G. Rao and F. Yin. “The APPU Engine Preliminary Design July 2021”. Internal presentation, unpublished, July 2021.

[20] A. bariş. “Inlet Design for a Propulsive Fuselage Concept: Exploring and evaluating geometrical inlet features based on a numerical approach”. Master Thesis. MA thesis. Delft University of Technology, 2024.

[21] Y. S. Chati and H. Balakrishnan. “Analysis of Aircraft Fuel Burn and Emissions in the Landing and Take Off Cycle using Operational Data”. In: *Proceedings of the 6th International Conference on Research in Air Transportation, Istanbul, Turkey*. 2014.

[22] Jack D. Mattingly, William H. Heiser, Keith M. Boyer, Brenda A. Haven, and David T. Pratt. *Aircraft Engine Design*. 3rd ed. American Institute of Aeronautics and Astronautics, Inc., 2018. DOI: 10.2514/4.105173.

[23] L. H. Smith. “Wake Ingestion Propulsion Benefit”. In: *Journal of Propulsion and Power* 9 (1 1993), pp. 74–82. DOI: 10.2514/3.11487.

[24] A. Uranga, M. Drela, David K. Hall, and Edward M. Greitzer. “Analysis of the Aerodynamic Benefit from Boundary Layer Ingestion for Transport Aircraft”. In: *American Institute of Aeronautics and Astronautics Journal* 56 (11 2018). DOI: 10.2514/1.J056781.

[25] Nicolas G.M. Moirou, Drewan S. Sanders, and Panagiotis Laskaridis. “Advancements and prospects of boundary layer ingestion propulsion concepts”. In: *Progress in Aerospace Sciences* 138 (2023), p. 100897. DOI: 10.1016/j.paerosci.2023.100897.

[26] A. F. El-Sayed. *Fundamentals of Aircraft and Rocket Propulsion*. 1st ed. Springer, 2016. DOI: 10.1007/978-1-4471-6796-9.

[27] J. P. van Buijtenen and et al. *AE4238: Aero Engine Technology*. 4th ed. Course reader. Delft, 2018.

[28] H. I. H. Saravanamuttoo, H. Cohen, and G. F. C. Rogers. *Gas Turbine Theory*. 5th ed. Pearson, 2001.

[29] M. Eqbal, N. Fernando, M. Marino, and G. Wild. “Development of a Turbo Electric Distribution System for Remotely Piloted Aircraft Systems”. In: *Journal of Aerospace Technology and Management* 13 (2021). DOI: https://doi.org/10.1590/jatm.v13.1209.

[30] P. Breeze. *Gas-Turbine Power Generation*. 1st ed. Elsevier, 2016. DOI: https://doi.org/10.1016/C2014-0-04848-4.

[31] J. H. R. Sadler and G. S. Hodges. “Turboprop and Open Rotor Propulsion for the Future”. In: *Proceedings of the AIAA/ASME/SAE/ASEE 22nd Joint Propulsion Conference, Huntsville, USA*. 1986.

[32] E. Hosking, D. P. Kenny, R. I. McCormick S. H. Moustapha, P. Sampath, and A. A. Smailys. “The PW100 Engine: 20 Years of Gas Turbine Technology Evolution”. In: *In Design Principles and Methods for Aircraft Gas Turbine Engines, proceedings of the RTO Applied Vehicle Technology Panel (AVT) Symposium, Toulouse, France*. 1998.

[33] M. P. Boyce. *Gas Turbine Engineering Handbook*. 4th ed. Elsevier, 2011. DOI: 10.1016/C2009-0-64242-2.

[34] P. P. Walsh and P. Fletcher. *Gas Turbine Performance*. 2nd ed. Blackwell Science Ltd., 2004. DOI: 10.1002/9780470774533.

[35] G. E. Welch, M. D. Hathaway, Gary J. Skoch, and C. A. Snyder. “Rotary-Wing Relevant Compressor Aero Research and Technology Development Activities at Glenn Research Center”. In: *Proceedings*

of the 65th Annual Forum and Technology Display, Grapevine, USA. NASA report No. TM—2012-217280. 2012.

[36] A. H. Lefebvre and D. R. Ballal. *Gas Turbine Combustion: Alternative Fuels and Emissions*. 3rd ed. Taylor&Francis, 2010.

[37] E. S. Hendricks and J. S. Gray. "pyCycle: A Tool for Efficient Optimization of Gas Turbine Engine Cycles". In: *Aerospace* 6 (8 2019), p. 87. DOI: 10.3390/aerospace6080087.

[38] J. S. Gray, J. T. Hwang, J. R. R. A. Martins, K. T. Moore, and B. A. Naylor. "OpenMDAO: an open-source framework for multidisciplinary design, analysis, and optimization". In: *Structural and Multidisciplinary Optimization* 59 (2019), pp. 1075–1104. DOI: 10.1007/s00158-019-02211-z.

[39] K. A. Geiselhart, L. P. Ozoroski, J. W. Fenbert, E. W. Shields, and W. Li. "Integration of Multifidelity Multidisciplinary Computer Codes for Design and Analysis of Supersonic Aircraft". In: *Proceedings of the 49th AIAA Aerospace Sciences Meeting including the New Horizons Forum and Aerospace Exposition, Orlando, USA*. 2011. DOI: 10.2514/6.2011-465.

[40] D. L. Allison, C. C. Morris, J. A. Schetz, R. K. Kapania, C. Sultan, L. T. Watson, J. D. Deaton, and R. V. Grandhi. "A Multidisciplinary Design Optimization Frameworkfor Design Studies of an Efficient Supersonic AirVehicle". In: *Proceedings of the 12th AIAA Aviation Technology, Integration, and Operations (ATIO) Conference and 14th AIAA/ISSM, Indianapolis, USA*. 2012. DOI: 10.2514/6.2012-5492.

[41] D. L. Allison, E. J. Alyanak, and N. D. Bhagat. "High Fidelity, Nonlinear, Integrated Nozzle Installation Effects for Numerical Propulsion System Simulation". In: *Proceedings of the 56th AIAA/ASCE/AHS/ASC Structures, Structural Dynamics, and Materials Conference, Kissimmee, USA*. 2015. DOI: 10.2514/6.2015-0649.

[42] R. W. Claus, A. L. Evans, J. K. Lylte, and L. D. Nichols. "Numerical Propulsion System Simulation". In: *Computing Systems in Engineering* 2 (4 1991), pp. 357–364. DOI: 10.1016/0956-0521(91)90003-N.

[43] J. K. Lytle. "The Numerical Propulsion System Simulation: A Multidisciplinary Design System for Aerospace Vehicles". In: *Proceedings of the 14th International Symposium on Air Breathing Engines, Florance, Italy*. 1999.

[44] J. S. Gray, K. T. Moore, and B. A. Naylor. "OpenMDAO: An Open Source Framework for Multidisciplinary Analysis and Optimization". In: *Proceedings of the 13th AIAA/ISSMO Multidisciplinary Analysis Optimization Conference, Fort Worth, USA*. 2010. DOI: 10.2514/6.2010-9101.

[45] S. Gordon and B. J. McBride. *Computer Program for Calculation of Complex Chemical Equilibrium Compositions and Applications – I. Analysis*. Tech. rep. NASA report No. 1311. NASA, 1994.

[46] B. J. McBride and S. Gordon. *Computer Program for Calculation of Complex Chemical Equilibrium Compositions and Applications – II. Users Manual and Program Description*. Tech. rep. NASA report No. 1311. NASA, 1996.

[47] J. Gray, J. Chin, T. Hearn, E. Hendricks, Thomas Lavelle, and J. R. R. A. Martins. "Chemical-Equilibrium Analysis with Adjoint Derivatives for Propulsion Cycle Analysis". In: *Journal of Propulsion and Power* 33 (5 2017), pp. 1041–1052. DOI: 10.2514/1.B36215.

[48] J. Kurzke. "Gas Turbine Cycle Design Methodology: A Comparison of Parameter Variation With Numerical Optimization". In: *Journal of Engineering for Gas Turbines and Power* 121 (1 1999), pp. 6–11. DOI: 10.1115/1.2816315.

[49] *Gasturb 12*. GasTurb GmbH. 2018. URL: https://www.gasturb.com/Downloads/Manuals/GasTurb12.pdf.

[50] H. Wemming. *Validation and integration of a rubber engine model into an MDO environment*. Master Thesis. 2010.

[51] J. W. Chapman, T. M. Lavelle, R. May, J. S. Litt, and T. Guo. "Propulsion System Simulation Using the Toolbox for the Modeling and Analysis of Thermodynamic Systems (T MATS)". In: *Proceedings of the 50th AIAA/ASME/SAE/ASEE Joint Propulsion Conference, Cleveland, USA*. 2014.

[52] C. A. Snyder and M. T. Tong. “Modeling Turboshaft Engines for the Revolutionary Vertical Lift Technology Project”. In: *Proceedings of the Vertical Flight Society’s 75th Annual Forum Technology Display, Philadelphia, USA*. 2019.

[53] M. Jonsson, O. Bolland, D. Bücker, and M. Rost. “Gas Turbine Cooling Model for Evaluation of Novel Cycles”. In: *Proceedings of the International ECOS Conference, Trondheim, Norway*. 2005, pp. 641–650.

[54] F. Yin, F. S. Tiemstra, and A. G. Rao. “Development of a Flexible Turbine Cooling Prediction Tool for Preliminary Design of Gas Turbines”. In: *Journal of Engineering for Gas Turbines and Power* 140 (9 2018), pp. 091201-1 - 091201–12. DOI: 10.1115/1.4039732.

[55] M.L. Grilli, D. Valerini, A.E. Slobozeanu, B.O. Postolnyi, S. Balos, A. Rizzo, and R.R. Piticescu. “Critical Raw Materials Saving by Protective Coatings under Extreme Conditions: A Review of Last Trends in Alloys and Coatings for Aerospace Engine Applications”. In: *Materials* 14 (7 2021), p. 1656. DOI: 10.3390/ma14071656.

[56] R. M. Plencner. *Plotting Component Maps in the Navy/NASA Engine Program (NNEP)– A Method and Its Usage*. Tech. rep. NASA report No. TM-101433. NASA, 1989.

[57] Y. Liu, X. Sun, V. Sethi, D. Nalianda, Y. Li, and L. Wang. “Review of modern low emissions combustion technologies for aero gas turbine engines”. In: *Progress in Aerospace Sciences* 94 (2017), pp. 12–45. DOI: 10.1016/j.paerosci.2017.08.001.

[58] O. Schmitz et al. “Aero Engine Concepts Beyond 2030: Part 3 — Experimental Demonstration of Technological Feasibility”. In: *Journal of Engineering for Gas Turbines and Power* 143 (2 2021), p. 021003. DOI: 10.1115/1.4048994.

[59] A. Chen, D. Maloney, and W. Day. “Humid Air NOx Reduction Effect on Liquid Fuel Combustion”. In: *Journal of Engineering for Gas Turbines and Power* 126 (1 2004), pp. 69–74. DOI: 10.1115/1.1615255.

[60] J. R. Cooper and R. B. Dooley. *Revised Release on the IAPWS Industrial Formulation 1997 for the Thermodynamic Properties of Water and Steam*. Tech. rep. The International Association for the Properties of Water and Steam, 2007.

[61] D. Sonntag. “Advancements in the field of hygrometry”. In: *Meteorologische Zeitschrift* 3 (2 1994), pp. 51–66. DOI: 10.1127/metz/3/1994/51.

[62] R.D. McCarty, J. Hord, and H.M. Order. *Selected properties of hydrogen (engineering handbook)*. National Bureau of Standards, 1981.

[63] M. W. Chase. *NIST-JANAF Thermodynamical Tables Fourth Edition*. American Institute of Physics, 1998.

[64] R. Xue, C. Hu, T. Nikolaidis, and P. Pilidis. “Effect of steam addition on the flow field and NOx emissions for Jet-A in an aircraft combustor”. In: *International Journal of Turbo and Jet-Engines* 33 (4 2015), pp. 381–393. DOI: 10.1515/tjj-2015-0041.

[65] K. G. Kyprianidis, D. Nalianda, and E. Dahlquist. “A NOx Emissions Correlation for Modern RQL Combustors”. In: *Proceedings of the The 7th International Conference on Applied Energy – ICAE2015*. 2015.

[66] H. H. W. Funke, N. Beckmann, and S. Abanteriba. “An overview on dry low NOx micromix combustor development for hydrogen-rich gas turbine applications”. In: *International Journal of Hydrogen Energy* 44 (2019), pp. 6978–6990. DOI: 10.1016/j.ijhydene.2019.01.161.

[67] C. F. McDonald and R. A. Langworthy. “Advanced regenerative gas turbine for lightweight and high performance”. In: ASME Paper 71-GT-67. 1971.

[68] C. F. McDonald, A. F. Massardo, C. Rodgers, and A. Stone. “Recuperated gas turbine aero-engines, part II: engine design studies following early development testing”. In: *Aircraft Engineering and Aerospace Technology: An International Journal* 80 (3 2008), pp. 280–294. DOI: 10.1108/00022660810873719.

[69] R. Andriani, U. Ghezzi, A. Ingenito, and F. Gamma. “Fuel Consumption Reduction and Weight Estimate of an Intercooled-Recuperated Turboprop Engine”. In: *International Journal of Turbo and Jet Engines* 29 (3 2012), pp. 165–177. DOI: 10.1515/tjj-2012-0025.

[70] C. F. McDonald and C. Rodgers. “Heat Exchanged Propulsion Gas Turbines: A Candidate for Future Lower SFC and Reduced Emission Military and Civil Aeroengines”. In: *Proceedings of the ASME Turbo Expo 2009: Power for Land, Sea and Air GT2009, Orlando, USA*. 2009.

[71] National Research Council. *Improving the Efficiency of Engines for Large Nonfighter Aircraft*. The National Academies Press, 2007. DOI: 10.17226/11837.

[72] S. Kaiser, A. Seitz, S. Donnerhack, and A. Lundbladh. “A Composite Cycle Engine Concept with Hecto-Pressure Ratio”. In: *In Proceedings of the 51st AIAA/SAE/ASEE Joint Propulsion Conference, Propulsion and Energy Forum, Orlando, USA*. 2015.

[73] C. Mourouzidis, G. Singh, X. Sun, J. Huete, D. Nalianda, T. Nikolaidis, V. Sethi, A. Rolt, E. Goodger, and P. Pilidis. “Abating CO2 and non-CO2 emissions with hydrogen propulsion”. In: *The Aeronautical Journal* (2024), pp. 1–18. DOI: 10.1017/aer.2024.20.

[74] R. Xu, H. Wang, M. Colket, and T. Edwards. *Thermochemical Properties of Jet Fuels*. Tech. rep. Stanford University, 2015.

A

Component maps

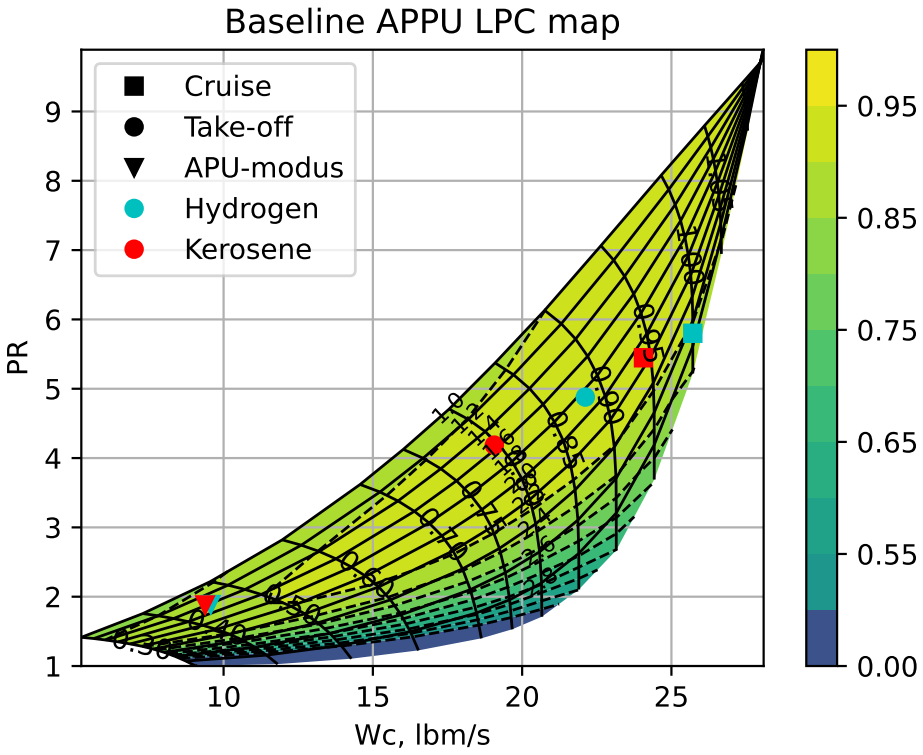

Figure A.1: Baseline APPU LPC map

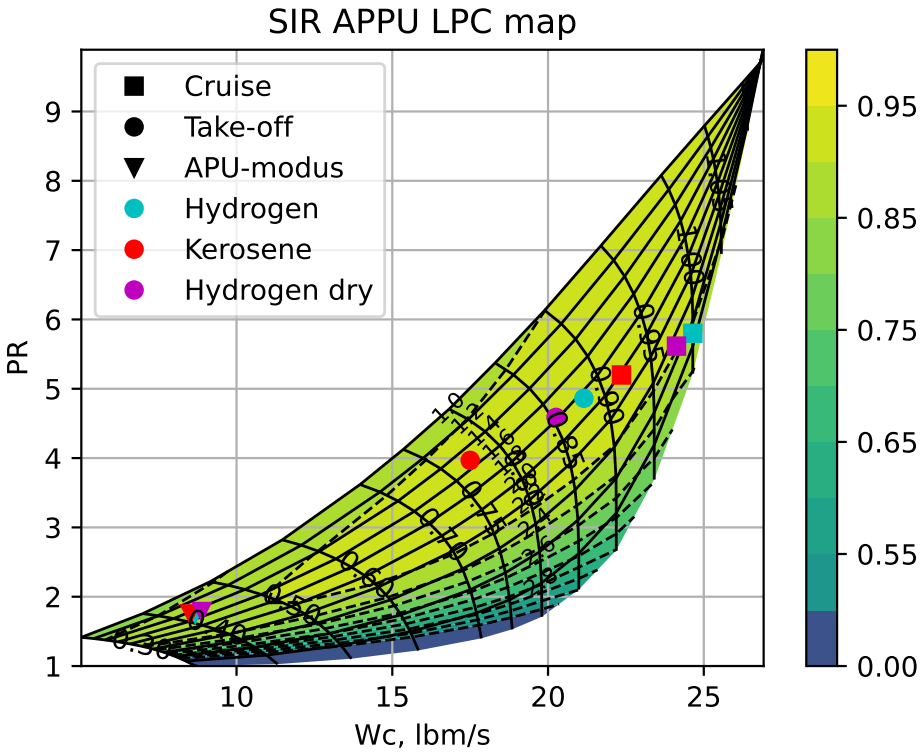

Figure A.2: SIR APPU LPC map

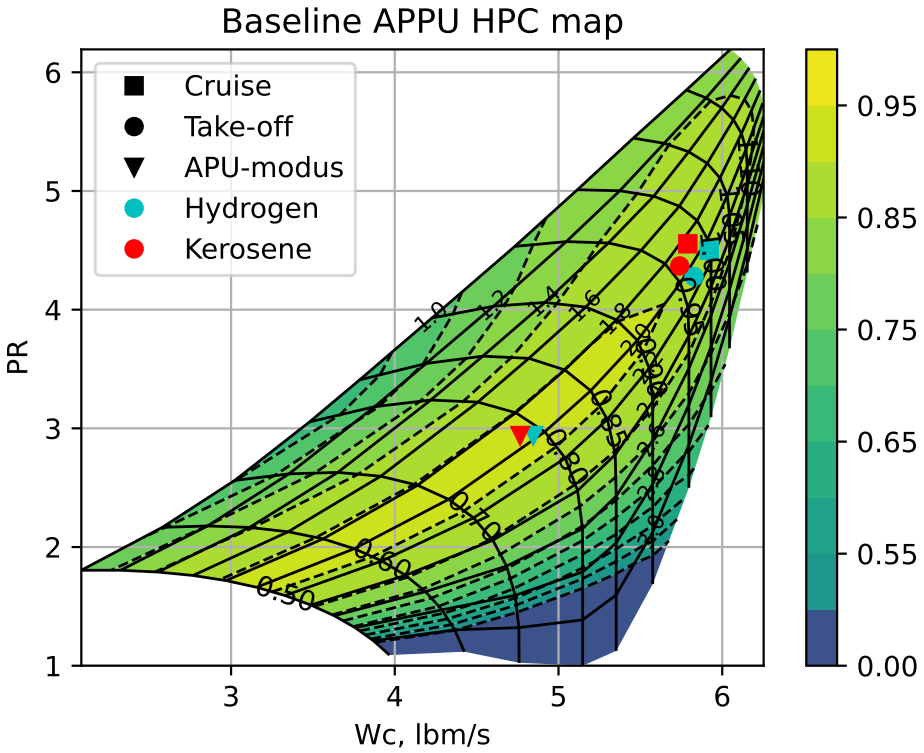

Figure A.3: Baseline APPU HPC map

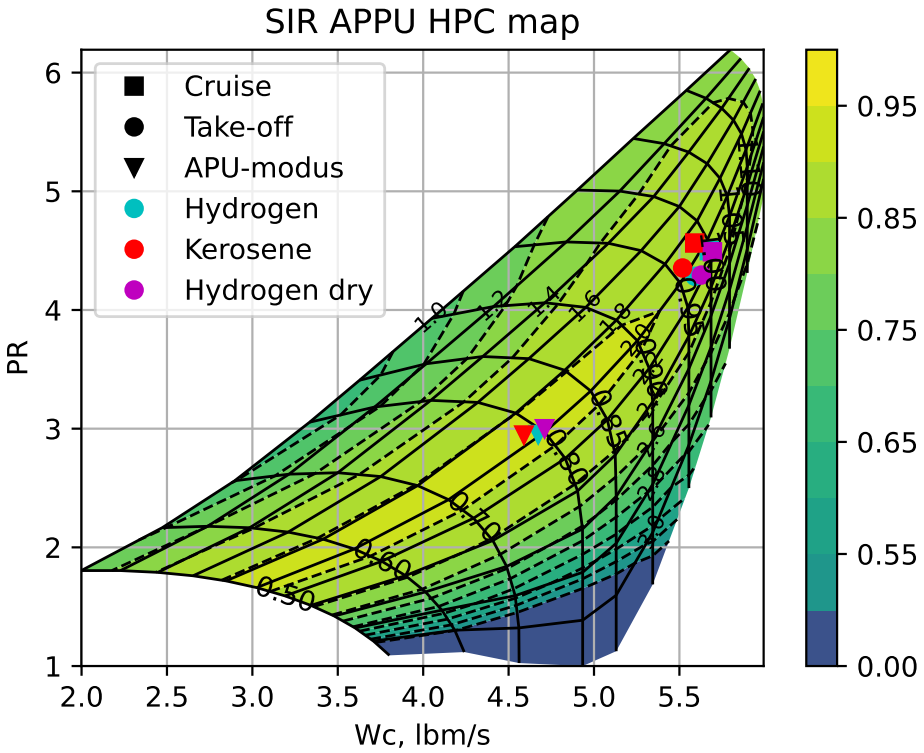

Figure A.4: SIR APPU HPC map

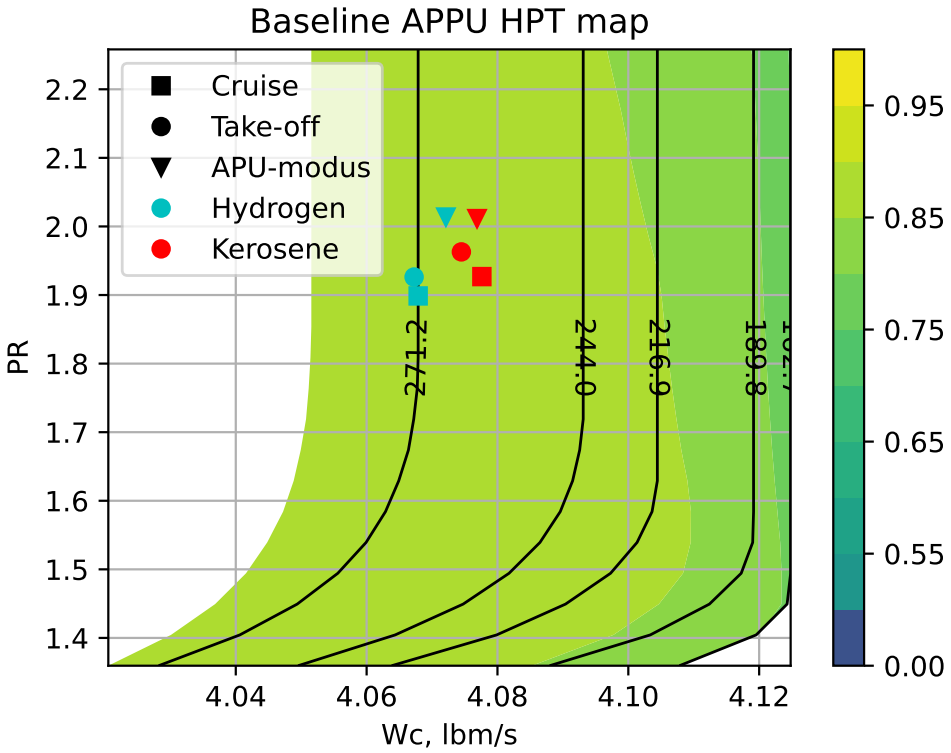

Figure A.5: Baseline APPU HPT map

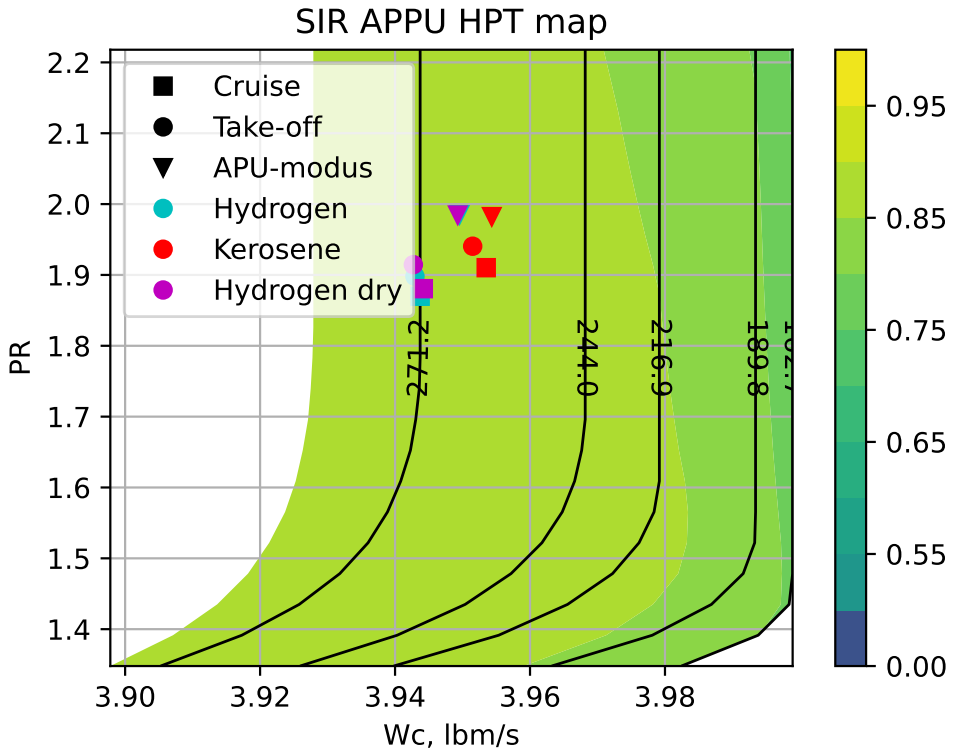

Figure A.6: SIR APPU HPT map

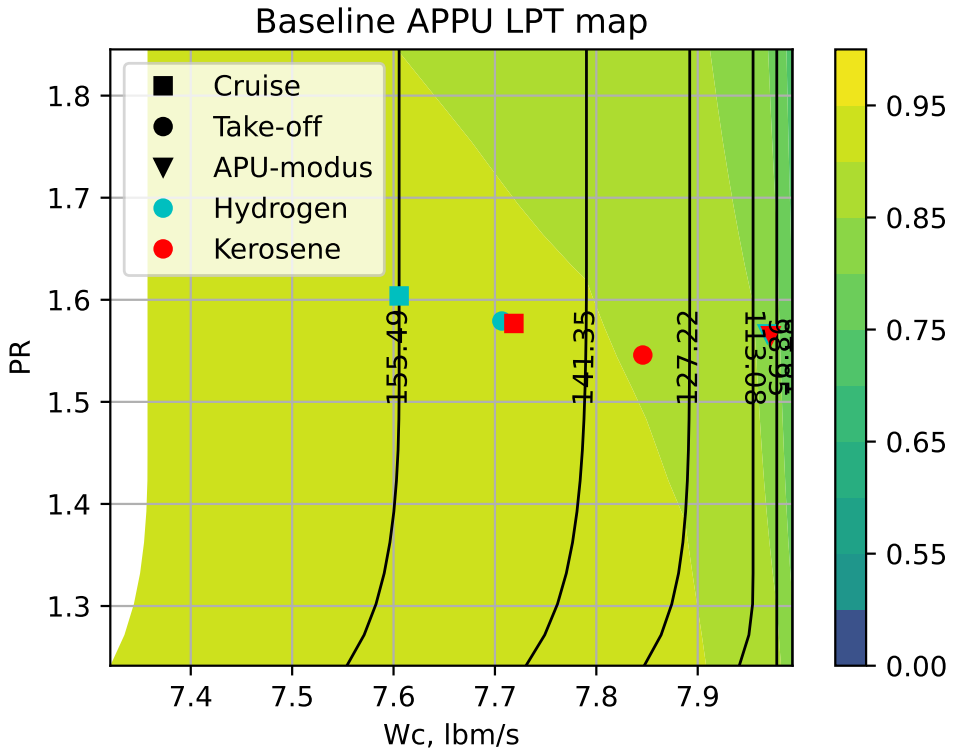

Figure A.7: Baseline APPU LPT map

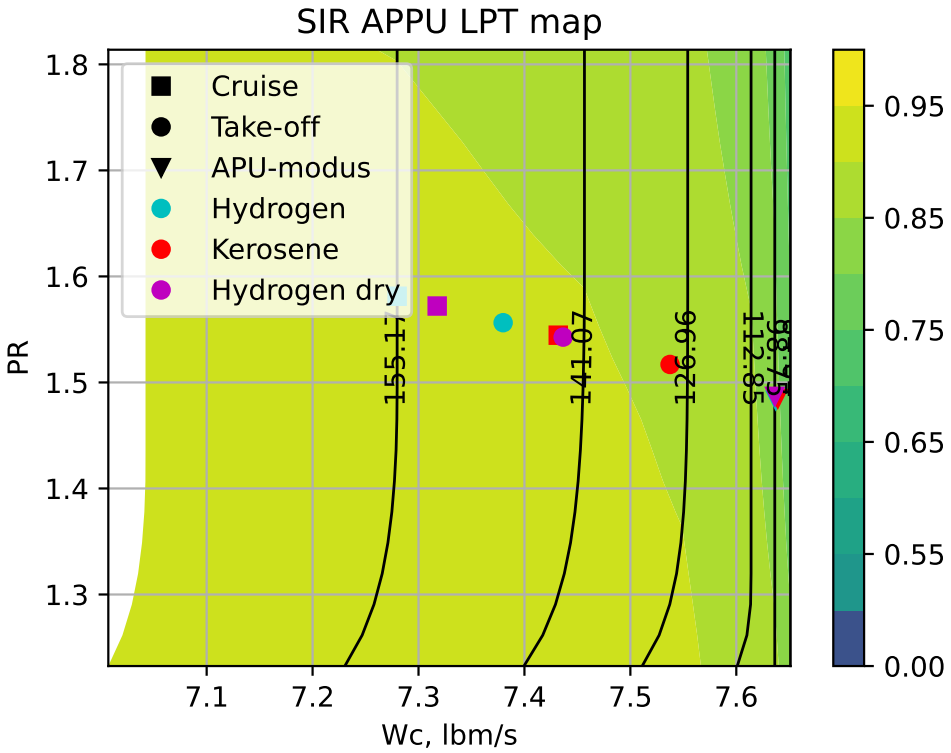

Figure A.8: SIR APPU LPT map

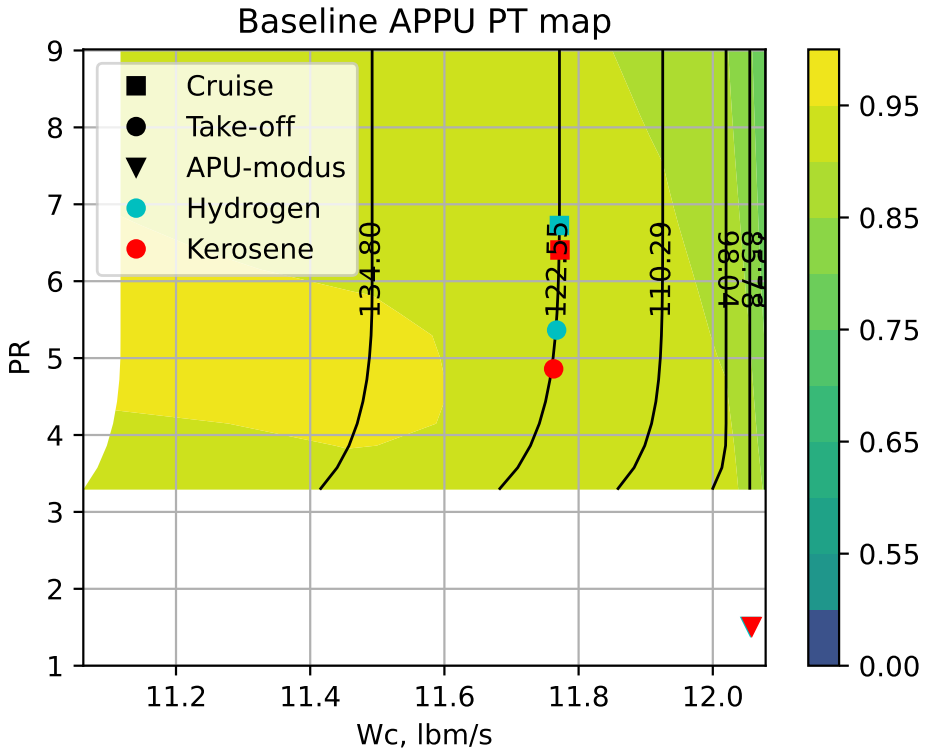

Figure A.9: Baseline APPU PT map

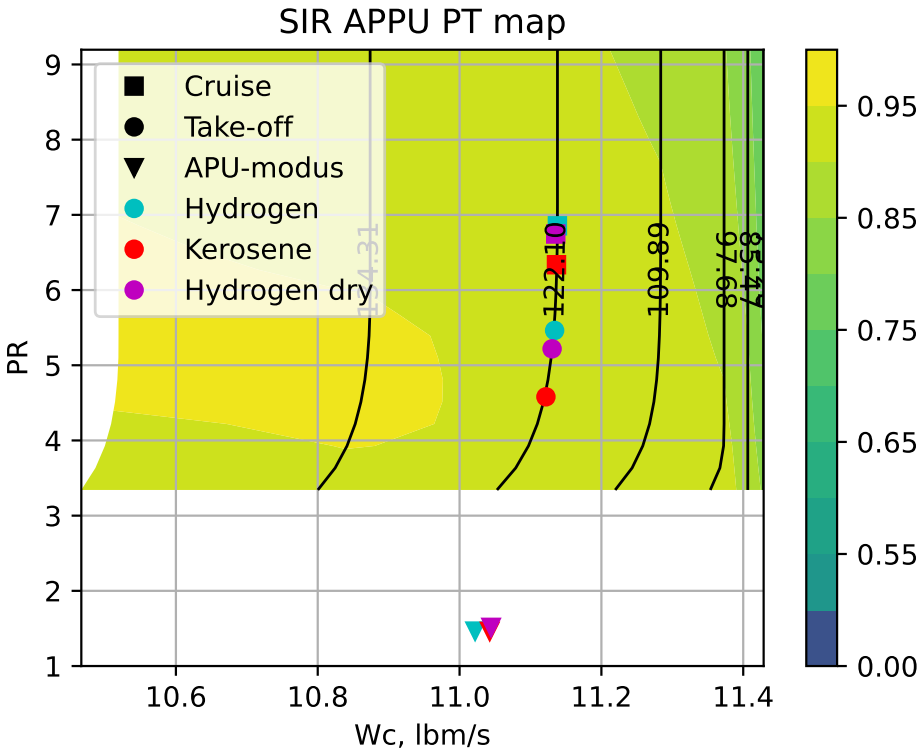

Figure A.10: SIR APPU PT map

B

Sensitivity analyses component efficiencies

This chapter displays the turbomachinery efficiencies and turbine cooling air fractions of both the baseline APPU and SIR APPU for the OPR-TET sensitivity analyses.

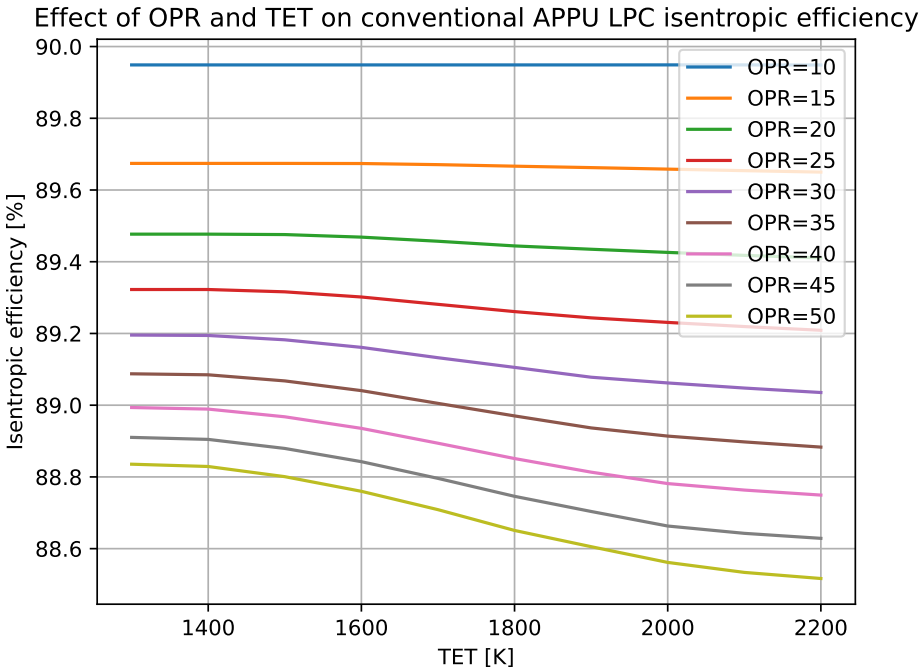

Figure B.1: Effect of OPR and TET on baseline APPU LPC isentropic efficiency

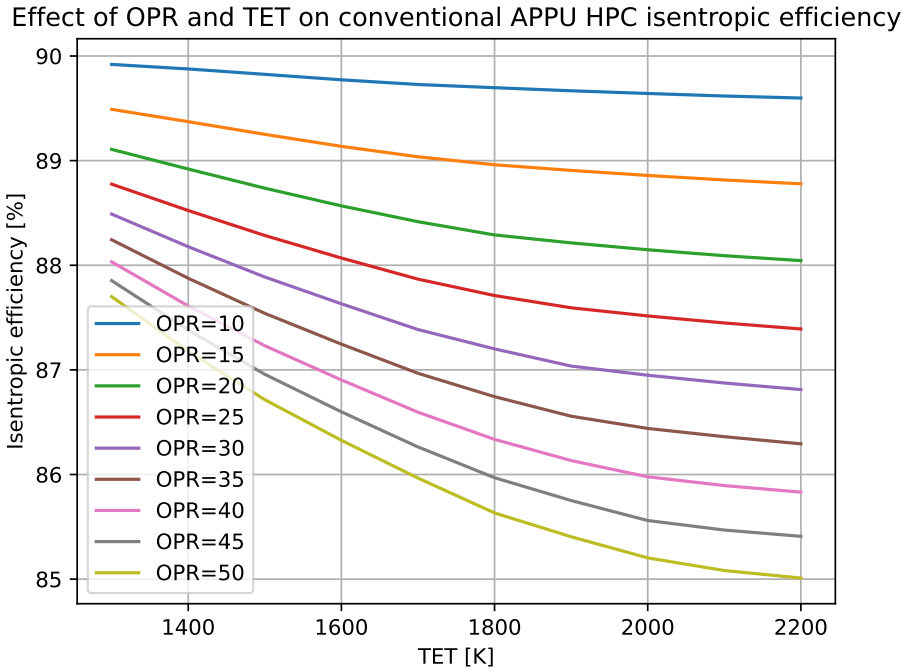

Figure B.2: Effect of OPR and TET on baseline APPU HPC isentropic efficiency

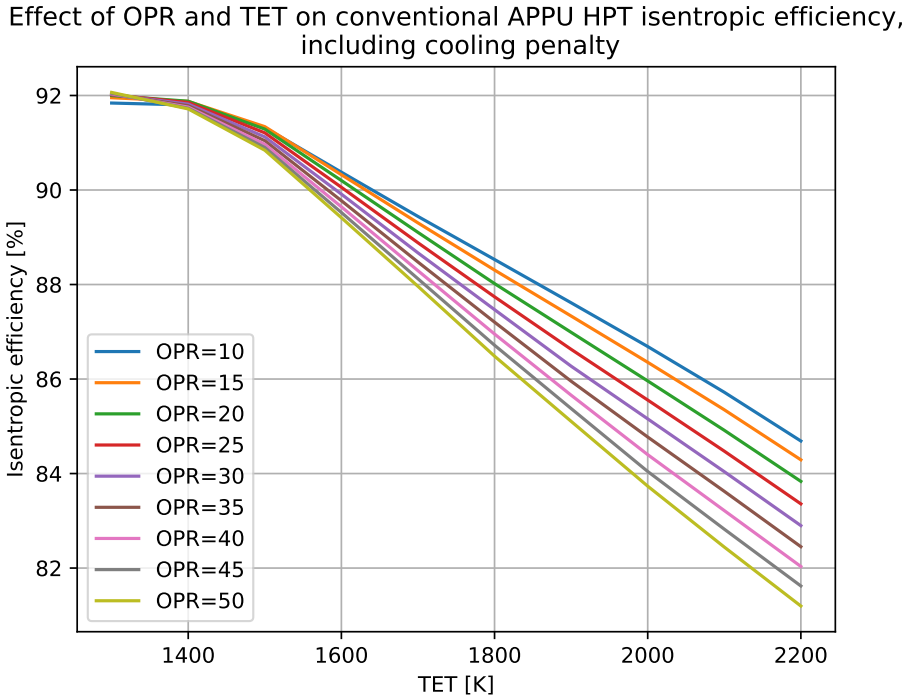

Figure B.3: Effect of OPR and TET on baseline APPU HPT isentropic efficiency, including cooling penalty

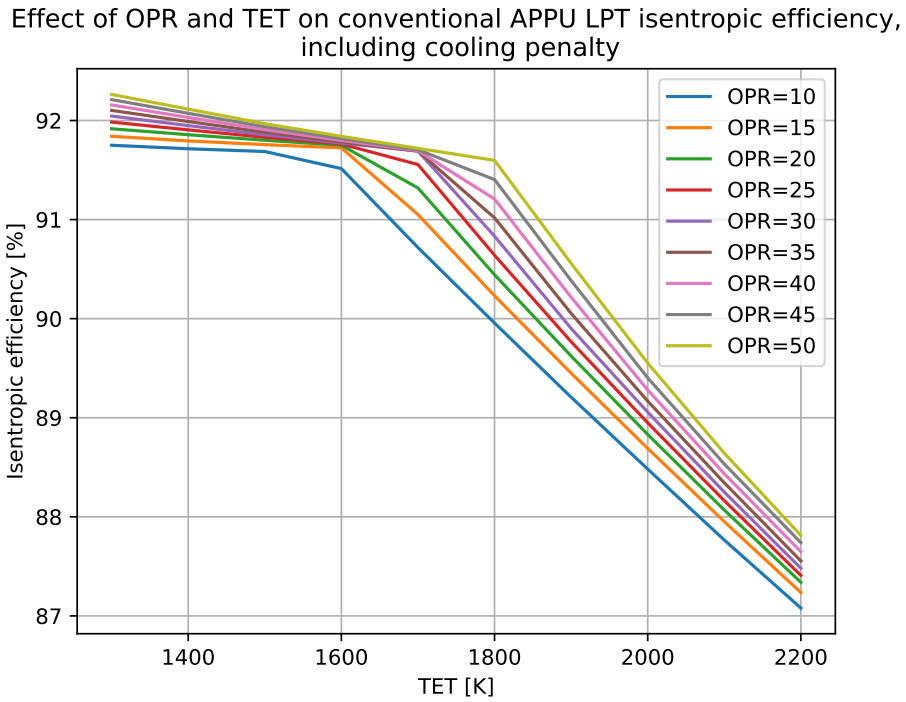

Figure B.4: Effect of OPR and TET on baseline APPU LPT isentropic efficiency, including cooling penalty

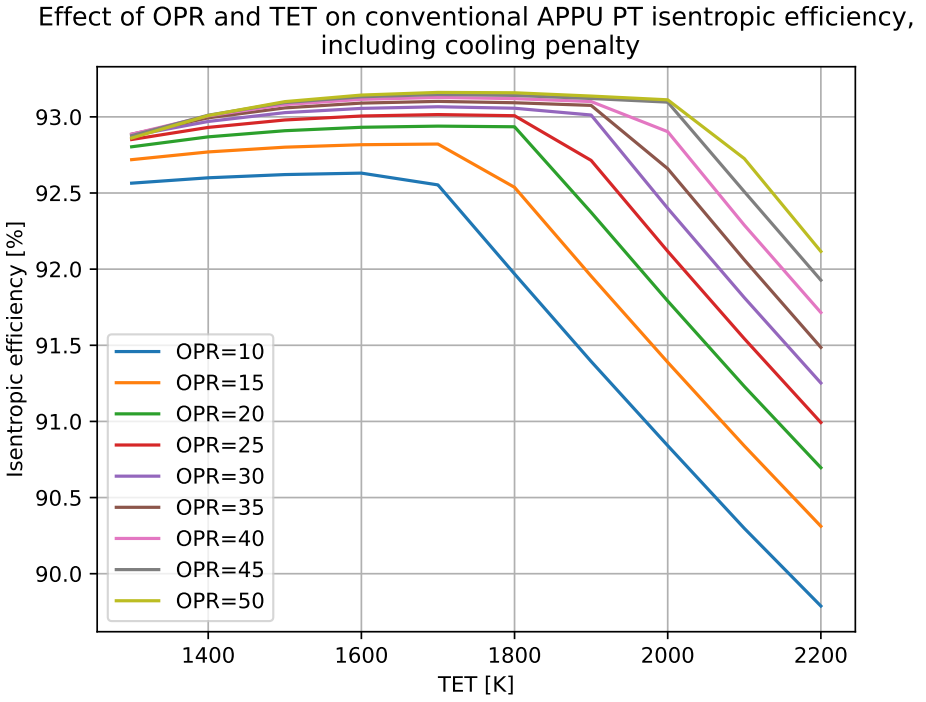

Figure B.5: Effect of OPR and TET on baseline APPU PT isentropic efficiency, including cooling penalty

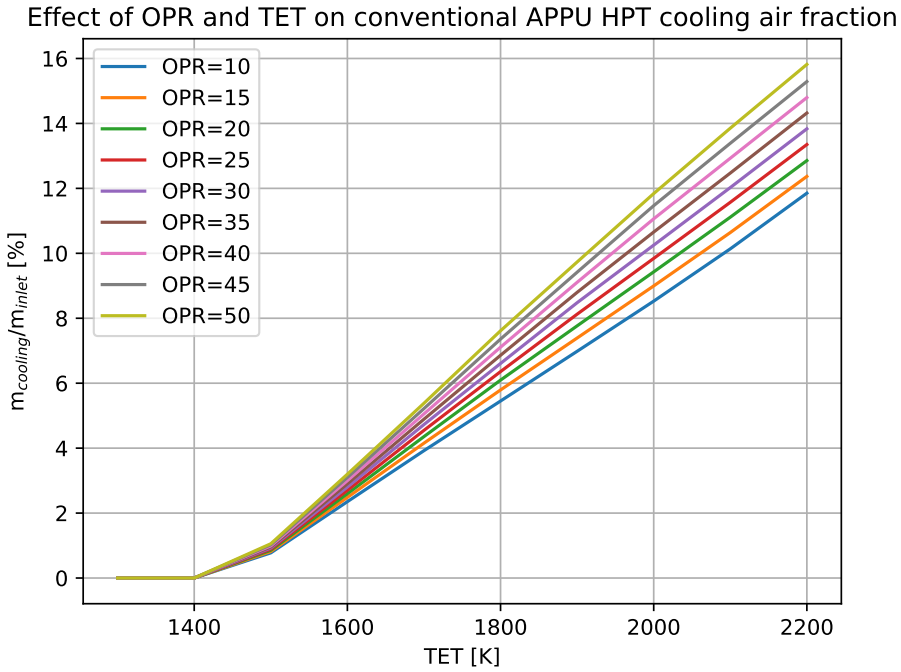

Figure B.6: Effect of OPR and TET on baseline APPU HPT cooling air fraction

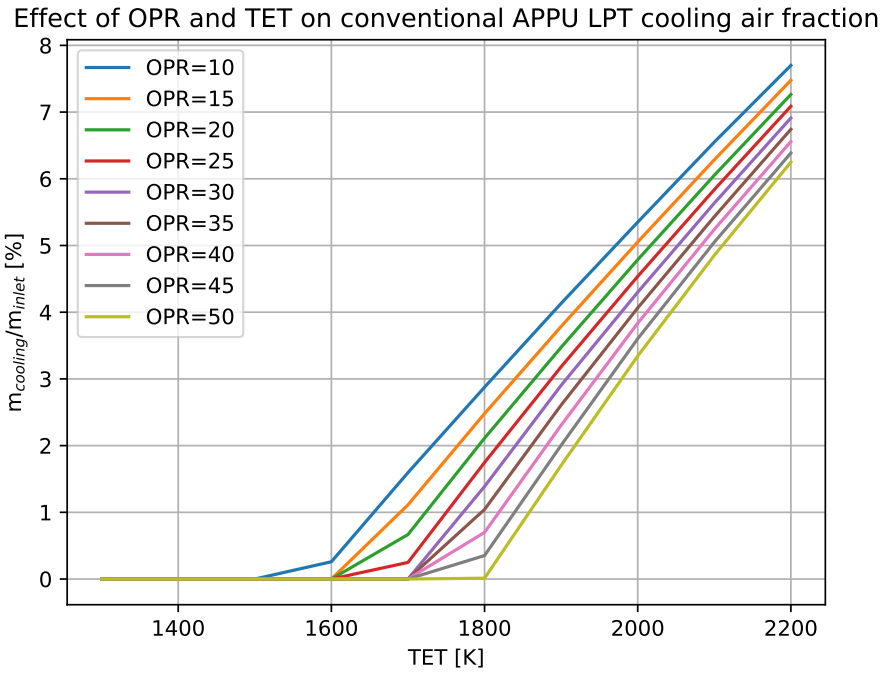

Figure B.7: Effect of OPR and TET on baseline APPU LPT cooling air fraction

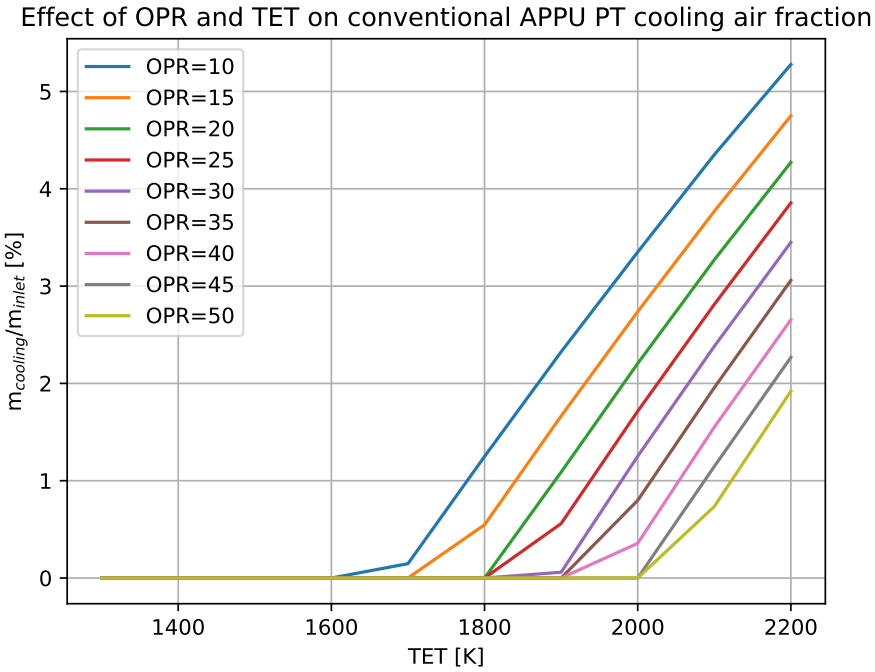

Figure B.8: Effect of OPR and TET on baseline APPU PT cooling air fraction

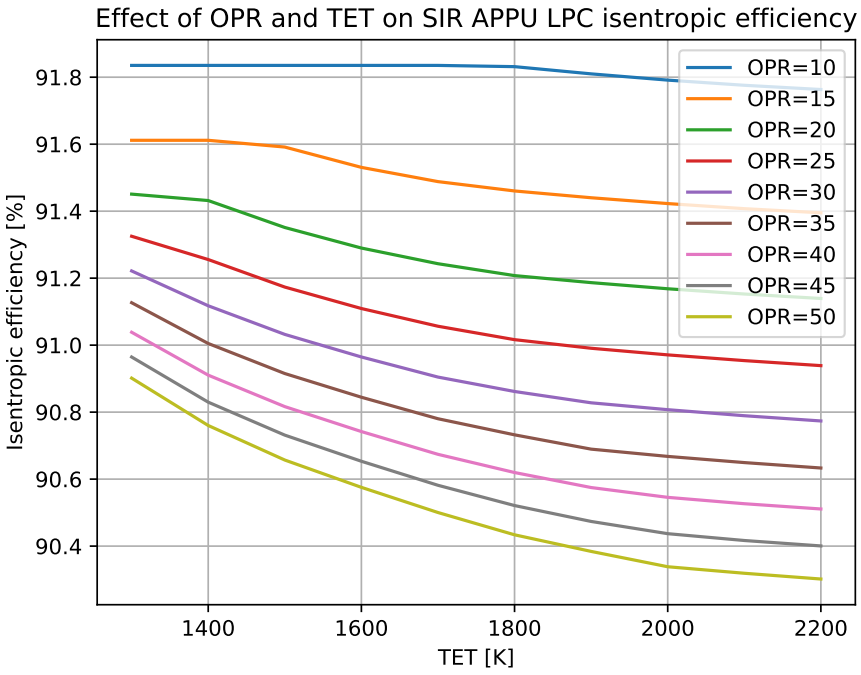

Figure B.9: Effect of OPR and TET on SIR APPU LPC isentropic efficiency

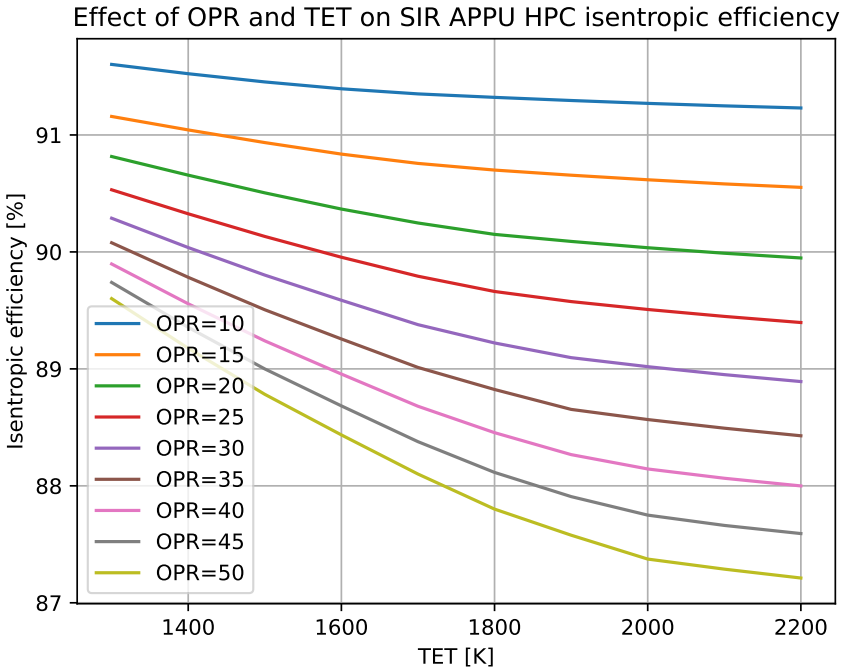

Figure B.10: Effect of OPR and TET on SIR APPU HPC isentropic efficiency

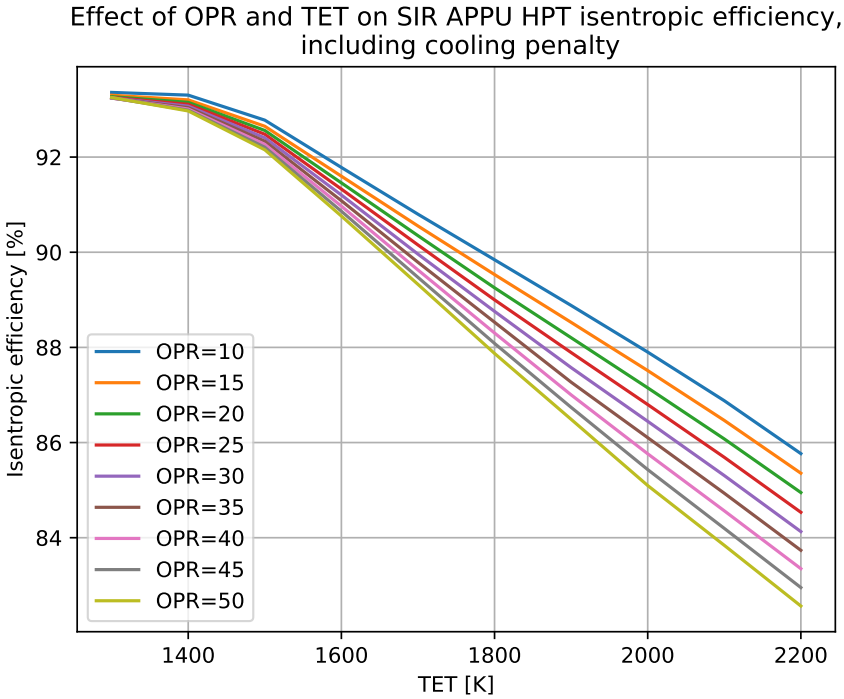

Figure B.11: Effect of OPR and TET on SIR APPU HPT isentropic efficiency, including cooling penalty

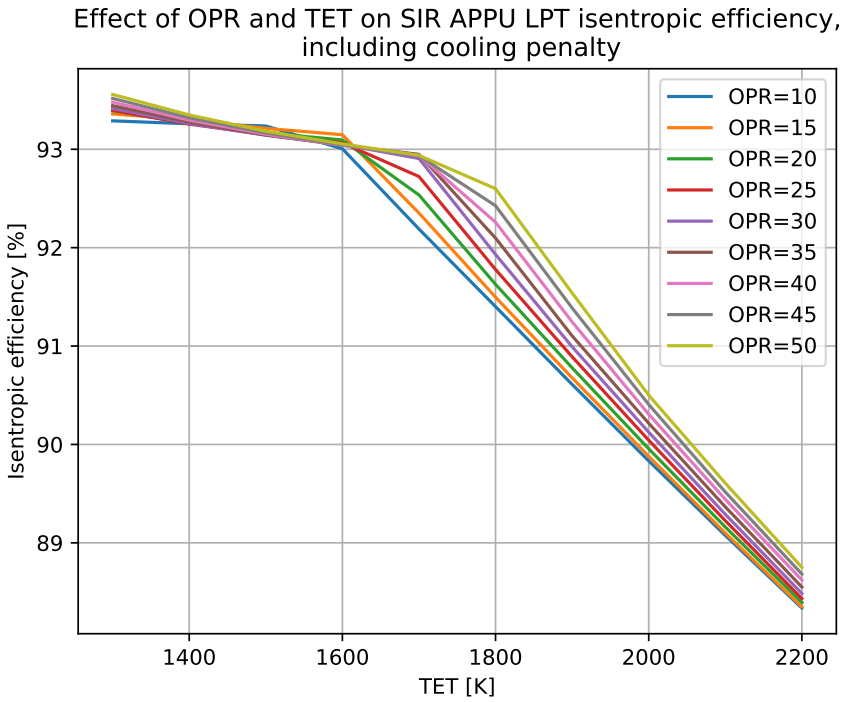

Figure B.12: Effect of OPR and TET on SIR APPU LPT isentropic efficiency, including cooling penalty

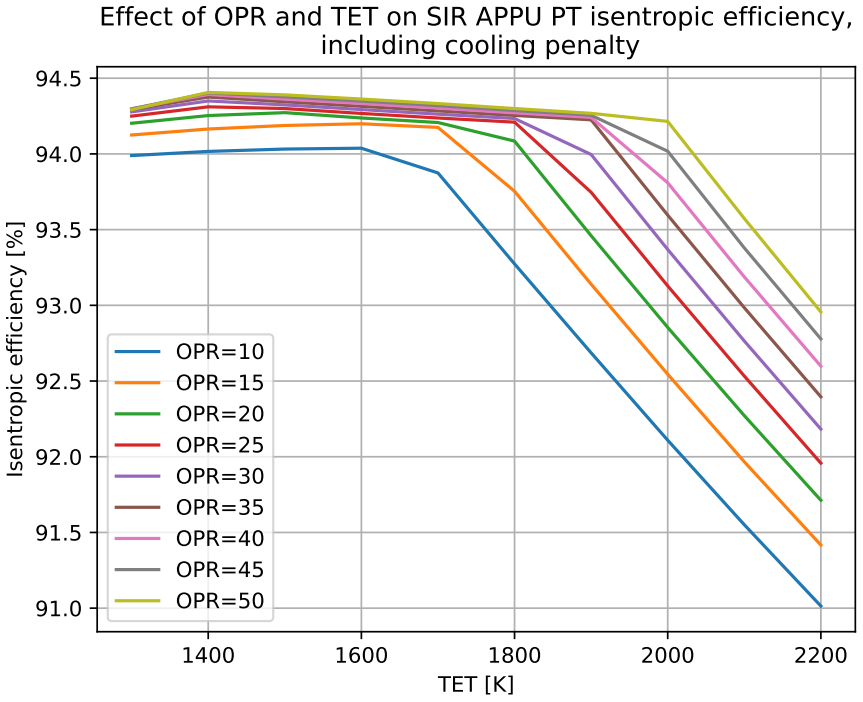

Figure B.13: Effect of OPR and TET on SIR APPU PT isentropic efficiency, including cooling penalty

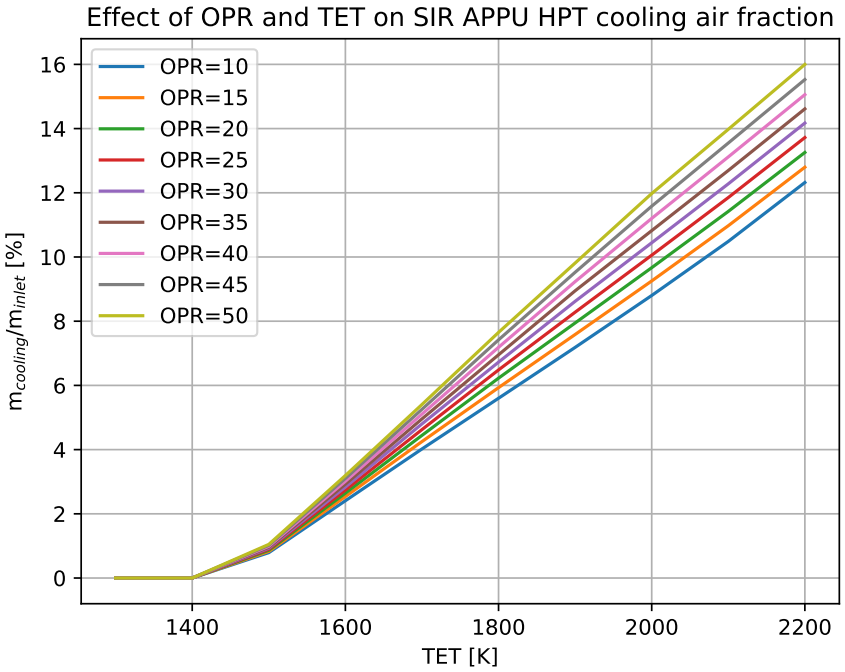

Figure B.14: Effect of OPR and TET on SIR APPU HPT cooling air fraction

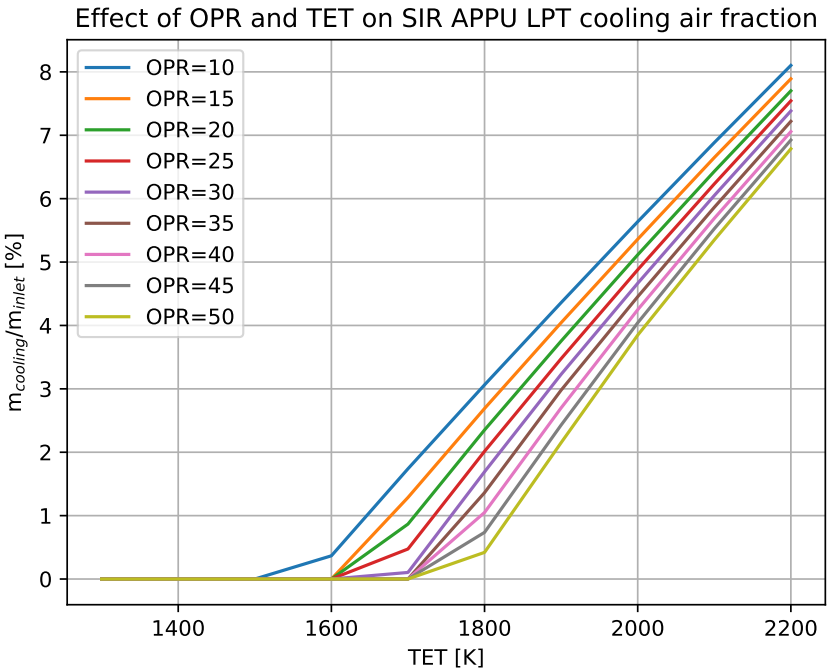

Figure B.15: Effect of OPR and TET on SIR APPU LPT cooling air fraction

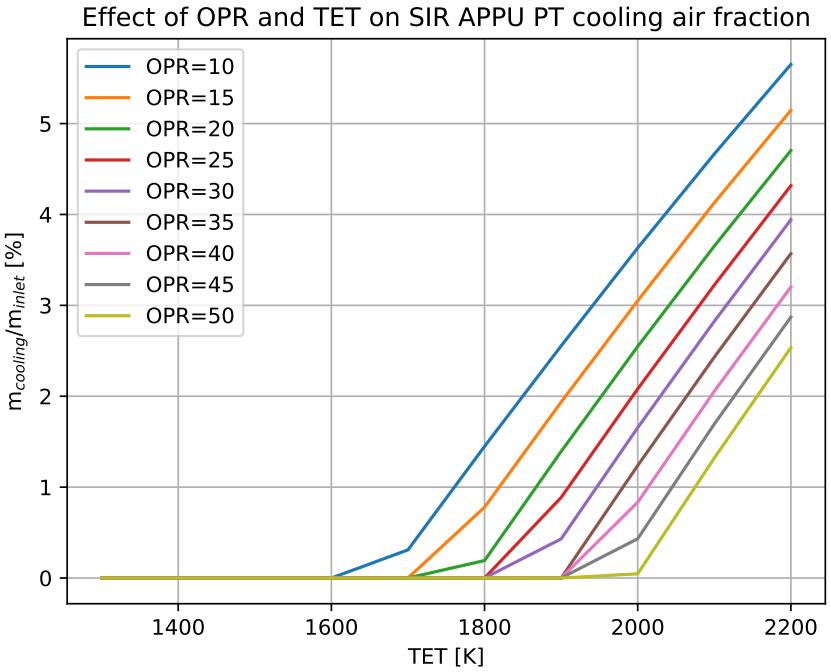

Figure B.16: Effect of OPR and TET on SIR APPU PT cooling air fraction